

Electronic Theses and Dissertations, 2004-2019

2015

Spectral Study of Asteroids and Laboratory Simulation of Asteroid Organics

Kelsey Hargrove
University of Central Florida

 Part of the [Astrophysics and Astronomy Commons](#), and the [Physics Commons](#)
Find similar works at: <https://stars.library.ucf.edu/etd>
University of Central Florida Libraries <http://library.ucf.edu>

This Doctoral Dissertation (Open Access) is brought to you for free and open access by STARS. It has been accepted for inclusion in Electronic Theses and Dissertations, 2004-2019 by an authorized administrator of STARS. For more information, please contact STARS@ucf.edu.

STARS Citation

Hargrove, Kelsey, "Spectral Study of Asteroids and Laboratory Simulation of Asteroid Organics" (2015).
Electronic Theses and Dissertations, 2004-2019. 1265.
<https://stars.library.ucf.edu/etd/1265>

SPECTRAL STUDY OF ASTEROIDS AND LABORATORY SIMULATED ASTEROID
ORGANICS

by

KELSEY D. HARGROVE
B.S. University of Central Florida, 2009

A dissertation submitted in partial fulfillment of the requirements
for the degree of Doctor of Philosophy
in the Department of Physics
in the College of Sciences
at the University of Central Florida
Orlando, Florida

Spring Term
2015

Major Professor: Joshua Colwell

© 2015 Kelsey D. Hargrove

ABSTRACT

We investigate the spectra of asteroids at near- and mid-infrared wavelengths. In 2010 and 2011 we reported the detection of 3 μm and 3.2-3.6 μm signatures on (24) Themis and (65) Cybele indicative of water-ice and complex organics [1] [2] [3]. We further probed other primitive asteroids in the Cybele dynamical group and Themis family, finding diversity in the shape of their 3 μm [4] [5] [6] and 10 μm spectral features [4]. These differences indicated mineralogical and compositional variations within these asteroid populations. Also in the mid-infrared region we studied a larger population of asteroids belonging to the Bus C, D, and S taxonomic classes to understand the relationship between any mineralogy and hydration inferred in the visible and near-infrared with the shape, strength, and slope of the 10 μm emission. We have discovered that at least 3 of the main Bus taxonomic groups (Cs, Ds, and Ss as defined by their visible spectra) clearly cluster into 3 statistically distinct groups based on their 8-13 μm spectra. Additionally we have attempted to simulate in a laboratory the possible organic compounds we have detected on two asteroids, using various mixtures containing aromatic and aliphatic hydrocarbons. We find that asteroid (24) Themis and (65) Cybele have τ_{CH_2}/τ_{CH_3} and N_{CH_2}/N_{CH_3} ratios similar to our 3-methylpentane, propane, and hexane residues, suggesting that the organics on these asteroids may be short-chained and/or highly branched. The τ_{CH_2}/τ_{CH_3} and N_{CH_2}/N_{CH_3} for asteroid (24) Themis are most consistent with the DISM, and some carbonaceous chondrites. The band centers of the C-

H stretch absorptions indicate that both asteroids may have aliphatic carriers chemically bonded to electronegative groups (i.e. aromatics), and some that are not. We also detect a $3.45 \mu\text{m}$ feature in the spectra of both asteroids that is present in several dense molecular clouds. Our results suggest an interstellar origin for the organics on (24) Themis, and likely (65) Cybele. The differences in the organics of Themis and Cybele are likely related to variations in thermal processing, irradiation and/or formation region in the solar nebula.

This work is dedicated to my family, my husband, and Autumn.

ACKNOWLEDGMENTS

The completion of this document and the research work described therein has been a long journey, one that at times was incredibly challenging. Life does not seem to care that we have important deadlines, or commitments to finish a task. In fact life can be exceptionally cruel when we are determined to finish a lifelong goal. In the past year, while gearing up for the writing of this work, I did not expect to lose most of my belongings when my apartment flooded, or to move mid-semester, or to get a call my mother needed medical care after an accident at work, or to find out my father almost needed open heart surgery after a routine operation. Life can be brutal, and puts forth an incredible effort to distract us. There are, though, amazing people in my life that counter-balanced the hard times. I am elated to have finished this epic undertaking, but I did not do it alone. I could not have succeeded without the invaluable support of several. To these select individuals, I owe you great thanks, much appreciation and my remaining sanity.

Christian Smith, my husband, and best friend. You were so integral in helping me achieve my dream. You were that shoulder to cry on when I wanted to give up and move to a cabin in rural Montana (or possibly South Carolina depending on my mood). When I was too serious your humor and sarcasm made me laugh. When I was frustrated you poured me a glass of my favorite red wine (if it was past 5pm of course). When others doubted me you remained my biggest fan. We wrote

the bulk of our dissertations at the same time, in the same room. The fact we didn't kill each other speaks worlds to how amazing you are. Thank you for picking up the slack when I was working day and night on this document. Without you I probably would have eaten frozen dinners for far too many days in a row, and we would have lost Autumn in a megalithic pile of laundry.

Mom and dad, without you I would not have gotten this far. I know it has been an incredible financial burden on our family, but I hope that I have made you proud. Thank you for understanding when I don't call you back right away. I was probably locked in my office writing, shut off from the world. Mom thank you for driving 8 hours at a moments notice to help us clean up after the apartment flood. Dad thank you for helping us move to a new home. You and mom helped us put our lives back together, and lessened the burden while I was trying to finish this work. Mom you have provided me with words of encouragement that no one else could. The stories you share about your experiences at work make me laugh, and realize that it happens to everyone. To my parents, I am forever grateful.

Whitney, you are my sister, but you are also my best friend. I appreciate you picking up the phone anytime of the day when I needed support. You give me such a different perspective on situations that I don't get from anyone else. You make me laugh. I love your stories. Your support and love has been invaluable. Thank you.

Bonnie Berry, my dear friend. You have been a source of confidence for me. Having shared similar experiences, venting with you has been an important part of my healing. Our thrifting adventures and wine/movie nights during these stressful times is my greatest therapy. Thank you

for stopping by at a moments notice, when times were hard. We did it. We really did it. Now our lives can finally begin.

I would like to give special thanks to Humberto Campins, my advisor as an undergraduate and graduate student. I sincerely appreciate the financial support and unique research opportunities that you provided for me. Your connections with Scott Sandford, Jaydeep Mukherjee, Javier Licandro, Marco Delbo, and others have given me the chance to work on incredible projects, many of which are described in this work.

Scott, Chris, Michel, Joe, and Ella, to each of you I owe my gratitude. Scott, thank you for letting me basically take over your laboratory for 3 summers in a row. I enjoyed learning from your many years of experience in astrochemistry. The knowledge I gained during those three years I cannot quantify. Chris and Michel, thank you for all of your help with my experiments, especially when things went awry. Joe and Michel, I have not forgotten you stayed until 8pm one night helping me fix the hydrogen flow to the UV lamp. You saved that experiment I otherwise would not have been able to repeat. Ella, I am so happy to have met you. You are such an amazing female role model. I look up to people like you.

To the members of my dissertation committee Josh Colwell, Yanga Fernandez, Mike Kelley and Dan Britt, I want to give my great appreciation for your academic support and input. I enjoyed learning from you, and I truly hope that this work reflects the top-notch Planetary Science Department we have at UCF. Thank you.

Much of the support for this work was provided by NASA's Graduate Student Research Program (GSRP) that allowed me to conduct the experimental portion of this study.

Our 2-4 μm work was conducted in part with the Infrared Telescope Facility that is operated by the University of Hawaii under Cooperative Agreement no. NCC 5-538 with the NASA, Science Mission Directorate, Planetary Astronomy Program.

This work is partially based on observations made with NASA's Spitzer Space Telescope that is operated by the Jet Propulsion Laboratory, California Institute of Technology under a contract with NASA.

TABLE OF CONTENTS

LIST OF FIGURES	xv
LIST OF TABLES	xxi
LIST OF ACRONYMS	xxiii
CHAPTER 1 : INTRODUCTION	1
1.1 The Dissertation	7
1.2 Remote Sensing Instruments and Laboratory Facilities	10
1.2.1 Infrared Telescope Facility	11
1.2.2 Spitzer Space Telescope	11
1.2.3 NASA Ames Laboratory of Earth and Space Sciences	14
1.3 Asteroid Targets and Laboratory Samples	15
1.3.1 Near-Infrared	15
1.3.2 Mid-Infrared	16
1.3.3 Laboratory Samples	16

CHAPTER 2 : ASTEROID TAXONOMY AND MINERALOGY	18
2.1 Taxonomy of Asteroids	18
2.2 Asteroid Types: The Formal Definition	21
2.3 Mineralogy and Composition of Asteroid Types.....	23
2.3.1 The Wavelengths of Investigation	23
2.3.2 Asteroid Superclasses	25
2.3.3 Meteorites	28
 CHAPTER 3 : EVIDENCE FOR HYDRATED MINERALS AND ORGANICS IN THE NEAR-INFRARED	 30
3.1 Introduction	31
3.2 Asteroid Observations	32
3.2.1 (24) Themis	33
3.2.2 (65) Cybele	33
3.2.3 (90) Antiope	34
3.2.4 (107) Camilla	35
3.2.5 (121) Hermione	35
3.2.6 (790) Pretoria	35
3.3 Data Reduction and Analysis.....	37

3.3.1	Spextool	38
3.3.2	ATRAN	41
3.3.3	Thermal Model	42
3.3.4	Band Characterization.....	49
3.4	Results	51
3.4.1	(24) Themis.....	53
3.4.2	(65) Cybele	54
3.4.3	(90) Antiope	54
3.4.4	(107) Camilla	58
3.4.5	(121) Hermione.....	58
3.4.6	(790) Pretoria	59
3.5	Discussion	59
CHAPTER 4 : MINERALOGY AND COMPOSITION OF ASTEROIDS IN THE MID- INFRARED		61
4.1	Introduction	62
4.2	Observations	65
4.3	Data Reduction	65
4.3.1	Post Processing	66

4.3.2	SPICE	68
4.3.3	Spitzer Align Modes Code	71
4.3.4	Thermal Modeling	77
4.4	Results	80
4.4.1	Themis Family and Cybele Group Asteroids	80
4.4.2	Asteroid C-, D-, and S-types	82
4.5	Discussion	84
4.5.1	Themis Family and Cybele Group Asteroids	84
4.5.2	Asteroid C-, D- and S-types	86
CHAPTER 5 : LABORATORY SIMULATION OF ASTEROID ORGANICS		89
5.1	Introduction	90
5.2	Laboratory Samples	93
5.3	Laboratory Techniques	94
5.3.1	Fabrication of Gas Bulbs	95
5.3.2	Experimental Techniques	98
5.4	Data Analysis	103
5.4.1	Identification of organic band centers and strengths	104
5.4.2	Calculation of Optical Depths and Column Densities	109

5.5	Results	110
5.5.1	Laboratory Samples	110
5.5.2	Band Centers of C-H stretch Aliphatic Features.....	113
5.5.3	Optical Depths and Column Densities	114
5.6	Discussion	118
CHAPTER 6 : CONCLUSIONS AND FUTURE WORK		129
6.1	Conclusions	130
6.1.1	Future Work	135
LIST OF REFERENCES		137

LIST OF FIGURES

- Figure 1.1 **Spitzer IRS Slit Apertures.** A schematic of the slit apertures used by the SL, SH and LH modules. For each module (and in the case of SL for each order), Spitzer takes spectra at 33% and 66% along the length of the slit. Adapted from Spitzer IRS Instrument Handbook (<http://irsa.ipac.caltech.edu/data/SPITZER/docs/irs/irsinstrumenthandbook/1/>) . 12
- Figure 2.1 **SMASS visible spectra of selected asteroid classes.** Characteristic visible spectra of asteroids belonging to the Bus C, D, and S taxonomic types. The C-class includes C-, B-, Cb, Cg-, Ch-, and Cgh- types. Adapted from [7] 22
- Figure 3.1 **Frame A of and an AB pair.** Frame A consists of signal from dark current, the telescope, the sky, and the target. 37
- Figure 3.2 **Frame B of and an AB pair.** Frame B consists of signal from dark current, the telescope, and the sky. The target was not observed in this frame. 38
- Figure 3.3 **Reflectance model for (121) Hermione.** A model of reflected light from the surface of asteroid (121) Hermione. The region between approximately 2.5 and 2.9 μm is the region of strong telluric absorptions in Earth's atmosphere. Due to interpolation in this region

there is a small artifact in the 2.9-3.1 μm region that produces a plateau rather than a smoothly decreasing reflectance. This artifact is of such small scale that it does not affect our data. . . . 43

Figure 3.4 **Thermal model for (121) Hermione.** A plot of the estimated thermal radiation emitted from the surface of asteroid (121) Hermione. 46

Figure 3.5 **Asteroid (121) Hermione and thermal contribution.** A plot of asteroid (121) Hermione reflectance spectra contaminated with thermal emission (black circles). The red line shows a model of this thermal contribution that we subtracted from our spectra. This figure illustrates how the thermal contribution is typically not significant shortward of about 3.5 μm . 48

Figure 3.6 **Example of “Sharp” and “Rounded” 3 μm Features.** An example of the “sharp” and “rounded” variations of the 3- μm feature. Panel (a) provides an example of the sharp 3- μm absorption produced by the fundamental stretch vibration of hydroxyl, and is diagnostic of H₂O incorporated into a mineral lattice or at interlayer sites. Panel (b) is a rounded variation of the 3- μm absorption caused by the symmetric stretch of the H₂O molecule in water ice. 50

Figure 3.7 **2-4 μm reflectance spectra of primitive asteroids in the Themis family and Cybele group.** Shown are: (24) Themis, (65) Cybele, (90) Antiope, (107) Camilla and (121) Hermione, and (790) Pretoria. This small sample of primitive asteroids show diversity in the shape and depth of their 3 μm features. The grey boxes are regions of atmospheric absorptions. 52

Figure 3.8 **2-4 μm reflectance spectra of (24) Themis and (90) Antiope.** The 2-4 μm reflectance spectra of asteroids (24) Themis [1], and (90) Antiope, obtained with the IRTF, and

rebinned to a resolution $R=167$. The K-band continuum was extrapolated from the visible and NIR spectrum near $1.95\text{-}2.5\mu\text{m}$. The $0.8\text{-}2.5\text{-}\mu\text{m}$ spectra are from the MIT-UH-IRTF survey (<http://smass.mit.edu/minus.html>). The grey box is a region of atmospheric absorption. . . . 55

Figure 3.9 **Ice model comparison to Themis and Antiope.** Our two independent (90) Antiope spectra compared with asteroid (24) Themis [1], and an ice model [2]. We rebinned our spectra to a resolution $R=167$. All asteroid spectra have been divided by a continuum we extrapolated from the slope of their spectrum in the K-band region ($1.95\text{-}2.5\mu\text{m}$). We have normalized the ice model to the $3.1\mu\text{m}$ region of each spectra. 57

Figure 4.1 **(107) Camilla profile.** This example is for the SL 1 module, nod position 1. Spice determines the profile by averaging orders at a given spatial position. 68

Figure 4.2 **(107) Camilla ridge.** This is an example of the maximum in the peak profile, or the ridge, that Spice determined was located at 66% along the length of the slit. 69

Figure 4.3 **Extracted Spectrum of (107) Camilla.** The extracted spectra is from the SL1 nod position 1, covering the $\sim 7\text{-}14\mu\text{m}$ range. 70

Figure 4.4 **(107) Camilla point source tune.** The point source procedure tuned the SL1 nod position 1 spectrum of (107) Camilla to the $\sim 7\text{-}14\mu\text{m}$ range. The spectrum has been corrected by a scaling constant to convert the final flux into unit of Jansky. Note the difference in the y-axis values compared to Figure 4.3. 71

Figure 4.5 **(107) Camilla SL2 spectrum scaled to SL1.** Our routine, COMBMODES, determined the scale amount that best aligned the SL2 mode to the SL1 mode. 72

Figure 4.6	(107) Camilla SH spectrum scaled to SL1. Our routine, COMBMODES, determined the scale amount that best aligned the SH mode to the SL mode.	74
Figure 4.7	(107) Camilla LH spectrum scaled to SH. Our routine, COMBMODES, determined the scale amount that best aligned the LH mode to the SH mode.	75
Figure 4.8	Aligned 5-35-μm spectrum of (107) Camilla. This aligned spectrum is the result of scaling the SL2, SH, and LH modes.	77
Figure 4.9	(24) Themis and (90) Antiope NEATM fits. The Near-Earth Asteroid Thermal Model (red line) fit to the 5-14 μm spectral energy density of asteroid (24) Themis and (90) Antiope.	78
Figure 4.10	8-10 μm emission spectra of hydrated asteroids from the Cybele group, and Themis family. The Cybele group objects are shown in the left panel, and the Themis family objects are shown on the right. We obtained these emission spectra by dividing the Spectral Energy Density of each asteroid by their respective thermal models. Spectra are offset for clarity.	81
Figure 4.11	8-13 μm spectra of C-, D-, and S-types. The emission spectra of C-, D-, and S-type asteroids cluster into 3 statistically distinct groups based on their 8-13 μm spectra. The solid lines are the average of the 8-13 μm spectra. The dashed lines represent the highest and lowest emissivity spectra for each asteroid type at 10 μm . All spectra are normalized at 8.0 μm	83

Figure 5.1	Aliphatic and aromatic hydrocarbons. We used these four types of alkanes in our simulations of asteroid organics. We chose these particular alkanes to vary the amount of initial -CH ₂ - groups.	94
Figure 5.2	Example cryovac system. This cryovac system is similar to the one we used for our experiments. The closed-cycle helium cooler allowed us to reach temperatures close to 15K.	99
Figure 5.3	Schematic of system sample head. Our gas mixtures were deposited onto the system via the gas inlet valve, where it condensed into ice on the window. We situated the window at an angle such that we could perform UV photolysis and deposition simultaneously. Adapted from [8].	100
Figure 5.4	Example of an astrophysical, organic-rich ice created in the laboratory. These ices formed on a zinc-solenoid window after deposition of the bulb material at temperatures near 15K, and under UHV pressures.	101
Figure 5.5	Possible baselines for analysis of C-H stretch region. Shown is the spectrum of asteroid (24) Themis with two possible baselines to isolate the C-H stretch organic features. We chose to use the blue dashed baseline for our asteroids, as well as our laboratory spectra.	104
Figure 5.6	Laboratory spectra organic gaussian deconvolution. We used Gaussian deconvolution to determine the optical depth (τ), FWHM, and band centers of the organic features. We show the complex organic residue produced by the starting mixture that contained the alkane hexane. We fit several Gaussians (orange) to the features produced by aromatics, aliphatics and possibly tertiary carbon ($\sim 3.45 \mu\text{m}$). In the 3.3-3.35 μm region and the 3.5-	

3.55 μm region the data (black) are not well fit to the sum of the Gaussians (red). This may be due to band broadening or wings on the CH_3 asymmetric feature and the CH_2 symmetric stretch feature. 106

Figure 5.7 **Asteroid (24) Themis organic gaussian deconvolution.** We applied a Gaussian deconvolution method to the aliphatic features in two sets of our higher S/N spectra of (24) Themis. We focused only on the four aliphatic C-H stretch features, although there may be other features such as tertiary carbon around 3.45 μm . Our two sets of spectra may indicate the organics are different as this asteroid rotates. These data have been smoothed using adjacent averaging techniques. 107

Figure 5.8 **Asteroid (65) Cybele organic gaussian deconvolution.** We applied a Gaussian deconvolution method to the aliphatic features in two sets of our higher S/N spectra of (65) Cybele. We have focused on only the four aliphatic C-H stretch features, although there may be other features such as tertiary carbon around 3.45 μm , similar to Themis. These data have been smoothed using adjacent averaging techniques. 108

Figure 5.9 **Laboratory residues at 235 K and 300 K.** Shown are the laboratory samples at (a) 235 K and (b) 330 K. At 235 K we find several features due to H_2O ice, aromatic and aliphatic hydrocarbons, C=O, C=C. At 300 K, once all volatiles have sublimated, we find absorptions due to OH, C=O, C=C, and complex organic material. 111

Figure 5.10 **Laboratory residues in the 3.2-3.6 μm region at 300 K.** Dashed lines locate the positions of the four aliphatic C-H stretch features. 112

LIST OF TABLES

Table 1.1 Asteroids Observed with The Infrared Telescope Facility in the 2-4 μm Region .	15
Table 1.2 Laboratory Samples Prepared at the NASA Ames Astrochemistry Laboratory . .	17
Table 3.1 Asteroids Observed with The Infrared Telescope Facility (IRTF)	36
Table 3.2 Band Depth Results and Presence of Organic Materials	53
Table 4.1 Observational Details of Asteroids Observed with The Spitzer Space Telescope	64
Table 4.2 Position of Aliphatic CH Stretch Features	80
Table 4.3 Relationship Between Asteroid Taxonomic Type with Spectral Features in the Near-, and Mid-infrared.	88
Table 5.1 Ratio of Water, Aromatics and Alkanes in our Laboratory Samples	95
Table 5.2 Position of Aliphatic CH Stretch Features	114
Table 5.3 Optical Depth and Column Densities of the Methyl (-CH ₃) and Methylene (-CH ₂ -) Components of our Laboratory Samples.	115
Table 5.4 Optical Depth and Column Densities of the Methyl (-CH ₃) and Methylene (-CH ₂ -) Components of Select Asteroid Spectral Sets.	116

Table 5.5	N_{CH_2}/N_{CH_3} Ratios for Our Laboratory Organics	117
Table 5.6	τ_{CH_2}/τ_{CH_3} and N_{CH_2}/N_{CH_3} Ratios for Our Asteroid Organics	118
Table 5.7	Optical Depth and Functional Group Ratios of Asteroids and Astronomical Sources	119
Table 5.8	Optical Depth and Functional Group Ratios of Asteroids and Meteorites	124
Table 5.9	Position of Aliphatic C-H stretch Features	127

LIST OF ACRONYMS

3-MP	3-methylpentane
ATRAN	Atmospheric Transmission of Near- and Far-Infrared Radiation
AU	Astronomical Unit
BCD	Basic Calibrated Data
BMASK	Basic Calibrated Data Mask
C	Carbon
CCD	Charge-Coupled Device
CH	Methylidyne
CH ₂	Methylene
CH ₃	Methyl Radical
CH ₄	Methane
C ₃ H ₈	Propane
C ₁₀ H ₈	Naphthalene
CN	Cyano Radical
CO	Carbon Monoxide
CSHELL	Cryogenic Echelle Spectrograph
DISM	Diffuse Interstellar Medium

DNA	Deoxyribonucleic Acid
ECAS	Eight Color Asteroid Survey
FITS	Flexible Image Transport System
H ₂	Hydrogen
HCN	Hydrogen Cyanide
H ₂ O	Water
Hg	Mercury
IDL	Interactive Data Language
IDP	Interplanetary Dust Particles
IPAC	Infrared Processing and Analysis Center
IR	Infrared
IRAC	Infrared Array Camera
IRS	The Infrared Spectrograph
IRSA	Infrared Science Archive
IRTF	Infrared Telescope Facility
ISM	Interstellar Medium
LH	Long-High
LL	Long-Low
LXD	Long Cross-dispersed
MBC	Main Belt Comet
MC	Mars Crossers

MIPS	Multiband Imaging Photometer for Spitzer
NASA	National Aeronautics and Space Administration
NEA	Near Earth Asteroid
NEATM	Near Earth Asteroid Thermal Model
NH	Imidogen
NSFCAM	National Science Foundation Camera
OH	Hydroxyl Group
PAH	Polycyclic Aromatic Hydrocarbon
PC	Principle Component
RA	Right Ascension
RNA	Ribonucleic Acid
S/N	Signal-to-Noise
SH	Short-High
SHA	Spitzer Heritage Archive
Si	Silicon
SL	Short-Low
SMASS	Small Main-belt Asteroid Spectroscopic Survey
SpeX	Spectral Extraction
SPICE	Spacecraft Planet Instrument C-matrix Events
TNO	Trans-Neptunian Object
WISE	Wide-field Infrared Survey Explorer

UT	Universal Time
UV	Ultra-Violet
VNIR	Visible and Near-Infrared
Xe	Xenon

CHAPTER 1

INTRODUCTION

Asteroids are ancient relics leftover from the epoch of planetary formation, and they are the most direct remnants of the original materials that were incorporated into the planets. These objects are ancient record keepers with a library of information that details the earliest conditions and composition of our solar system, which has long since been erased on other bodies such as Earth. Asteroids are within reach of our telescopes and our space probes, making them prime targets for our investigations of the past. By studying the physical nature, distribution, formation mechanisms, and evolution of asteroids planetary scientists can begin to understand how planets formed in our solar system, and in other solar systems, and ultimately why an abundance of life and water exists here on Earth.

The main population of asteroids is located between the orbits of Mars and Jupiter, in a region called the Main Asteroid Belt. These objects are plentiful, and relatively easy to study. Other important populations are known as near-Earth asteroids (NEAs) and Mars crossers (MCs). These asteroids are small and would be difficult to observe, though they come relatively close to Earth, allowing us to study them sometimes in greater detail. In the outer reaches of the Solar System there are cold, icy bodies called trans-Neptunian objects (TNOs), located beyond the orbit of Nep-

tune in a region known as the Kuiper Belt. These asteroids are distant, dark and difficult to study, but likely have preserved the most clues to our Solar System's early history.

Planetary Scientists study asteroids with both ground-based and space-based instruments sensitive to various regions of the electromagnetic spectrum. In the visible ($\sim 0.4\text{-}0.8\ \mu\text{m}$) we observe the sun's light reflected off the surface of these bodies, which can reveal absorption features due to a plethora of minerals, and the presence of iron on the surfaces of asteroids. Asteroids have thus far been observed most often in the visible as our earliest technologies made this wavelength region most accessible. With improvements in our technology we have expanded our studies to the visible-near-infrared ($\sim 0.8\text{-}4\ \mu\text{m}$). At these wavelengths we can also detect minerals and the presence of iron, though now we can observe the overtone and fundamental features of ices, carbonates, hydroxyl and organics. Observations in the mid-infrared ($5\text{-}40\ \mu\text{m}$), we can detect the solar radiation thermally re-emitted from an asteroid's surface. At these diagnostic wavelengths we are able to detect the fundamental features of the bond between silicon and oxygen, implying silicates, and emissions due to minerals, H_2O , and organics. Additionally we can infer the temperature, surface texture, and surface porosity of an object. Combined the visible, near- and mid-infrared wavelength regimes help us to understand the big picture view of an asteroid's mineralogy and composition, which is directly related to the thermal processing it, or the parent body from which it came, experienced.

Since their formation, asteroids have experienced collisional, dynamical, and sometimes thermal evolution that has shaped their physical and orbital properties. Researchers that study the physical properties of asteroid surfaces can benefit from understanding how these bodies have

evolved over time. Though this can be quite challenging as there are processes that can alter our interpretation of asteroid surface spectra. For example, asteroids experience small scale collisions from micrometeorites, and are subject to solar radiation and cosmic rays. Together these forms of alteration are known as space weathering, and can slowly changes the surface characteristics of asteroids depending on their composition. These compositional changes are then reflected in our spectra of these bodies. For instance, space weathering can darken the surface of silicate-rich objects, producing a reddened spectral slope in the visible and near-infrared [9]. The opposite may be true for primitive carbonaceous objects. Space weathering may produce bluer spectral slopes depending on the relative abundances of carbonaceous, and organic material compared to silicates on the object's surface [9]. Space weathering can also dampen and/or shift the band center of key spectral features. These alterations make it difficult for us to link asteroid parent bodies with the meteorites we have studied in much more detail.

Another process that can shape the surface composition of asteroids is thermal processing, which can alter the existing mineralogy of asteroids, and in extreme cases completely restructure the interior all the way to the surface. Most of the thermal evolution that asteroids experienced happened relatively soon after their formation, billions of years ago, although not all asteroids experienced it to the same degree. These ancient variations in thermal processing produced two main populations of asteroids: processed asteroids, those that experienced significant thermal evolution, and primitive asteroids, those that did not experience much. Studying these distinct populations is important. For example, processed asteroids are crucial for our understanding of the formation and evolution of the terrestrial planets. These bodies are remnant planetesimals that grew large enough

to thermally differentiate, and after millions of years of collisions have left behind pieces of their metal-rich cores, and less frequently their olivine-rich mantles and pyroxene-rich crusts, giving us insight into the thermal processes they, and ultimately Earth, experienced in the early epochs of planetary formation. Processed asteroids dominate the inner main asteroid belt. Their surfaces are typically bright, making them relatively easy to study, with pronounced spectral characteristics indicating metals and several high temperature minerals.

Primitive asteroids are those that have experienced minimal thermal and aqueous processing. These objects are the main focus of this work, and are of interest to researchers because they may preserve detailed records of the primordial composition of the solar nebula in which they formed some 4.6 billion years ago. These bodies reside in the middle and outer main belt, and extend to the outer reaches of the Solar System, beyond the orbit of Neptune, in the Kuiper Belt. Primitive objects are also remnant planetesimals, though given that they likely formed at greater heliocentric distances the available materials in the sun's accretion disk were different than that for processed asteroids. The parent bodies of primitive asteroid types must have formed beyond the snow line, the distance from the sun past which ice could condense in the solar nebula. Primitive asteroids incorporated dark carbonaceous material and frozen volatiles during their formation. In many cases this accumulated water ice was eventually melted as a result of a primordial heating source such as long-lived radionuclides, ^{26}Al , or electric induction of solar wind during our sun's T-Tauri phase [10]. Although, some primitive objects never experienced heating sufficient to melt these acquired ices. For example, we have detected in various amounts frozen water, ammonia, and methane on several Kuiper-Belt Objects, the distant moons of giant planets, and Pluto and its moon Charon.

There is no question that ice is abundant in the outer solar system. Temperatures there do not exceed the sublimation temperature of many ices. Therefore it was unexpected by the community for ice to be present on primitive asteroids in the Main Belt since ice should be thermodynamically unstable, especially on the surface, on very short timescales at these heliocentric distances [11]. For instance "dirty ice" or ice with the same albedo of a dark primitive asteroid, typically $<10\%$, would sublimate at approximately 1 myr^{-1} at around 3 AU [1]. Additionally on active comets, such as 9P/Tempel, the ice resides mainly below the surface [12]. Subsurface reservoirs of ice are also theorized to exist in Trojan asteroids and asteroids belonging to the D classification, but have eluded our detection due to the shallow penetration depth of reflection spectroscopy. So why is ice present on the surfaces of several asteroids given the supposedly unfavorable conditions? This is an open and ongoing question for researchers that study primitive MBAs. Several mechanisms have been proposed such as sublimation frost, impact gardening, the photolysis of hydrated minerals, or deposits from a recent comet impact. Taking asteroid (24) Themis for example a water-ice frost could form due to sublimation activity within subsurface layers that deposits a thin layer of ice on its surface. This scenario is plausible considering that several members of the Themis family exhibit cometary activity [13], although no evidence of this kind has been observed on Themis [11]. Impact gardening could expose or bring near to the surface buried ice sufficient for us to detect with reflection spectroscopy. This process occurs on the moon at a rate of approximately 1 mGyr^{-1} [1]. Therefore the impact gardening rate of Themis would have to be large enough to account for the wide spread distribution of surface ice on this roughly 200 km diameter object. It is also plausible, but not likely, that a nearby comet impact deposited material on the surface of

Themis. If this occurred we would expect to detect a dust band around Themis. This dust signature has not been observed on Themis or the several other asteroids with evidence of an icy surface.

Another lingering question is the connection between water-ice and organics. Does the stability of water-ice possibly require the presence of organics? Several models for the longevity of water ice includes a combination of dust and ice grains [14] [15]. It is also possible that the water-ice-dust mixture is in a fluffy matrix that is not in thermal equilibrium with the warm asteroid's surface. Could the addition of organics also aid in the longevity of ice? Thus far, only two asteroids have been observed to have the signatures of both water-ice and organics: (24) Themis and (65) Cybele [1] [3], while several other asteroids have only evidence of water ice [4] [5] [16] [17]. Though the organic features are inherently weaker in strength than that of the water feature, and require higher signal-to-noise (S/N) spectra for detection. Additionally, the asteroids likely to harbor organics are distant and extremely dark, with low albedo surfaces that can absorb upwards of 90% of the sun's radiation. This makes achieving high S/N spectra of these primitive asteroids challenging for observers.

The detection of organic hydrocarbons on asteroids may be difficult, but these from other astronomical sources have been studied by researchers in more detail. For example other sources of organics include our extensive meteorite collection here on Earth, comets, Interplanetary Dust Particles (IDPs), the moons of giant planets, and the interstellar medium. The organics we have observed on asteroids thus far have not been investigated in detail. This work has compared and measured the organics on two asteroids with organics throughout the solar system, and in our meteorite collection. Our goal is to answer several questions: Are the organics on Themis and Cybele

of interstellar origin? Are they more similar to IDPs and comets? Which meteorite, if any, likely originated from these asteroids?

In this work, we have also investigated other Themis family member (90) Antiope, and other Cybele group members (107) Camilla, (121) Hermione, and (790) Pretoria for the presence of water-ice (or other hydration features), and organics. We aim to understand if other Themis family and Cybele group asteroids share the characteristics of their largest members. Is water ice present? Is it accompanied by organics? We also combine our observations, spanning several wavelength regimes to paint a greater picture of asteroid composition. Unraveling these questions will help us to begin to answer some of the big picture questions proposed by NASA related to life and the evolution on life here on Earth.

1.1 The Dissertation

This work consists of four projects: 1) our interpretation of near-infrared (2-4 μm) spectra of primitive asteroids; 2) our interpretation of the mid-infrared (8-14 μm) spectra of asteroids for which we obtained near-infrared spectra; 3) the link between visible, near- and mid-infrared 8-13 μm spectra of asteroid types; and 4) the near- and mid-infrared spectra (2-16 μm) of laboratory simulated asteroid organics.

1) Using remote sensing in near-infrared 2-4 μm region, our main motivation was to continue our characterization of primitive asteroids in the Themis dynamical family and the Cybele group. The Themis family [18] is comprised of dark, compositionally primitive bodies, and this popula-

tion resides in the outer Main Belt at a heliocentric distance between ~ 3.1 and ~ 3.2 AU. Cybele group objects are situated between the main-belt and Jupiter Trojan asteroids around 5 AU, two populations of primitive asteroids that have been studied by researchers in more detail. In the Themis family hydration has been observed in the form of hydroxyl-bearing minerals and water ice, yet very few asteroids have been observed in this diagnostic 2-4 μm region. After our discovery of water ice and organics on the surfaces of asteroids (24) Themis [1] and (65) Cybele [3], we continued to investigate members of the Themis family by focusing on asteroid (90) Antiope [17]. Similar to (24) Themis we discovered the signatures of water ice and organics on Cybele group asteroid (65) Cybele, the asteroid for which this dynamical group of asteroids is named. This spurred our investigations of other Cybele group asteroids (107) Camilla, (121) Hermione, and (790) Pretoria. With this study our motivation was to determine if other members of the Themis family and Cybele group had 3- μm features indicating OH- or H₂O-bearing minerals and/or widespread organics on their surface.

2) Of the asteroids for which we obtained near-infrared 2-4 μm spectra we analyzed their available mid-infrared 8-13 μm spectra that was obtained by the Spitzer Space Telescope. Our motivation is to constrain the processes and products of hydration in primitive asteroids by using a combination of their visible, near-infrared, and mid-infrared spectra. Although we did not obtain visible spectra of these asteroids we use diagnostic spectral features at these wavelengths reported by other researchers, such as the 0.7 μm features. We hypothesize that hydration products and processes are affecting the 0.7 μm , 3- μm , and 8-13 μm spectra of asteroids and that we can constrain these by incorporating the three wavelength regions. We also predict that hydration

processes are changing the spectra of asteroids in the visible and near-infrared and are also affecting the shape, strength, and slope of mid-infrared spectra as a result of grain size and/or porosity changes caused by the aqueous processing.

3) We have averaged the 8-13 μm Spitzer spectra of select asteroid taxonomic types, mainly Bus C-, D-, and S-types. With this study we intend to characterize the diversity in the shape and spectral contrast of emissions in this wavelength region, testing any possible links with asteroid taxonomy at visible wavelengths. We predict the combination of visible, near-infrared, and mid-infrared spectra will help us to constrain the thermal history of asteroids. More specifically that this combination of wavelengths will test that D-type asteroids have not been heated enough for aqueous alterations and conversely, that the C-types have.

4) In a laboratory we simulated and characterized asteroid organics in the near-infrared (2-4 μm) range. Organics are widespread throughout the solar system and are present in the interstellar medium, the moons of giant planets, comets, and meteorites. It had been proposed that organics were also present in asteroids, though their detection remained elusive. In 2010 and 2011 we discovered the signatures of organics in the spectra of two main-belt asteroids: (24) Themis and (65) Cybele. Our motivation to simulate these asteroid organics was to provide us with a more detailed understanding of their likely molecular structure. We created several ice mixtures containing water and other starting materials that we believe may have been present in the solar system during the formation of asteroids. We have compared the spectra produced by our laboratory organics both quantitatively and qualitatively to the spectra of asteroids and other astronomical sources.

For the remainder of this chapter we list the remote sensing instruments we used for our observations of asteroids, and the targets of these ground-based and space-based observations. We also describe the laboratory facility in which we performed our experiments, and list our ice/organic starting mixtures. In Chapter 2 we provide details of asteroid taxonomy, the classes that were born out of these classification techniques, and the mineralogy and composition that we can infer from these asteroid classes. In Chapter 3 we discuss the results of our near-infrared study of primitive Themis and Cybele asteroids. In Chapter 4 we detail our mid-infrared investigations of the asteroids for which we obtained near-infrared spectroscopy. We also describe the results at these same wavelengths of asteroids belonging to the Bus C, D, and S taxonomic classes. In Chapter 5 we present the spectra and analysis of our laboratory simulations of asteroid organics, and our comparisons of the spectra of these organics with other relevant astronomical sources. Lastly we summarize the dissertation and discuss future work in Chapter 6.

1.2 Remote Sensing Instruments and Laboratory Facilities

To carry out our study of asteroids we used ground-based and space-based telescopes that operated in the near- and mid-infrared wavelengths. Additionally we used a laboratory facility uniquely equipped to spectrally investigate astronomically relevant ices and organics also in the near- and mid-infrared. The following is a brief overview of these instruments and facilities.

1.2.1 Infrared Telescope Facility

NASA's Infrared Telescope Facility (IRTF) is 3.0 m telescope located on Mauna Kea in Hawaii, and operated by the University of Hawaii. At the time of our observations the suite of instruments included NSFCAM, a 1-5.2 μm camera, CSHELL, a 1-5.5 μm high-resolution ($R = 5,000\text{-}40,000$) spectrograph, and SpeX [19], a 0.7-5.3 μm a low- to medium-resolution ($R = 50\text{-}2,500$) spectrometer.

For all of our objects we chose the SpeX instrument [19]. SpeX is a medium-resolution ($R=800$), 0.8-5.5 μm cross-dispersed spectrograph and imager for the NASA IRTF. This instrument has the capability to obtain cross-dispersed spectroscopy across 0.8-2.4 μm , 1.9-4.2 μm , or 2.4-5.5 μm , using either a 0.3", 0.5", 0.8", 1.6", or 3.0" slit width. There is also a prism mode that covers the 0.8-2.5 μm wavelength range with a resolution ($R=200$) that is applicable for faint objects and occultation spectroscopy. Of the available modes we selected the LXD 1.9, which allowed us to observe our objects in the 1.9-4.2 μm range. At these wavelengths we are able to detect absorption features diagnostic of composition and mineralogy, and thus the SpeX instrument was crucial to our investigation of asteroid hydrated minerals and organics.

1.2.2 Spitzer Space Telescope

NASA's Spitzer Space Telescope was launched on August 25, 2003 into an Earth-trailing solar orbit. During its five and a half year cryogenic lifetime, Spitzer made over five hundred spectral

and photometric observations between 3 and 180 μm [20]. These data are now publicly available through the Spitzer Heritage Archive (SHA) an interface to the Infrared Science Archive (IRSA), which is part of the Infrared Processing and Analysis Center (IPAC).

From its vantage point Spitzer is unimpeded by the problems related to Earth’s atmosphere that normally plague ground-based spectroscopy. Spitzer incorporates three scientific instruments: 1) the Infrared Array Camera (IRAC) that operates simultaneously at four wavelengths (3.6 μm , 4.5 μm , 5.8 μm and 8 μm); 2) The Multi-band Imaging Photometer for Spitzer (MIPS), which uses three detector arrays for far-infrared (24 μm , 70 μm and 160 μm) observations; and 3) The Infrared Spectrograph (IRS).

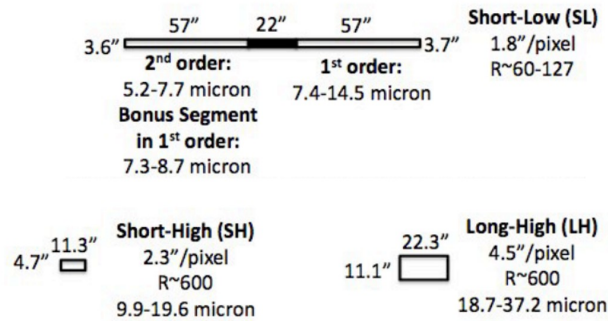


Figure 1.1: **Spitzer IRS Slit Apertures.** A schematic of the slit apertures used by the SL, SH and LH modules. For each module (and in the case of SL for each order), Spitzer takes spectra at 33% and 66% along the length of the slit. Adapted from Spitzer IRS Instrument Handbook (<http://irsa.ipac.caltech.edu/data/SPITZER/docs/irs/irsinstrumenthandbook/1/>)

All of the Spitzer observations we incorporated into this study were observed by IRS. The IRS is comprised of four distinct modules: Short-Low (SL), Short-High (SH), Long-Low (LL),

and Long-High (LH). Figure 1.1 shows a schematic of the slit apertures used. Combined, these modules provide low ($R \sim 60-130$) and moderate ($R \sim 600$) resolution in the $5-38 \mu\text{m}$ wavelength range. Each of the long slit apertures used by the low resolution modes (SL and LL) are divided into two in-line sub-slits that allow Spitzer to obtain spectroscopy in either the first or second order. The standard observing procedure places the target at approximately $\sim 33\%$ and 66% along the length of these sub-slit for the SL and LL modules, and slits in the case of the SH and LH modules. This automatic nodding provides the user with redundant observations of the object in the case of cosmic ray hits and detector artifacts.

The SL module covers the $5.2-14.5 \mu\text{m}$ spectral range in two orders (SL1: $7.5-15 \mu\text{m}$; SL2: $5-7.5 \mu\text{m}$), with a resolution range $R \sim 60-120$. The SL2 module also simultaneously produces a short “bonus” spectral segment (SL3) that spans the $7.3-8.7 \mu\text{m}$ region, slightly overlapping with both the SL2 and SL1 modules. The SL3 module is for normalizing the often disjointed SL2 and SL1 modules.

The LL module is most analogous to the SL module, as they share many similarities. The LL module covers the $14-38 \mu\text{m}$ spectral range in two orders (LL1: $20-38 \mu\text{m}$; LL2: $13.9-21.3 \mu\text{m}$) with a resolution range of $R \sim 57-126$. The LL2 order also produces a “bonus” spectral segment ranging from $19.2-21.6 \mu\text{m}$, which is for normalizing the often disjointed LL2 and LL1 modules.

The SH module covers the $9.9-19.6 \mu\text{m}$ region with a resolution $R \sim 600$, and shares a small overlap in wavelength with the LH module, which covers a range of $18.7-38 \mu\text{m}$ with a similar resolution as SH.

1.2.3 NASA Ames Laboratory of Earth and Space Sciences

As part of the Graduate Student Research Program we had access to The Laboratory of Earth and Space Sciences at the NASA Ames Research center. Here we carried out several laboratory studies, under the supervision and guidance of Dr. Scott Sandford. The Laboratory of Earth and Space Sciences has an extensive variety of equipment that can be used to make and characterize gas, ice, and solid substances under conditions relevant to a wide variety of astrophysical environments. The equipment at this facility includes a glass line for sample preparation, and six high vacuum cryogenic systems that routinely operate in the 10^{-8} mbar range. Each experimental chamber is equipped with a closed cycle helium refrigerator that can operate continuously between room temperature and approximately 15 K, and a dedicated microwave-powered, hydrogen flow, discharge lamp for the production of UV radiation. Additional lamps (deuterium, Xe, Hg) are also available if needed. These systems make it possible to create astrochemically-relevant gas phase and solid samples in simulated astrophysical environments across a broad range of pressures, temperatures, and radiation fluxes.

The Astrochemistry Laboratory has a variety of analytical instruments with which researchers are able to characterize samples within the vacuum chambers under specific environmental conditions. Particularly relevant to this study are four systems equipped with Fourier Transform infrared spectrometers (one Nicolet and three Bio-Rad) that are collectively capable of studies across the spectral range from 17,000 to 50 cm^{-1} ($0.6\text{-}200\text{ }\mu\text{m}$) with resolutions as good as 0.33 cm^{-1} . These

systems are routinely used by researchers to study the infrared spectra of a wide range of organic and ice materials of astrophysical relevance.

1.3 Asteroid Targets and Laboratory Samples

1.3.1 Near-Infrared

Table 1.1: Asteroids Observed with The Infrared Telescope Facility in the 2-4 μm Region

<i>Asteroid</i>	<i>Tholen, Bus</i>	<i>Population</i>	<i>Diameter (Km)</i>
(24) Themis	C, B	Themis Family	198
(65) Cybele	P, Xc	Cybele Group	237
(90) Antiope	C, C	Themis Family	120
(107) Camilla	C, X	Cybele Group	223
(121) Hermione	C, Ch	Cybele Group	209
(790) Pretoria	P, –	Cybele Group	170

Columns indicate the object, Bus and Tholen taxonomic type, population, and object diameter.

The asteroids that we observed in the near-infrared are listed in Table 1.1. We chose these targets for several important reasons. All objects are considered by the community to be primitive in nature. Although they have visible geometric albedos less than 10%, they were large enough that their absolute magnitudes were less than the limiting magnitude observable by the IRTF's SpeX

instrument. Also, at the time of the observations, none of the objects had been observed previously in the 2-4 μm region.

1.3.2 Mid-Infrared

In the 5-14 or 5-38 μm region, Spitzer observed five of the six asteroids for which we obtained spectra in the near-infrared, including (24) Themis, (65) Cybele, (90) Antiope, (107) Camilla, and (121) Hermione. Spitzer did not observe asteroid (790) Pretoria. We also selected Spitzer spectra of asteroids belonging to particular taxonomic classes for our investigation into the relationship between visible, near-, and mid-infrared spectra.

1.3.3 Laboratory Samples

For this study we chose to focus on mixtures of aliphatic and aromatic hydrocarbons that would be relevant to our detection of organics on (24) Themis and (90) Antiope. We chose alkanes for the aliphatic component of our starting mixtures. Alkanes are saturated hydrocarbons, consisting of carbon and hydrogen with all bonds being single bonds. We varied the alkane length (propane to decane) to sample a wide range of $-\text{CH}_2-/-\text{CH}_3$ ratios. For the aromatic component we chose naphthalene, the simplest polycyclic aromatic hydrocarbon. Our laboratory mixtures are presented in Table 1.2.

Table 1.2: Laboratory Samples Prepared at the NASA Ames Astrochemistry Laboratory

<i>Experiment</i>	<i>Explanation</i>
$\text{H}_2\text{O} + \text{C}_{10}\text{H}_8 + \text{C}_3\text{H}_8$	Water + Naphthalene (aromatic) + Propane (aliphatic)
$\text{H}_2\text{O} + \text{C}_{10}\text{H}_8 + \text{C}_6\text{H}_{14}$	Water + Naphthalene (aromatic) + 3-methylpentane (aliphatic)
$\text{H}_2\text{O} + \text{C}_{10}\text{H}_8 + \text{C}_6\text{H}_{14}$	Water + Naphthalene (aromatic) + Hexane (aliphatic)
$\text{H}_2\text{O} + \text{C}_{10}\text{H}_8 + \text{C}_{10}\text{H}_{22}$	Water + Naphthalene (aromatic) + Decane (aliphatic)

Columns indicate the chemical formulae for each laboratory-created gas mixture, as well as the standard nomenclature.

CHAPTER 2

ASTEROID TAXONOMY AND MINERALOGY

Taxonomy is a crucial tool used in many fields of science. In biology all of the earth's organisms are grouped based on shared physical characteristics. In chemistry all 118 elements known to man can be classified into Metalloids, Metals, and Non-metals, with many subgroups therein. The field of astronomy is no different. Stars are grouped according to their spectra [21] [22], galaxies according to their shape [23] [24], and comets according to their orbital periods and composition. Since the discovery of the first asteroid in 1801 [25], it would only be a matter of time until observers noticed similarities and differences between these small bodies, and the need for a taxonomic scheme was evident. This chapter describes the methods of the most successful asteroid taxonomy regimes, the asteroid classes that were born out of taxonomy, and the mineralogy that we can infer from these classes by our investigations at multiple wavelength regions.

2.1 Taxonomy of Asteroids

Asteroid colors and spectra can be used to identify statistically significant taxonomic groups that share specific spectral characteristics. These groups can then give us insight into the mineralogy of asteroids, which can be an important tracer of processes such as aqueous, collisional, and thermal

history. Two asteroid taxonomies are widely used today, the Tholen [26], and Bus [7] taxonomies. Both taxons largely use the visible spectra of asteroids to define distinct classes. The visible is home to many features directly related to asteroid mineralogy. These features indicate minerals and mineral assemblages, and arise due to crystal field theory and charge transfer mechanisms [27]. Asteroid taxonomy is not based on the composition of asteroids, but rather principle component analysis of their spectra, which groups asteroids with similar spectral features. For example, Tholen (1984) [26] used this novel technique of principle component analysis on approximately 500 asteroids observed by the eight color asteroid survey (ECAS). Each object's spectrum consisted of eight photometric points ranging from $0.3 \mu\text{m}$ - $1.1 \mu\text{m}$ [28] (a range slightly below the visible into the UV, and slightly above the visible into near-infrared) to sample expected features and continuum slopes at these wavelengths. The analysis of Tholen (1984) distilled the multi-dimensional information contained within the independent color indices into just two principal components, PC1 and PC2. This procedure led to fourteen asteroid classes: C, G, B, F, D, S, R, A, M, P, Q, E, V, and T.

Tholen's approach to asteroid classification remained the standard for over a decade. Since 1984 advances in our technology introduced other tools for observation, including high throughput spectrometers and charge-coupled devices (CCDs). Applications of these new technologies are the Small Main-belt Asteroid Spectroscopic Surveys, SMASS [29] [30] and SMASSII [7] [31] [32] in which observers out of the Massachusetts Institute of Technology obtained the visible spectra of 1447 asteroids. This database represented the largest of its kind, over three times larger than that used by Tholen (1984). The goal of SMASSII was to extend the robust Tholen classifica-

tion using higher resolution spectra and significantly more objects. Though the spectral coverage of SMASSII (0.44 μm -0.92 μm) consisted of a more narrow wavelength range than ECAS (0.3 μm -1.1 μm). In other words, only four of the eight filters used in Tholen taxonomy overlapped the wavelength range used by SMASSII. Despite these wavelength limitations, Bus (1999) used principal component analysis in an effort to maintain consistency with the Tholen taxonomy [33]. Bus' first principle component, PC1, was a linear fit to the slope of each spectra. The second, PC2, was sensitive to the presence and strength of a 1 μm feature, indicative of olivine and pyroxene. The third principle component, PC3, was diagnostic of objects with 0.55 μm and 0.7 μm features both suggestive of phyllosilicates.

Their 3-principle component analysis led to a new feature-based taxonomy in which twenty six asteroid classes were defined. The main classes include C, S, X, T, D, Ld, O, and V with various subgroups contained therein. The significance of this work remains in the higher resolution data used, allowing the detection of features not otherwise seen by ECAS, and thus resulting in a more diverse classification system than Tholen.

In 2009, the Bus taxonomy was expanded upon by DeMeo et al. (2009) to include reflectance spectroscopy of 371 asteroids in the 0.8-2.45 μm region [34]. An extension of the Bus asteroid taxonomy into the near-infrared). Using the same analysis techniques of Bus (1999), DeMeo (2009) introduced a system to classify objects using the diagnostic infrared wavelengths. They found that the classes of most objects originally determined by Bus (1999) remained, though several objects changed classes due to spectral details revealed only in the near-infrared. This work showed the

importance of combining multiple wavelength regimes to more thoroughly understand the range of spectral characteristics that asteroids of a particular class may exhibit.

Although taxonomy is useful for characterizing similarities and differences in the visible spectra of asteroids, it is not diagnostic of the mineralogy or composition of asteroids that lack strong features in the visible, which is the case for most primitive asteroids. Thus we must incorporate spectra of these bodies at multiple wavelengths. The next subsections introduce the spectral characteristics of asteroid types in addition to the mineralogy and composition we can infer from diagnostic spectral features in the visible plus the near- and, mid-infrared.

2.2 Asteroid Types: The Formal Definition

Although several taxonomic systems exist, this work focuses on the Bus classification of asteroids. The average visible spectra of asteroids belonging to the Bus C, D, and S taxonomic types are shown in Figure 2.1. In Bus taxonomy C-types exhibit spectra characterized with a weak to medium absorption at wavelengths shortward of $0.55 \mu\text{m}$, and are neutral to slightly reddish and featureless longward of $0.55 \mu\text{m}$. Ch asteroids have spectra similar to C-types, with a shallow absorption centered near $0.7 \mu\text{m}$. The B-types have a linear, featureless spectrum with bluish to neutral slope. The Cb-types are similar to B-types with a neutral to slightly reddish slope. Cg-types have a strong UV absorption at wavelengths shortward of $0.55 \mu\text{m}$, and are featureless with neutral to reddish slope longward of $0.55 \mu\text{m}$. Sharing a similar spectrum to the Cg asteroids are the Cgh-types, with shallow absorption centered near $0.7 \mu\text{m}$.

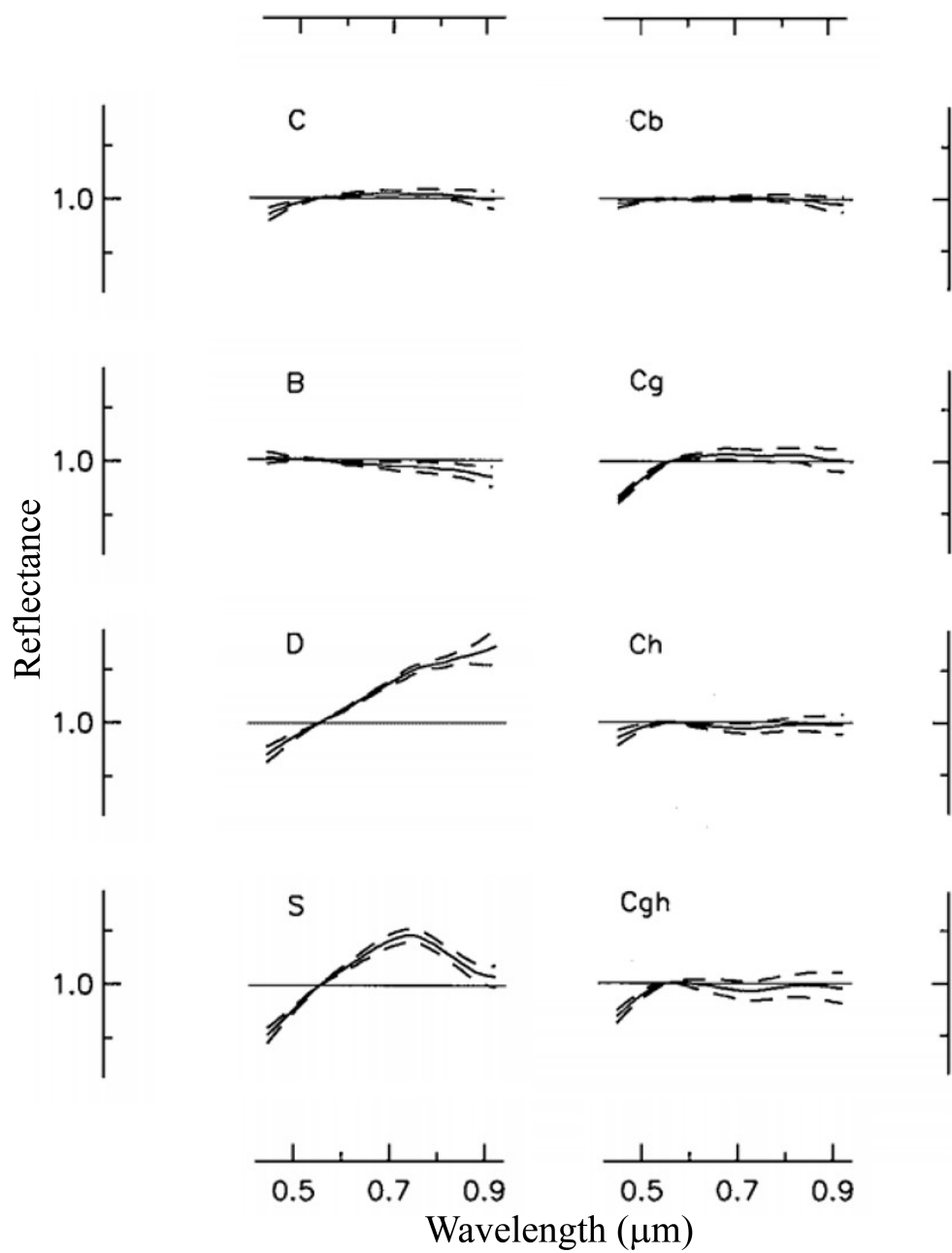


Figure 2.1: **SMASS visible spectra of selected asteroid classes.** Characteristic visible spectra of asteroids belonging to the Bus C, D, and S taxonomic types. The C-class includes C-, B-, Cb, Cg-, Ch-, and Cgh- types. Adapted from [7]

Although there exist many asteroid types as defined by the Bus taxonomic systems, this study focuses on the Bus C-, D-, and S-types. The C- and S-types have several subtypes, for example the B-types which belong to the larger C-complex classification. We consider all members of the C class and will therefore refer to this as the C-complex. When referring to S-types we are only considering the S classification and not the S-complex as some members, such as S(IV), may be more primitive than other members.

2.3 Mineralogy and Composition of Asteroid Types

2.3.1 The Wavelengths of Investigation

The current surface mineralogy of asteroids, is related to the initial composition of the parent body, and to the composition of the solar nebula in the region it formed, which is dependent upon heliocentric distance and other factors. Over the lifetime of the solar system the starting mineralogy of asteroid parent bodies has been modified by both exogenic and endogenic processes. These internal processes include heating, metamorphism, partial or complete melting, differentiation, or aqueous alteration, while external processes involve regolith formation, shock, cratering events, and collisional disruption [35]. These alterations leave tell-tale signatures detailing an evolutionary history of the mineralogy and composition of asteroids that we can attempt to decipher using spectroscopy.

One such way we can interpret these diverse mineralogies is to determine the presence, abundance and composition of known mineral species in the absorption or emission spectra of asteroids. Using visible and visible-near-infrared reflectance spectroscopy, typically in the 0.4-1.0 μm and 1.0-2.5 μm regions, respectively, we can identify both individual minerals and mineral assemblages [36]. In these wavelength regimes there are two general classes of minerals that produce absorption features that dominate both asteroid and meteorite spectra: these are 1) minerals containing iron or other transition metals such as nickel, cobalt, copper, and titanium [35]; and 2) silicates, including pyroxene, olivine, feldspar, and OH- and H₂O-bearing minerals.

The near-infrared 2.5-5.0 μm region is well suited to our studies of several astronomical sources, including relatively low temperature objects ($T < 2,000\text{K}$) such as asteroids and comets [19]. This diagnostic wavelength region includes important spectral features. The most notable features we find here are the vibrational and rotational bands of astrophysically relevant molecules such as CO, CH, HCN, CN, NH, OH, H₂O, CH₄, etc; the pure rotation transitions of H₂, ionic and atomic transitions; and several solid state bands that are imperative for our determination of the composition of ices, dust and the surfaces of small bodies, such as asteroids and comets [19].

Using mid-infrared spectroscopy, most commonly defined between the wavelengths 5-40 μm , we can not only probe at the dominant surface composition of asteroids but also their surface temperatures and textures. This wavelength regime is important for asteroid classes that are typically featureless at shorter wavelengths such as the D-types. As in the visible and near-infrared, there are a host of interesting features found in this wavelength regime. For example, the second most intense molecular vibration of H₂O, known as the H₂O-bend fundamental, occurs around 6.1 μm

and is an indicator for the presence of water [37]. The Si-O stretch and bend fundamentals, silicon's strongest molecular vibrations, occur around 10 and 20 μm , respectively, and are sensitive to the presence of silicates, the size of surface grains [38], and surface porosity [39]. There are also a multitude of strong emission features due to Polycyclic Aromatic Hydrocarbons (PAHs) around 6.2, 7.7, 8.6, 11.3, and 12.7 μm [40] that have been detected throughout our solar system. The photoproducts (alcohols, quinones, and ethers) produced by the UV irradiation interstellar ices containing PAHs can also be observed in the mid-infrared [41].

2.3.2 Asteroid Superclasses

The spectral features we detect, largely in the visible and infrared, can detail the likely thermal history of an object. Since objects with similar spectral characteristics often belong to the same class we can often infer the average thermal history of each class. For example Bell (1986, 1989) grouped asteroid types into three main classes or superclasses: primitive, metamorphic, and igneous. The primitive types have undergone very little heating, the metamorphic class have been heated enough to cause spectral changes, and igneous objects experienced extreme temperatures, and were formed via the melting of materials.

Primitive asteroids typically belong to the C-, and D-classes with some members in the X class. These asteroid types have the darkest surfaces compared to other asteroid types, with geometric albedos, p_v , typically less than 10%. In the visible wavelength region (0.4-0.9 μm) primitive asteroids exhibit a range of spectral slopes. The B-types typically show a blue to neutral slope, the

C-types a neutral to slightly red slope, and the P- and D-types exhibit the reddest slopes. Although their visible spectra is relatively featureless, there are subclasses of the C- and X-types that show features between 0.5 and 1.3 μm due to charge transfers in iron oxides. These phyllosilicates features are found in Cg-, Ch-, Cgh- and Xc-types that have spectra exhibiting features shortward of 0.55 μm , centered around 0.7 μm , or longward of 0.85 μm , which are generally attributed to hydration by the community [42].

It is not surprising that the most aqueously altered and thus thermally processed of the primitive asteroids belong to sub-members of the C class. The heliocentric distance at which they formed played a crucial role in their current state of hydration. The C-types, including B-types (metamorphic), are located in the middle ($\sim 2.5\text{-}2.8$ AU) and outer ($\sim 2.8\text{-}3.2$ AU) main asteroid belt, though are predominately in the middle regions [43]. These objects were likely thermally altered by our primordial sun and/or ^{26}Al that they accreted during formation that melted any surface and/or subsurface water ice. B- and C-type asteroids, although they exhibit relatively featureless spectra at visible wavelengths, often show an array of absorptions in the near-infrared, including those implicating hydrated minerals (especially phyllosilicates), water ices, and even organics [1] [2] [5]. These absorption features present in the spectra of some primitive asteroids indicate that these bodies have undergone some thermal processing, though not sufficient enough to completely remove all hydration products.

Beyond these bodies are the more primitive D-types asteroids and members of the X-class. These objects likely did not accumulate as much ^{26}Al or were not subject to significant primordial solar heating, thus are less aqueously and thermally altered. These populations largely reside from

the middle to beyond the outer belt, with roughly 40% of primitive X-types (old P-types) found in the Cybele group centered at 3.5 AU, and 75% of the D-types located in the Trojan population around 5 AU [43]. At these distances the parent bodies of the D-types and some members of the X-class also accumulated water ice, similar to the C-types, but did not experience heating sufficient to melt this ice as evident by their completely featureless visible spectra, where many features due to aqueous alteration typically occur. Water ice has been detected on several X-types, including (65) Cybele [3] [5]. Water ice has not yet been detected on a D-type asteroid. Although it is believed by the community that D-types may still harbor this ice within their interiors, and their extremely red visible spectra indicate these objects are likely rich in organic material [44]. Thus many parallels have been drawn between D-types and comets.

Igneous asteroids typically include V-types and some members of the S and X classes. These bodies experienced significant heating that induced extreme compositional changes. The most important features we detect are crystal field absorptions due to the presence of transition ions in metals, most commonly Fe^{2+} , that are located in certain crystallographic sites in Fe- and Mg-bearing silicate minerals such as pyroxene and olivine [45]. Olivine has a characteristically wide and prominent absorption feature at $1 \mu\text{m}$ arising from Fe^{2+} cations in specific crystallographic sites. Pyroxene also has an absorption feature at $1 \mu\text{m}$, though it can be distinguished from olivine as it produces another feature at $2 \mu\text{m}$. The band centers of these features can shift with varying amounts of Ca^{2+} and Fe^{2+} . Feldspar, another high-temperature mineral, has a characteristic feature at $1.2 \mu\text{m}$. The presence of these important features points to a metamorphic and/or igneous past, consistent with complete or partial melting of these asteroid types [46].

2.3.3 Meteorites

When considering the composition and taxonomy of asteroids, it is appropriate to mention these for meteorites, which are small fragments from asteroids that have been delivered to Earth. Meteorites can be divided into three overall categories: iron, stony-iron, and stony. Relevant to this study are the stony types that can be further classified into chondrites, which consist of both ordinary chondrites and carbonaceous chondrites. Carbonaceous chondrites are the most primitive and unaltered meteorites, with elemental compositions similar to the solar nebula. These primitive meteorites are believed by the community to originate from dark, primitive asteroids. Carbonaceous chondrites include CI, CM, CO, CV, CR, CK, CH and CB types, grouped as such based on shared physical, chemical, isotopic and mineralogical properties. All of these types can have a numerical assignment following the group name that denotes the amount of secondary processes such as aqueous alteration and thermal metamorphism that it has experienced. Petrologic types 1-2 describe the degree of aqueous processing, and types 3-6 detail the degree of thermal metamorphism.

Although several types of chondrites exist, this study will focus on the CI, CM and CR types. The CI types thus far are all type 1, having experienced the most aqueous alteration and the least thermal modification. As a result of this aqueous processing they do not possess any chondrules, however up to 20% of their weight is water, and they contain a plethora of aqueously altered minerals, such as phyllosilicates and magnetite. They are also rich in complex organic materials. CIs have not been heated above $\sim 50^{\circ}\text{C}$, indicating they likely came from parent bodies that condensed in the cold outer regions of the solar system. CM meteorites are largely petrologic type 2, and as a

result do exhibit chondrules. They contain less water than CIs, up to about 10%, and are similarly rich in complex organic materials and magnetite. Like CMs, CRs are also mainly petrologic type 2, and contain chondrules, water, hydrated silicates, and magnetite. However, they differ from CMs in that they have up to $\sim 10\%$ reduced metals in the form of nickel-iron and iron sulfides.

CHAPTER 3

EVIDENCE FOR HYDRATED MINERALS AND ORGANICS IN THE NEAR-INFRARED

The origin of Earth's water, crucial to all life here on Earth, remains a mystery. Earth, like the other inner solar system planets, likely accreted from the driest materials in the solar nebula. Although if any water was accreted during Earth's formation the differentiation process of the early Earth and/or the moon impact event likely destroyed it. Thus the question remains how Earth is covered in roughly 75 % water, with possibly more undiscovered water deep within the mantle. There are several theories that explain the origin of this water. One hypothesis describes an extraterrestrial origin, in which water ice was incorporated into comets and asteroids during the formation of these objects, and was then delivered to Earth by impacts about 4 billion years ago.

This chapter investigates several objects analogous to those that may have "seeded" the Earth with an abundance of water. Understanding the hydration state of asteroids is important for us to estimate the water inventory these objects may have contributed to Earth. We have observed several members of the Themis family and Cybele group. Our goal is to understand if other members of these populations are representative of the largest members, which have the signatures of water ice and organics. Studies of this nature will help to quantify the prevalence of water ice and organics in the outer main belt, and may be related to the origin of water and life on Earth.

3.1 Introduction

To prove or disprove this "seeding" of the Earth by hydrated objects researchers have been investigating the "3 μm " feature, indicative of the hydration state of primitive asteroids, for several decades. Jones et. al (1990) and Britt et al. (1992a), found many C-types, including one B-type, had hydrated silicates present on their surfaces [44] [47]. Florczak et al. (1999) detected evidence of aqueous alteration on 15, and possibly up to 26, of the 35 members they studied belonging to the Themis family. Further investigation, and improvements in spectral resolution revealed that there were various forms of the 3 μm " feature, implying different degrees of thermal processing. For example, in 2002 Rivkin et al. discovered this diversity in the shape of the 3 μm absorption, and classified the two variations as "sharp" and "rounded", arising from O-H dominated minerals and H₂O dominated minerals, respectively[16]. The asteroids with "sharp" features included SMASS Ch- and B-types, while the asteroids with "rounded" absorptions included two SMASS Xc-types. [16].

More recent studies of hydration in primitive asteroids by Campins et al. (2010) and Rivkin and Emery (2010) reveal a "rounded" 3 μm water-ice feature in the spectra of asteroid (24) Themis, an SMASS B-type [1] [2]. A similar absorption was seen by Licandro et al. (2011) in the spectra of (65) Cybele, an SMASS Xc-type [3]. This feature was concluded by these authors to be the result of the symmetric stretch mode of water molecules in ice. These were the first detections of their kind and spurred more investigations to follow. A larger examination by Takir and Emery (2012) revealed fifteen asteroids with the "sharp" 3 μm absorption [5]. The sharp group consists

of largely C-types (including Chs and one B), one Xc, and one T-type. The rounded group only applied to six asteroids, sampling mainly SMASS X-types.

This study investigates six outer main belt asteroids in the 2-4 μm region. We characterize the presence and shape of the 3 μm feature, and the presence of organics. Our targets belong to the C and X taxonomic classifications, and are likely primitive objects with OH- or H₂O-dominated minerals.

3.2 Asteroid Observations

For our asteroid, standard star, and solar analog observations, we used SpeX [19]. We selected the Long Cross-dispersed (LXD) 1.9 mode that produced medium-resolution spectra in the 1.9- to 4.2- μm wavelength range. We chose the 0.8 x 15 arcsec slit with an image scale of 0.15 arcsec/pixel that resulted in a spectral resolution $R \sim 800$. We obtained the spectra in A-B (object-sky) pairs by nodding the telescope 10 arcsec along the long dimension of the slit.

For all observations we followed a similar procedure of data acquisition. First, we began by running macros that took arc and flat exposure frames, useful later for our data reduction procedure. We then obtained spectra of the solar analog and the standard star closest to our object in right ascension (RA) and airmass before moving to the asteroid. We carefully selected standard stars that were not only close in RA to our asteroid, but also had a similar airmass. This would allow for optimal modeling and correction of atmospheric extinction. The standard star is also used to assign physical flux units to the detected counts in the extracted spectra of our objects. We repeated this

process of acquiring calibration frames, stars, then asteroid frames several times for each observing run. In Table 3.1 we list all of our relevant observing details.

3.2.1 (24) Themis

We observed asteroid (24) Themis on January 23, 2008 UT. This night was photometric with good transparency and a seeing of approximately 0.6 arcsec. We observed Themis from its transit to almost 1.7 airmasses. In between each of the eight sets of Themis observations we obtained arc and flat spectra, as well as spectra of solar analog star HD 28099 [48] [49] and standard star BS 1358. We selected this particular solar analog for two reasons: 1) it was shown by Cayrel de Strobel (1996) to be a reliable solar analog, and 2) it was very close in RA to Themis [49]. The standard star BS 1358 also had a similar RA to this asteroid. Since Themis was relatively bright, with a magnitude of 12.69, we chose an exposure time of 30 seconds with one cycle and five co-adds. In total, we acquired eight sets of spectra for Themis, with each set consisting of on average 11 AB pairs.

3.2.2 (65) Cybele

We observed asteroid (65) Cybele over the course of two nights, September 08-09, 2009 UT. The heliocentric and geocentric distances of this object were 3.37 and 2.36 AU, respectively, and the phase angle was 0.6 degrees. The first night we estimated a seeing of roughly 0.55 arcseconds.

There were cirrus clouds and low humidity, approximately 0.3%. We observed solar analogue stars 51 Pegasus and HD 42618, and G Landolt stars [50] SA113_274 and SA115_271 throughout the night covering similar airmasses as Cybele. The following night was clear with a seeing of roughly 1.0 arcseconds. We observed similar solar and standard stars as the previous night.

3.2.3 (90) Antiope

We observed asteroid (90) Antiope on two independent occasions, the first of which was the night of July 23, 2006 UT. This particular night had high clouds, high amounts of atmospheric water, and a seeing of approximately 0.7 arcseconds. We acquired two sets of Antiope spectra, each consisting of an average of 16 AB pairs. For the first and second set of spectra we chose an exposure time of 30 seconds, though with two co-adds/two cycles and one co-adds/sixteen cycles, respectively. Additionally we obtained spectra of HD 14786, a near-solar spectral type G5 star, which had a similar airmass and RA as Antiope.

Our second observation of Antiope was on the night of January 23, 2008 UT, the same night we observed asteroid (24) Themis. We took spectra of Antiope from approximately -1.1 to 1.4 airmasses. In between each of the four sets of observations we obtained spectra of the standard star BS 2962 that we selected as it shared a similar airmass and RA as Antiope.

3.2.4 (107) Camilla

We observed asteroid (107) Camilla the night of June 6th, 2009 UT. We also observed solar analog HD 153631, a spectral type G0, and HD 163840, also a G0.

3.2.5 (121) Hermione

We observed (121) Hermione on, September 8th 2009 UT, the first night that we observed (65) Cybele. In addition we observed solar analogs and standards stars each night at similar airmasses as the asteroids. We used (51) Pegasus, spectral type G2, and HD 42681, spectral type A0, for (121) Hermione.

3.2.6 (790) Pretoria

We observed asteroid (790) Pretoria on September 09, 2009 UT, the second night that we observed (65) Cybele. The apparent magnitude was 12.9. We observed solar analogue stars 51 Pegasus and HD 42618, and G Landolt stars [50] SA113_274 and SA115_271 throughout the night covering similar airmasses as Pretoria.

Table 3.1: Asteroids Observed with The Infrared Telescope Facility (IRTF)

<i>Asteroid</i>	<i>Population</i>	<i>Tholen, Bus</i>	<i>Date (UT)</i>	<i>r (AU)</i>	Δ (AU)	α (deg)	<i>Magnitude</i>
(24) Themis	Themis Family	C, B	2008-Jul-23	2.74	3.54	11.72	12.69
(65) Cybele	Cybele Group	P, Xc	2009-Sep-08	3.37	2.36	0.27	11.20
			2009-Sep-09	3.37	2.36	0.51	11.24
(90) Antiope	Themis Family	C, C	2006-Jan-23	2.69	3.56	8.48	13.76
			2008-Jul-23	3.65	4.65	2.13	14.67
(107) Camilla	Cybele Group	C, X	2009-Jun-06	3.68	2.71	4.1	13.76
(121) Hermione	Cybele Group	C, Ch	2009-Sep-08	3.10	2.99	18.93	13.1
			2009-Sep-09	3.10	2.98	18.93	13.11
(790) Pretoria	Cybele Group	P, N/A	2009-Sep-08	3.15	2.26	10.3	12.93

Details of the near-infrared 2-4 μm observations using NASA's Infrared Telescope Facility. Columns indicate the object, population, Bus and Tholen taxonomic type, UT date of observation, heliocentric distance r in AU, observer-target-distance Δ in AU, sun-target-observer angle or phase angle θ_{STO} in degrees, and the object's apparent magnitude.

3.3 Data Reduction and Analysis

The following describes the methods we used to reduce our 2-4 μm asteroid spectra. The data reduction procedures include spectral extraction, removal of water vapor in the Earth's atmosphere, and modeling and subtraction of the thermal excess. Additionally, we analyzed our reduced asteroid spectra for the presence of a 3- μm feature in a systematic way, and we also detail the methods behind this analysis.

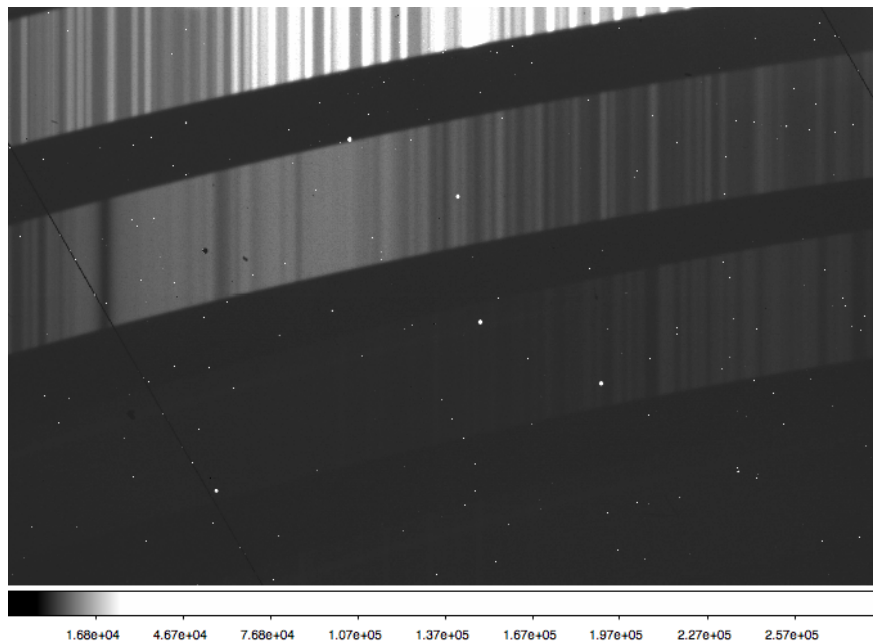


Figure 3.1: **Frame A of and an AB pair.** Frame A consists of signal from dark current, the telescope, the sky, and the target.

3.3.1 Spextool

All of our asteroid and star spectra were reduced using standard methods employed by other researchers studying point source objects in the near-infrared. The first step in this reduction procedure involves the Interactive Data Language (IDL) based spectral reduction program Spextool (v3.4) [51]. This routine accounts for the added complexity introduced by the crossed-dispersed spectrograph we used to acquire our data. For example, it corrects for the significantly curved spectral orders and variations in spacing between orders with position on the array.

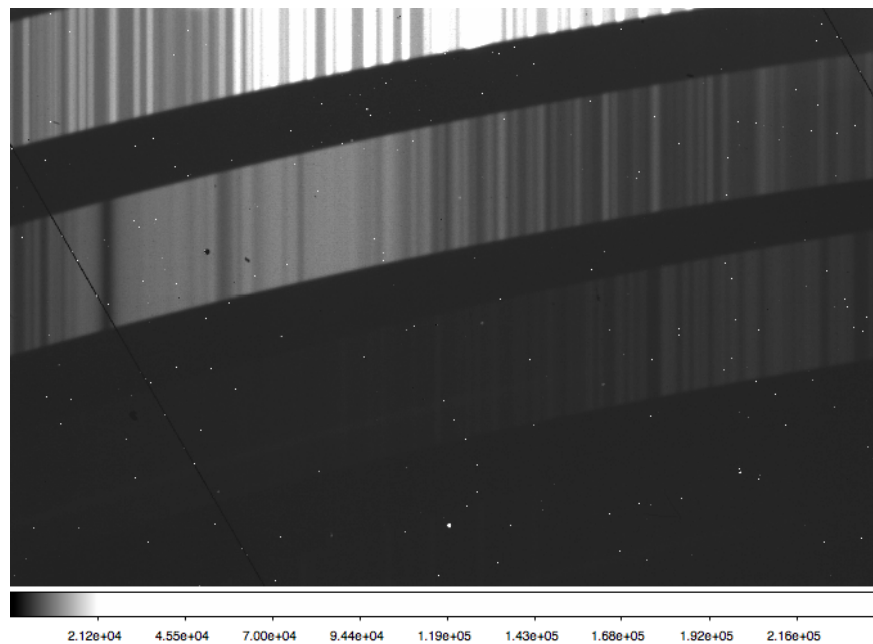


Figure 3.2: **Frame B of and an AB pair.** Frame B consists of signal from dark current, the telescope, and the sky. The target was not observed in this frame.

Summarizing from Cushing et al. (2004) Spextool’s reduction pipeline can be distilled into three main steps: 1) preparation of calibration frames (arcs and flats), 2) extraction of the spectra, and 3) post-extraction processing [51]. In preparing the calibration frames Spextool normalizes the flat field exposures, then combines them into one single exposure in order to increase the signal-to-noise ratio of the final product. Using the FITS header and this combined high signal-to-noise flat field exposure, Spextool locates the spectral orders on the array. The routine then normalizes the combined flat field image to unity. To process the arc frames in LXD mode, Spextool subtracts the “arc off” frame from the “arc on” frame to remove signal from atmospheric OH and thermal emission from both the sky and telescope. The resulting arc frame is then divided by the sky as given in the equation

$$sky = (A + B) - |(A - B)|, \quad (3.1)$$

where A is

$$A = \text{dark current} + \text{telescope signal} + \text{sky signal}_a + \text{target} \quad (3.2)$$

and B is

$$B = \text{dark current} + \text{telescope signal} + \text{sky signal}_b. \quad (3.3)$$

The resulting sky-subtracted arc frames were then divided by the normalized flat field images.

For wavelength calibration Spextool uses two target frames (in AB mode) to produce a night-sky emission image. Spextool performs wavelength calibration by using a combination of emission lines from an Argon calibration lamp for shorter wavelengths and sky OH emission lines for longer wavelengths, since the number and intensity of Argon emission lines diminish rapidly longward of $3 \mu\text{m}$ where OH emission lines are plentiful. Calibration of LXD modes is performed using a number of sky emission lines for longer wavelengths, and Argon lines for shorter wavelengths. For those LXD orders (4 and 6) where the arc lines are either weak or absent, the sky emission image replaces the arc image.

We obtained spectroscopy of our objects in AB pairs. Figure 3.1 and 3.2 show an example of an A and B pair, respectively. To remove the background Spextool subtracts the B frame from the A frame (pair subtraction) that gives

$$A - B = target + sky_A - sky_B \quad (3.4)$$

$$A - B = target + R \quad (3.5)$$

where $R = sky_A - sky_B$, is the residual sky signal that the user can choose to remove later in the extraction process.

Spextool extracted the asteroid and star spectra by adding the flux for each channel within an aperture size defined by the user, which in this case was 10 pixels wide. Each pixel of the raw data frame is corrected for any nonlinearity using an iterative technique described in Vacca et al. (2004) [52]. After this correction, the data (total net signal) is converted to flux, by normalizing by the integration time, number of readouts, and number of co-adds. The extracted spectra then undergoes a post-processing routine to remove some telluric absorption features, combine the flux and error spectra from each aperture, and merge the LXD spectra. The result is a continuous spectrum across all orders.

3.3.2 ATRAN

All of our ground-based asteroid spectra were contaminated with telluric features from Earth's atmosphere. These strong features of CO₂ and H₂O can vary in depth depending on the local precipitable water vapor and airmass of the object. Therefore, we implemented the IDL routine ATRAN (Atmospheric Transmission of Near- and Far-Infrared Radiation) [53] that modeled then removed these telluric features from our asteroid and star spectra.

ATRAN is a set of routines written in IDL that computes the transmittance of Earth's atmosphere for wavelengths ranging from 0.8 μm to 10,000 μm [53]. ATRAN is particularly useful as

it has the ability to model both low- and high-resolution ($R = 10-10,000$) spectral profiles, which was applicable for our low-resolution 2-4 μm asteroid spectra.

For each spectrum ATRAN generated multiple models of atmospheric transmission using the altitude of the telescope, airmass of the object, spectral resolution, and a range of precipitable water vapor amounts. Included in the transmission models are contributions from mixed gases, water vapor, and ozone. ATRAN shifted each spectrum by each of the various atmospheric models generated for that spectrum and selected the model with a subpixel shift and water vapor amount that best removed the telluric features. The routine divided each corrected asteroid spectrum by both the corrected solar analog and standard star spectra. ATRAN fit polynomials to these resulting spectra, flagging any measured points that deviated significantly from the fit. These spectra (asteroid/solar analog and asteroid/standard) were median combined into a single, final spectrum. In all of our asteroid spectra we omit the strong telluric band between 2.45 and 2.85 μm .

3.3.3 Thermal Model

Long ward of approximately 3.3 μm primitive asteroids in the outer main belt typically show an increase in reflectance caused by the combination of both reflected light and thermal radiation from its surface. The onset and amount of the thermal component depends on the surface temperature of the object. The temperature of the surface is dictated by several factors including heliocentric

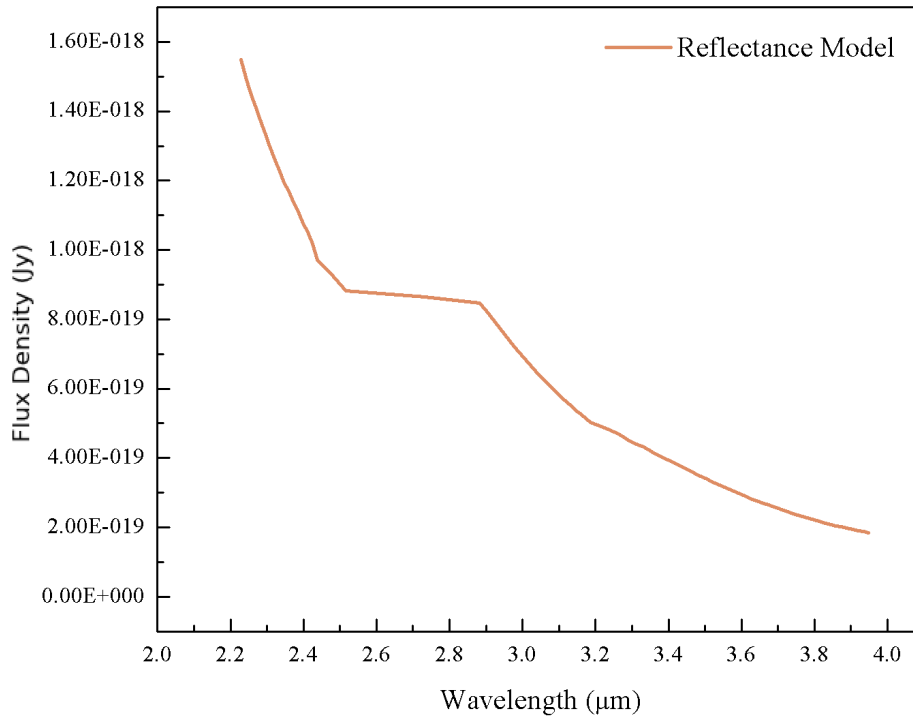


Figure 3.3: **Reflectance model for (121) Hermione.** A model of reflected light from the surface of asteroid (121) Hermione. The region between approximately 2.5 and 2.9 μm is the region of strong telluric absorptions in Earth’s atmosphere. Due to interpolation in this region there is a small artifact in the 2.9-3.1 μm region that produces a plateau rather than a smoothly decreasing reflectance. This artifact is of such small scale that it does not affect our data.

distance, and surface properties such as albedo, thermal inertia, and roughness. For example, a low albedo NEA at around 1 AU will have a considerable fraction of its total flux at 2.5 μm due to thermal emission [54]. A low albedo asteroid at around 3 AU, similar to those in this study, will typically have negligible thermal emission at this wavelength, instead the onset of the thermal

component is longward of $3.3 \mu\text{m}$ for all spectra presented here. Hence the thermal component does not affect our interpretation of the $3\text{-}\mu\text{m}$ features but it is still important to remove it. The thermal component adds slope to the reflectance data, making it difficult to compare the near-infrared spectra of objects at various heliocentric distances.

Thermal infrared observations can also be used to determine the diameter and albedo of asteroids. A refined standard thermal model (STM) was put forth by Lebofsky et al. [55] [56], and a vast majority of asteroid diameters and albedos have been derived using the STM [57] [58]. Because the STM assumes a non-rotating spherical object observed at 0° solar phase angle, it is not well suited to describing some asteroids that are irregularly shaped objects with lower thermal inertia, sometimes observed at large solar phase angles ($> 30^\circ$). A more flexible thermal model, the Near Earth Thermal Model (NEATM), was introduced [59] [58] in order to obtain diameter and albedo values in better agreement with those estimated by radar observations. The infrared beaming parameter η is an important variable in the NEATM, it can account for effects such as night side emission, thermal inertia, and surface roughness. In the STM η was previously held constant at 0.756. The NEATM, like the STM before it is built upon a modified blackbody formalism. While the STM required only one wavelength λ , the NEATM requires at least two. In the treatment of the thermal emission of these asteroids, we can determine the sub-solar temperature of the surface from

$$T_{ss} = \left[\frac{S_{\odot}(1-A)}{\varepsilon\sigma\eta} \right]^{1/4} \quad (3.6)$$

where S_{\odot} is the solar constant, A is the bolometric bond albedo, ε is the emissivity in the IR, and σ is the Stefan-Boltzmann constant. The relationship between A and p_v is $A \cong q \times p_v$ where q is the phase integral $0.290 + 0.684G$ [58]. G is the slope parameter following from the standard H_v , G magnitude system [60]. The thermal flux an observer would detect is then numerically calculated for a given solar phase angle from

$$F_{\lambda} = \frac{\varepsilon D^2}{\Delta^2} \frac{hc^2}{\lambda^5} \int_0^{\pi/2} \int_{-\pi/2}^{\pi/2} \left[\exp\left(\frac{hc}{\lambda \kappa T(\theta, \phi)}\right) - 1 \right]^{-1} \cos^2(\phi) \cos(\theta - \theta_{STO}) d\theta d\phi \quad (3.7)$$

$$T(\theta, \phi) = T_{ss} \cos(\theta)^{1/4} (\cos(\phi))^{1/4} \quad (3.8)$$

where D is the object's diameter, Δ is the geocentric distance, h is Planck's constant, c is the speed of light, and κ is Boltzmann's constant. T_{ss} is determined at $\theta = 0$ $\phi = 0$. The NEATM assumes that no emission originates from the night side, with the observable portion of the body expressed as $\theta = [\theta_{sto} - \pi/2, \theta_{sto} - \pi/2]$ with θ_{sto} describing the sun-target-observer angle, or phase angle. The NEATM, which allows η to be a free parameter, tunes the thermal emission to produce the best fit to the spectral data. This parameter allows for the determination of radii for asteroid observations over a range of phase angles [59].

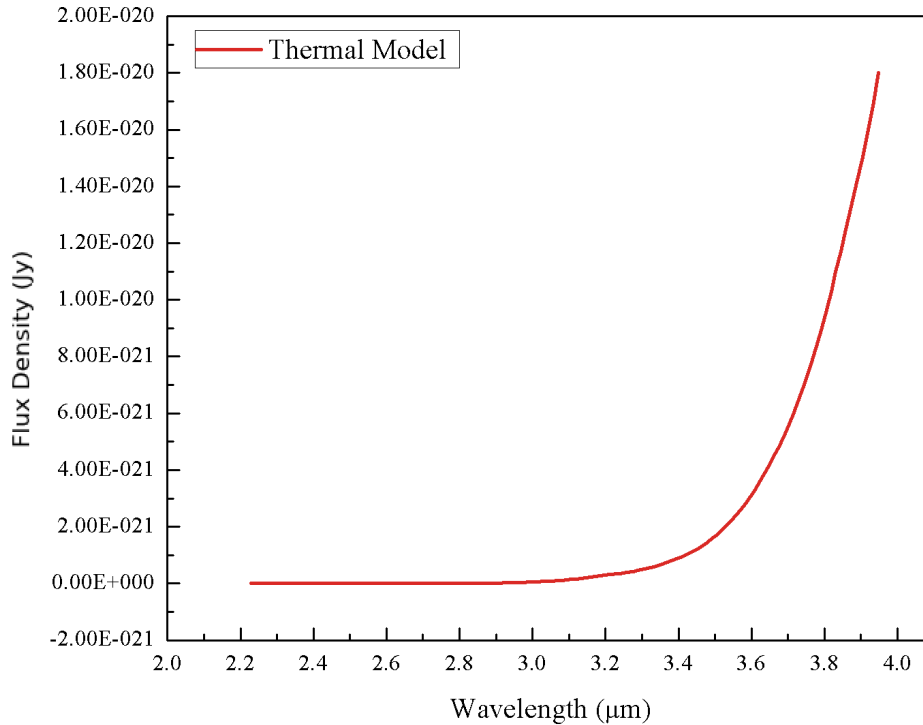


Figure 3.4: **Thermal model for (121) Hermione.** A plot of the estimated thermal radiation emitted from the surface of asteroid (121) Hermione.

We modeled the thermal component in the near-infrared, 2-4 μm region using the NEATM. The NEATM requires several parameters to compute the theoretical thermal flux of an object. We obtained the heliocentric and geocentric distance, and the phase angle or the sun-target-observer angle, θ_{sto} , for each asteroid during the time of our IRTF observations from the Jet Propulsion Laboratory online ephemeris generator (ssd.jpl.nasa.gov). Additionally the NEATM requires the user to provide an albedo guess, or the parameter H_v in order to estimate the asteroid's diameter. The

albedo can be estimated from a measure of the reflected light, though we did not obtain photometry of any of the asteroids at visible wavelengths. Instead we obtained an estimate of the albedo from the NEATM model we generated from the mid-infrared Spitzer spectra. This model also provides estimates of the radius and the beaming parameter η . We were able to acquire the albedo, radius, and η in this way for all asteroids except (790) Pretoria, which was not observed by Spitzer. In the case of (790) Pretoria we assumed the default value of 0.15 for the slope parameter (G) [60], and an H_v magnitude from the JPL Small Database Browser (ssd.jpl.nasa.gov) in lieu of a visible albedo and diameter value. We assumed that the spectral emissivity was constant, and we used a value of 0.9.

Given the user-supplied parameters, we used the NEATM to compute the thermal flux, for this case in the 2-4 μm region, of all six objects. We then estimated the reflected light component of each object using the following equation from Emery et al. [38].

$$Rref_{\lambda} = \frac{F_{sun\lambda}}{r_{AU}^2} \frac{R^2 p_{\lambda} \phi}{\Delta^2} \quad (3.9)$$

where $F_{sun\lambda}$ is the wavelength dependent flux of the Sun at 1 AU, p_{λ} is the geometric albedo at a given λ , ϕ is the phase correction factor [60], r is the heliocentric distance in AU, and Δ is the object-observer distance in AU. This is essentially a model of the reflected solar flux scaled to the albedo of the asteroid at a given θ_{sto} , Δ , and radius. We then divided the thermal model by the reflected light model to achieve the thermal contribution in each the 2-4 μm spectra. An example

of a calculated reflectance model for (121) Hermione is shown in Figure 3.3, and the thermal model in Figure 3.4. To remove this thermal contribution from our reflection spectra, we simply subtracted this component from each 2-4 μm spectra. An example of the thermal contribution in an asteroid spectrum is shown in Figure 3.5.

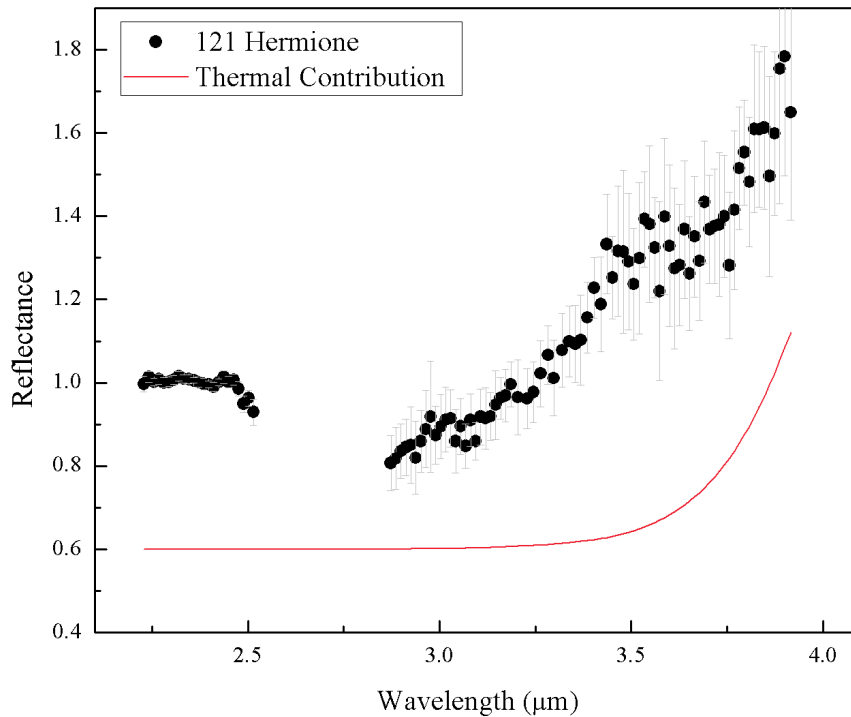


Figure 3.5: **Asteroid (121) Hermione and thermal contribution.** A plot of asteroid (121) Hermione reflectance spectra contaminated with thermal emission (black circles). The red line shows a model of this thermal contribution that we subtracted from our spectra. This figure illustrates how the thermal contribution is typically not significant shortward of about 3.5 μm .

3.3.4 Band Characterization

In order to characterize the 3- μm features for the asteroids, we followed a procedure similar to that in Takir and Emery [5]. We first estimated the spectral continua by extrapolating the slope in the K-band region (1.95-2.5 μm) using publicly available IRTF 0.8 to 2.5 μm near-infrared spectra of each asteroid. The band depth at a given wavelength, D_λ , is the depth of the feature relative to the continuum at that same wavelength:

$$D_\lambda = \frac{R_c - R_\lambda}{R_c} \quad (3.10)$$

where R_c is the value of the solar continuum at a given wavelength, and R_λ is the asteroid's reflectance at the same wavelength as R_c . The errors associated with the band depth calculation

$$\delta D_\lambda = D_\lambda * \sqrt{\left(\frac{\delta R_\lambda}{R_\lambda}\right)^2 + \left(\frac{\delta R_c}{R_c}\right)^2} \quad (3.11)$$

where δR_λ and δR_c are the uncertainties in the flux at each wavelength, which we calculated during the data reduction process.

Using a criterion of a 2σ detection, an asteroid exhibited a 3- μm feature at a given wavelength if $D_\lambda > 2\sigma D_\lambda$. Since this study focuses on the 3- μm feature, we chose to measure D_λ and σD_λ at 3.0 μm . Furthermore, we did not base our calculations on a single point, rather we used an average

of 5 points centered at $3.0 \mu\text{m}$. For our criteria, an asteroid demonstrated a $3\text{-}\mu\text{m}$ feature if $D_{\lambda 3.0} > 2\sigma D_{\lambda 3.0}$.

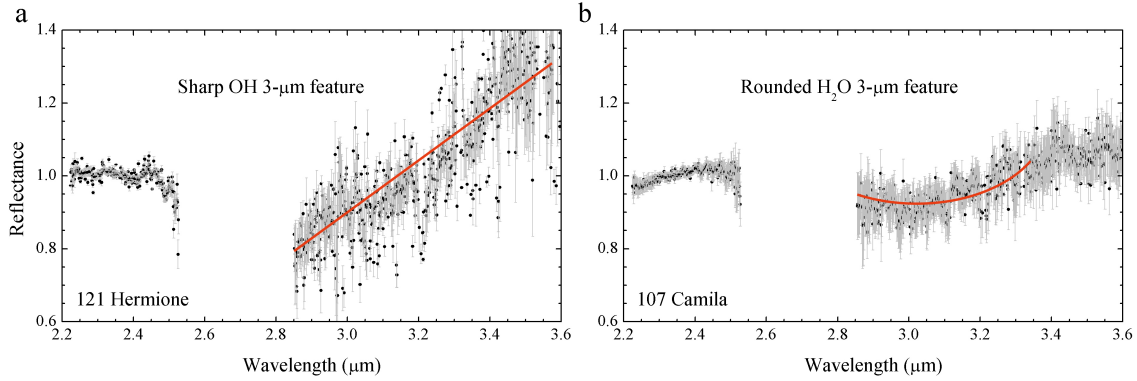


Figure 3.6: **Example of “Sharp” and “Rounded” $3\mu\text{m}$ Features.** An example of the “sharp” and “rounded” variations of the $3\text{-}\mu\text{m}$ feature. Panel (a) provides an example of the sharp $3\text{-}\mu\text{m}$ absorption produced by the fundamental stretch vibration of hydroxyl, and is diagnostic of H_2O incorporated into a mineral lattice or at interlayer sites. Panel (b) is a rounded variation of the $3\text{-}\mu\text{m}$ absorption caused by the symmetric stretch of the H_2O molecule in water ice.

If an asteroid presented a $3\text{-}\mu\text{m}$ feature we characterized the shape of the absorption by dividing out the continuum, then fitting a trend line to the asteroid’s spectrum across the $2.85\text{-}3.25 \mu\text{m}$ region. We implemented a chi-square test to assess whether the best fit was a linear regression, or a second-order polynomial. This process not only provided us with insight into the shape of the spectral feature, but the band center of the absorption minimum. Figure 3.6 shows an example of the two possible shapes observed for the asteroids in our sample. To confirm the results of our band shape analysis, we determined the reflectance at $2.90 \mu\text{m}$ and $3.05 \mu\text{m}$. By calculating the ratio of

$R_{2.90}/R_{3.05}$, we were able to further differentiate between asteroids with sharp and rounded 3- μm features. For example, the spectrum of an asteroid with a sharp feature would be best fit with linear regression and have a $R_{2.90}/R_{3.05} < 1$. Conversely, a rounded feature would be best described by a second-order polynomial, with $R_{2.90}/R_{3.05} > 1$.

3.4 Results

Using spectroscopy in the near-infrared 2-4 μm region, we have observed a small sample of primitive asteroids in the Themis family and Cybele group. All these objects (24) Themis, (65) Cybele, (90) Antiope, (107) Camilla, (121) Hermione, and (790) Pretoria show evidence of either a sharp or rounded 3- μm feature. Using the methods of Takir and Emery (2012) we have quantitatively analyzed the band shape, center and depth of these absorptions, and qualitatively inspected the results. The asteroids in our sample show apparent diversity in the shape, center and band depth of their 3- μm features. Our spectra are presented in Figure 3.7. The results of our band depth analysis are summarized in Table 3.2.

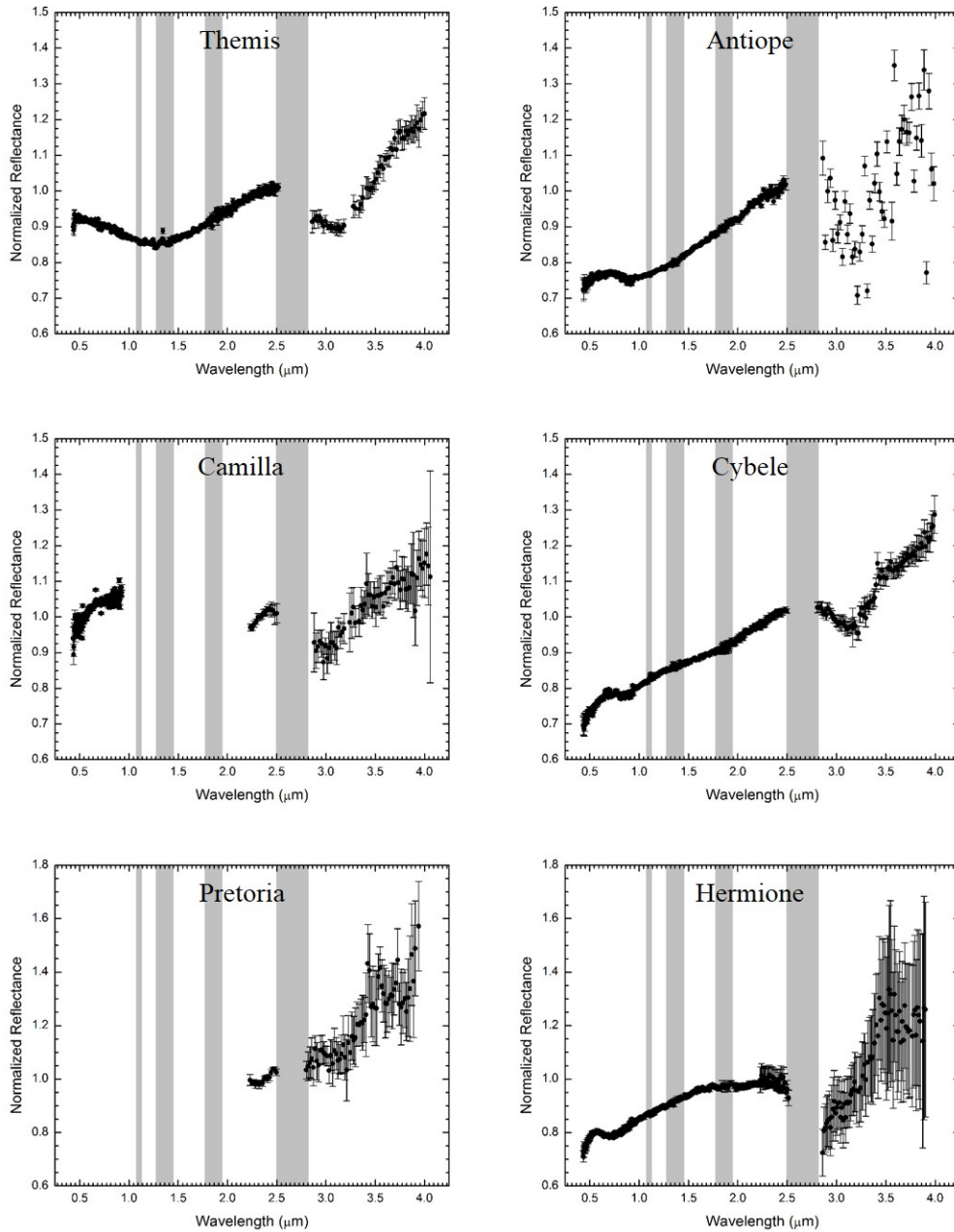


Figure 3.7: **2-4 μm reflectance spectra of primitive asteroids in the Themis family and Cybele group.** Shown are: (24) Themis, (65) Cybele, (90) Antiope, (107) Camilla and (121) Hermione, and (790) Pretoria. This small sample of primitive asteroids show diversity in the shape and depth of their $3 \mu\text{m}$ features. The grey boxes are regions of atmospheric absorptions.

Table 3.2: Band Depth Results and Presence of Organic Materials

<i>Asteroid</i>	<i>Band Depth</i> <i>(This Work)</i>	<i>Band Depth</i> <i>(Literature)</i>	<i>3-μm Absorption</i>	<i>Organics?</i>
(24) Themis	$20\pm 3\%$	$18\pm 3\%$	Rounded	Yes
(65) Cybele	$14\pm 4\%$	–	Rounded	Yes
(90) Antiope	$24\pm 10\%$	–	Rounded	Not Resolved
(107) Camilla	$14\pm 4\%$	$14\pm 7\%$	Rounded	Not Resolved
(121) Hermione	$21\pm 8\%$	$24\pm 8\%$	Sharp	Not Resolved
(790) Pretoria	$6\pm 8\%$	$11\pm 6\%$	Rounded	Not Resolved

Results of our band depth analysis compared to values in the literature [5]. Additionally we determined the type of 3- μ m feature: rounded or sharp. We also visually inspected our spectra for the presence of organic material in the 3.2-3.5- μ m region.

3.4.1 (24) Themis

The spectrum of the largest asteroid in the Themis dynamical family, (24) Themis, shows evidence of a rounded, bowl-shaped 3- μ m absorption feature [1] [2], and our band depth analysis confirms the rounded 3- μ m absorption. We find a band depth of $20\pm 3\%$. Themis also exhibits features in the 3.2-3.6 μ m region that we has previously been attributed to aromatic and aliphatic hydrocarbons.

3.4.2 (65) Cybele

The spectrum of the largest member of the Cybele group, (65) Cybele, has a rounded 3- μm feature [3], and our band depth analysis confirms the rounded 3- μm absorption with band depth of $14\pm 4\%$. Cybele also exhibits weaker bands due to aromatic and aliphatic organic molecules in the 3.2-3.6 μm region.

3.4.3 (90) Antiope

We observed the second largest asteroid in the Themis family, (90) Antiope, on two independent occasions. We find an absorption in the 3- μm region clearly present in our 2008 spectrum and likely in our 2006 spectrum [17]. We chose to focus on our 2008 observation for the band-depth analysis as it had better S/N than our 2006 observation. However the S/N of this 2008 spectrum was still not sufficient for us to detect organic molecules in the 3.2-3.5- μm region.

Our band analysis on this asteroid's spectra was particularly challenging due to the low S/N. We have found that $R_{2.90}/R_{3.05} > 1$ and the best fit to this asteroid features is rounded. We calculated a band depth of $24\pm 10\%$.

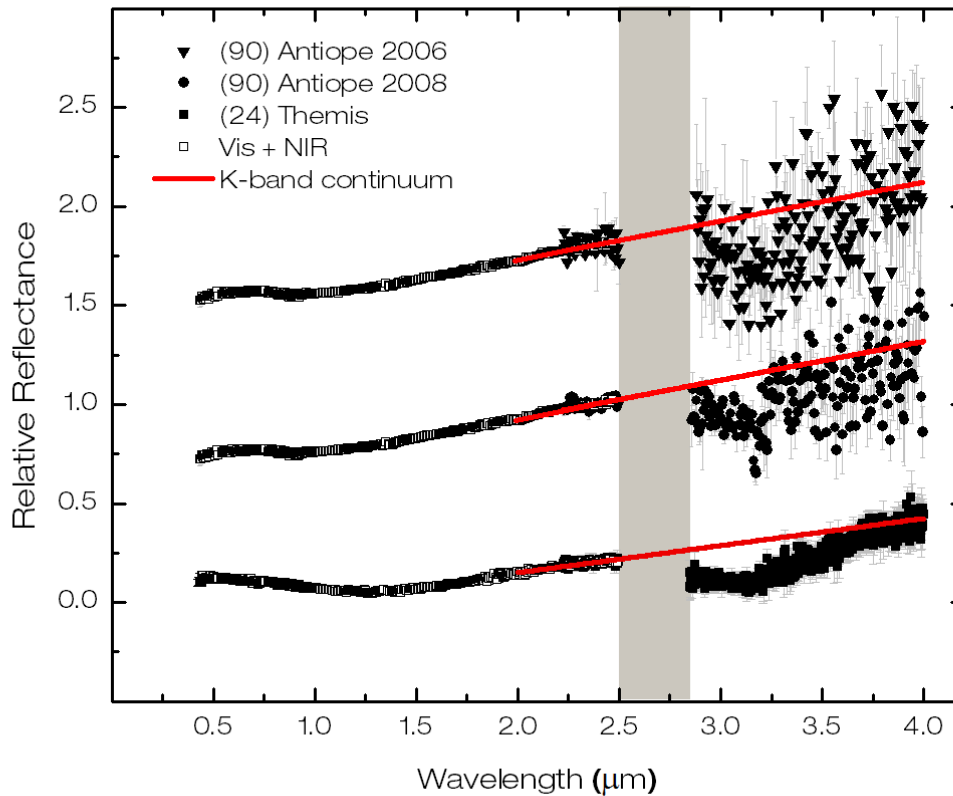


Figure 3.8: **2-4 μm reflectance spectra of (24) Themis and (90) Antiope.** The 2-4 μm reflectance spectra of asteroids (24) Themis [1], and (90) Antiope, obtained with the IRTF, and rebinned to a resolution $R=167$. The K-band continuum was extrapolated from the visible and NIR spectrum near 1.95-2.5 μm . The 0.8-2.5- μm spectra are from the MIT-UH-IRTf survey (<http://smass.mit.edu/minus.html>). The grey box is a region of atmospheric absorption.

Figure 3.8 shows our two independent spectra of Themis family asteroid (90) Antiope with an estimate of the continuum for each observation. Our spectrum of asteroid (24) Themis, pub-

lished in Campins et al. (2010), is shown for comparison. We estimated the spectral continua by extrapolating the slope of the data in the K-band region (1.95-2.5 μm) using IRTF 0.8-2.5 μm near-infrared spectra of Antiope and Themis that are part of the MIT-UH-IRTF Joint Campaign for NEO Reconnaissance (<http://smass.mit.edu/minus.html>). Our 2006 and 2008 2-4- μm spectra exhibit an absorption below the continuum from approximately 2.9-3.2 μm that is consistent with the absorption ascribed to water ice in the spectrum of asteroid (24) Themis [1] [2].

We also compared our Antiope spectra with the same spectral model presented in Rivkin and Emery (2010) to describe the 3.1 μm feature of (24) Themis. This spectral “ice” model consists of a mixture of ice-coated amorphous carbon and pyroxene grains. Figure 3.9 shows our 2006 and 2008 spectra compared with Themis and the Themis ice model. We have divided the asteroid spectra by their continua to remove any slopes, and we normalized the ice models at 3.1 μm for each dataset. Our 2006 spectrum has the lowest S/N and does not appear to necessarily match the width, shape and depth of the ice model, especially in the 2.9-3.0 μm region. Therefore, it is inconclusive if the Themis ice model is appropriate to describe this particular dataset. Our 2008 spectrum has improved S/N, and these data follow the shape of the ice model in the 2.9-3.1 μm region more closely. Comparing with Themis, neither Antiope spectra are entirely consistent with the ice model in the full 2.9-3.2 μm region. This may be due to the S/N of our data and/or the ice model, which was generated for (24) Themis, is not entirely sufficient for the absorption we detect in the spectra of (90) Antiope.

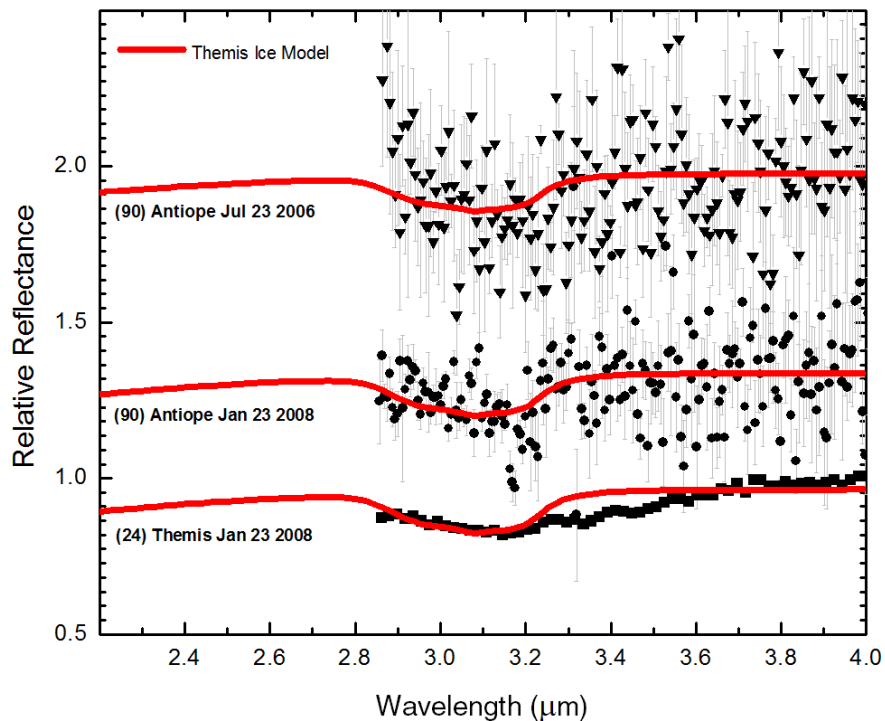


Figure 3.9: **Ice model comparison to Themis and Antiope.** Our two independent (90) Antiope spectra compared with asteroid (24) Themis [1], and an ice model [2]. We rebinned our spectra to a resolution $R=167$. All asteroid spectra have been divided by a continuum we extrapolated from the slope of their spectrum in the K-band region ($1.95\text{-}2.5\ \mu\text{m}$). We have normalized the ice model to the $3.1\ \mu\text{m}$ region of each spectra.

3.4.4 (107) Camilla

Asteroid (107) Camilla presents a rounded 3- μm feature. We calculated the band depth of this absorption to be approximately $14\pm 4\%$, which is identical to the band depth of $14\pm 7.3\%$ determined by Takir and Emery (2012) for this same object [5]. Because the band depth calculations are dependent on our estimates of the continuum extrapolated from the 1.95-2.5 μm region, and these data were not publicly available, we adopted the continuum slopes for Camilla determined by Takir and Emery (2012) [5]. The S/N of the 2-4 μm spectrum of Camilla is not sufficient to detect the weaker bands in the 3.2-3.6 μm region that we have attributed to organic molecules in the spectra of (24) Themis and (65) Cybele.

3.4.5 (121) Hermione

Asteroid (121) Hermione, belonging to the Cybele dynamical group, shows a sharp 3- μm feature. This absorption linearly rises from a minimum shortward of 2.9 μm and is the result of OH-dominated minerals. We calculated a band depth of $21\pm 8\%$ that is similar within the errors to the band depth of 24 ± 7.7 described in Takir and Emery (2012) for this same object. The low S/N of these data limit our detection of organic molecules in the 3.2-3.6 μm region.

3.4.6 (790) Pretoria

Our band analysis indicates (790) Pretoria, a member of the Cybele group, exhibits a rounded 3- μm absorption. We determined a band depth of $6\pm 8\%$. Within the error this value is similar to $11.3\pm 5.6\%$ calculated by Takir and Emery (2012) [5].

3.5 Discussion

Both members of the Themis family we investigated in the 2-4 μm region show a rounded 3.1- μm feature. Spectral features showing hydration in the Themis family are not surprising considering that roughly 50% of its members show signs of aqueous alteration in their visible spectra [61], and two so-called Main-Belt comets (MBCs) 133P/Elst-Pizzaro and 176P/LINEAR belong to this family [13] [62].

Only three Themis-family asteroids have been investigated thus far in the 2-4 μm region: (24) Themis [1] [2], (90) Antiope [17], and (104) Klymene [5]. Models by Castillo-Rogez and Schmidt (2010) predict that many other Themis-family asteroids should contain water ice. Their models suggest that Antiope, its binary companion, and other large Themis family objects may be comprised of a large fraction of the parent body's ice shell. Their models also suggest that the ice on these asteroids may not be completely pure, possibly contaminated with organics, brines, other hydrated minerals, and oxides. Our spectra suggest that asteroid (90) Antiope has a feature possibly

due to H₂O ice, and due to the low S/N of our spectra we were unable to search for organics in the 3.2-3.4 μm region.

The 2-4 μm spectra of our sample of four Cybele group asteroids: (65) Cybele, (107) Camilla, (121) Hermione, and (790) Pretoria exhibit diversity in the shape of their 3- μm features. Asteroid (121) Hermione shows a sharp feature, while asteroid (107) Camilla, (65) Cybele, and (790) Pretoria have a rounded feature that strongly resembles (24) Themis and (107) Camilla.

CHAPTER 4

MINERALOGY AND COMPOSITION OF ASTEROIDS IN THE MID-INFRARED

Visible and near-infrared (VNIR) spectroscopy in the (0.4-2.5 μm) region is crucial for our studies of the surface mineralogy of asteroid classes with prominent spectral features in this range [29][63][64][65][66][67][68][69]. Although there are several asteroid classes, and many subclasses, that remain featureless in the VNIR [70][71]. For these asteroid taxonomic types, most notably the C-, and D-classes, mid-infrared spectra of these objects can provide us with new insight into the composition of these bodies [38][72][39].

This study utilizes existing mid-infrared observations of several primitive main-belt asteroids belonging to the Themis family and Cybele group, the same objects we investigated in the near-infrared 2-4 μm region. Additionally we averaged a large set of mid-infrared spectra belonging to C-, D-, and S-type asteroids. We compare the shape, and strength of the prominent mid-infrared features of these asteroids with both their visible and near-infrared spectral features. This study combines visible, near-, and mid-infrared observations, allowing us to test the robustness of as-

teroid taxonomy and to understand the larger picture of asteroid composition spanning multiple wavelengths.

4.1 Introduction

In the mid-infrared $\sim 5\text{-}38\ \mu\text{m}$ region there are several important indicators of mineralogy including the Si-O stretch and bend fundamentals located between $\sim 8.2\text{-}12.5\ \mu\text{m}$ and $\sim 14\text{-}25\ \mu\text{m}$, respectively. The Si-O stretch is the strongest vibrational mode of silicates caused by the asymmetric displacement of the oxygen in the Si-O bonds [36]. Combined with the Si-O bend, these fundamental molecular vibrations give rise to the $10\text{-}\mu\text{m}$ and $20\text{-}\mu\text{m}$ emission plateaus that are an important marker of asteroid composition. The spectral contrast of the silicate emission features is also diagnostic of an asteroid's surface structure (under-dense or compact) as well as grain size. For example, Trojan asteroids are relatively featureless in the visible and near-infrared, yet these objects have compositionally-detailed, high-contrast $10\text{-}\mu\text{m}$ and $20\text{-}\mu\text{m}$ emission features in the mid-infrared. This lack of information in reflectance spectra and presence in thermal emission spectra may be due to grain sizes less than $2\ \mu\text{m}$, first suggested by Emery et al. (2006) [38] and later refined by Vernazza et al. (2012) [39].

A study by Hargrove et al. (2012) found a possible relationship between the hydration state of an asteroid with its emission in the mid-infrared [4]. They found that asteroids with hydroxyl

or water ice features in the near-infrared had 0-5% 10- μ m emissions in the mid-infrared. The authors attribute this low emission strength to aqueous processes that shaped the surface textures of these objects. This study furthers the work of Hargrove et al. (2012) [4] by using a larger data set, and incorporating the mineralogical interpretations at visible wavelengths implied by asteroid taxonomy.

Table 4.1: Observational Details of Asteroids Observed with The Spitzer Space Telescope

<i>Asteroid</i>	<i>Classification</i>	<i>Program ID</i>	<i>Date (UT)</i>	<i>r (AU)</i>	Δ (AU)	ϕ (deg)	<i>Mode</i>
(24) Themis	B	91	2005-Jun-08	3.54	3.37	16.64	Map
(383) Janina	B	50672	2008-Nov-28	2.93	2.40	19.15	Stare
(704) Interamnia	B	91	2005-Mar-23	3.38	3.12	17.14	Map
(3200) Phaethon	B	91	2005-Jan-14	1.14	0.50	61.74	Stare
(45) Eugenia	C	40164	2007-Oct-30	2.93	2.62	20.24	Map
(90) Antiope	C	88	2004-Jul-12	3.17	3.04	18.76	Map
(379) Huenna	C	91	2004-Oct-24	3.17	3.01	18.78	Map
(253) Mathilde	Cb	88	2004-Jun-26	3.12	3.05	18.92	Stare
(515) Athalia	Cb	50672	2009-Jan-08	2.66	2.01	19.38	Stare
(121) Hermione	Ch	40164	2007-Sep-30	3.36	2.92	17.01	Map
(130) Elektra	Ch	88	2005-Apr-22	3.50	2.91	14.59	Map
(284) Amalia	Ch	1419	2005-Mar-17	2.11	1.70	28.06	Stare
(1086) Nata	Ch	50672	2009-Jan-24	3.03	2.98	19.32	Stare
(2428) Kamenyar	Ch	50672	2009-Apr-02	3.40	3.11	16.94	Stare
(267) Tirza	D	91	2005-Nov-17	3.02	2.97	19.55	Map
(624) Hektor	D	88	2004-Mar-02	5.19	5.24	10.96	Map
(911) Agamemnon	D	88	2004-Aug-08	5.60	5.27	10.25	Stare
(944) Hidalgo	D	91	2005-Feb-10	1.96	1.70	30.74	Map
	D	30241	2005-Jul-24	4.82	4.83	12.15	Map
(07) Iris	S	91	2005-Mar-22	2.91	2.72	20.16	Map
(433) Eros	S	88	2004-Sep-30	1.31	0.95	50.58	Map
(951) Gaspra	S	88	2006-Feb-03	1.97	1.26	26.15	Map
(1685) Toro	S	88	2004-Jul-14	1.15	0.38	61.03	Map
(1866) Sisyphus	S	91	2006-Apr-19	1.65	1.36	37.51	Map

Columns indicate Bus taxonomic classification, Spitzer Program ID, UT date of observation, heliocentric distance r in AU, observer-target-distance Δ in AU, phase angle θ_{STO} in degrees, and the Spitzer observation mode are given.

4.2 Observations

The Spitzer Heritage Archive allows public access to over five hundred spectral and photometric observations in the 3-180 μm range. Despite this large database, only about three hundred and fifty observations were made with Spitzer's Infrared Spectrograph (IRS), and yet fewer (approximately one hundred and thirty) were made in the 5-14 μm region, which is the focus of our studies of the 10 μm emission for various asteroid types. Of these remaining observations about half have the appropriate signal to noise for our analysis. A large majority of these roughly sixty asteroids have already been classified using Tholen, Bus and Bus-DeMeo taxonomies. Though in this study we specifically focus on the Bus taxonomy [7]. The objects we observed and the observation details are described in Table 4.1.

4.3 Data Reduction

The science data obtained with the Spitzer Space Telescope are received by the Spitzer Science Center, where these data were processed with a fully automated reduction pipeline. This pipeline performed a number of important functions, for example, subtracting dark current, flagging bad pixels and cosmic ray hits on the array, and stray light and flat field correction. The outputs from this pipeline reduction were termed Basic Calibrated Data (BCD). These BCD files, although preliminarily processed by the Spitzer pipeline, still contain a background emission dominated by

the zodiacal cloud, and lesser contributions from the interstellar medium. This background not only introduces excess brightness, but also spectral structure that may interfere with any features present in the spectra of an object. Additionally, the FUNC and BMASK calibration files also require post processing. Therefore we developed several routines in the python programming language to further reduce the Spitzer BCD, FUNC, and BMASK files. We also implement routines to extract the asteroid spectra, align the disjointed spectral orders, and fit a thermal model to the asteroid's spectral energy density.

4.3.1 Post Processing

We first downloaded all available Spitzer IRS data for our near-infrared targets, after performing a moving object search for asteroids (24) Themis, (65) Cybele, (90) Antiope, (107) Camilla, and (121) Hermione from the Spitzer Heritage Archive . Asteroid (790) Pretoria was not observed by Spitzer. Our routine searched the FITS headers of the BCD files to check if the observing mode was IRS stare or IRS map. In most cases, Spitzer observed the asteroids in mapping mode, which allowed the observer to configure a grid of positions centered around a target object, with spectra obtained at each position. To define this grid in mapping mode, the telescope slewed in a direction perpendicular to the long axis of the slit (rows) for a number of steps before moving parallel to the slit (columns) for a number of steps, where the observer defined the number of steps for each

case. For example, in the case of (121) Hermione the number of steps perpendicular to the slit was 3, and the steps parallel was 2, creating a grid of 2 columns and 3 rows. The observer could also specify any combination of IRS modes (e.g. SL, SH, LH, LL) and the slit size, each with a different number of map cycles and exposure times (ramp duration). For example, the observer of (121) Hermione selected the SL2, SL1, SH and LH modes. In the case of the SL modes Spitzer created two maps, one centered on the SL 1st order, and one centered on the SL 2nd order. Since Spitzer obtained spectra in both orders simultaneously, as there is physically only one SL slit, there were several extraneous spectra taken with one order offset from the target object. We later used these offset spectra to create sky frames for background subtraction.

Our routine averaged all on-source frames for each order. Then created a sky background for each order using off-source frames. These were combined and subtracted from the average on-source frames. The FUNC files were combined by adding these frames in quadrature. The BMASK files were combined using the bitwise-or method.

Our routine produced three products: 1) BCD.FITS files, 2) FUNC.FITS files and 3) BMASK.FITS files. The routine created several of these files depending on the mode (e.g. SL, SH, LH, LL) that was observed by Spitzer. For example, (121) Hermione had a total of 6 files for the SL modes: 4 BCD files (SL1_Position1.BCD, SL1_Position2.BCD, SL2_Position1.BCD and SL2_Position2.BCD) and 2 calibration files (FUNC.FITS, and BMASK.FITS). For the SH and LH modes our routine produced only 4 files each. The next step in our data reduction procedure re-

quired the Spitzer IRS Custom Extraction Software (SPICE) that we used to calibrate and extract spectra from the BCD files output by our code.

4.3.2 SPICE

Spice is a JAVA-based software that allows a user to interactively extract Spitzer IRS spectra. We chose this method because IRS spectra are not rectilinear on the array, thus spectral extraction requires careful tracing of the particular shape of each order, which SPICE takes into consideration.

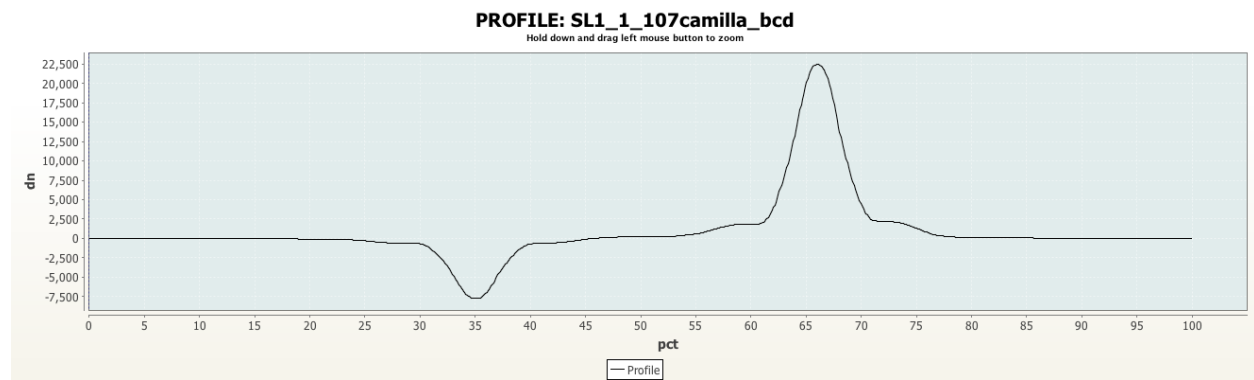


Figure 4.1: **(107) Camilla profile.** This example is for the SL 1 module, nod position 1. Spice determines the profile by averaging orders at a given spatial position.

Upon opening Spice we initiated an “extraction flow”, more specifically the point source with regular extraction flow. This flow is a visual and interactive collection of modules that allow a user to process the data in a specific order. The first module is Initialize Parameters and Files, where the user inputs the image file, mask file, and uncertainty file, as well as defines the output directory

where SPICE will place the reduced data. In this module the user must also specify the Calibration file. In all cases, we chose the default calibration file that SPICE determined using information from the FITS header of each asteroid's BCD file.

The second module, Profile, takes as input the two-dimensional BCD image the user defined in the previous module. It calculates the average of the cross-dispersed orders at a given spatial position (Figure 4.1). By default SPICE uses all of the available orders for a particular channel (High Resolution or Low Resolution) to compute the mean, and we selected this option. SPICE determines the location of the orders using the wavsamp.tbl calibration file.

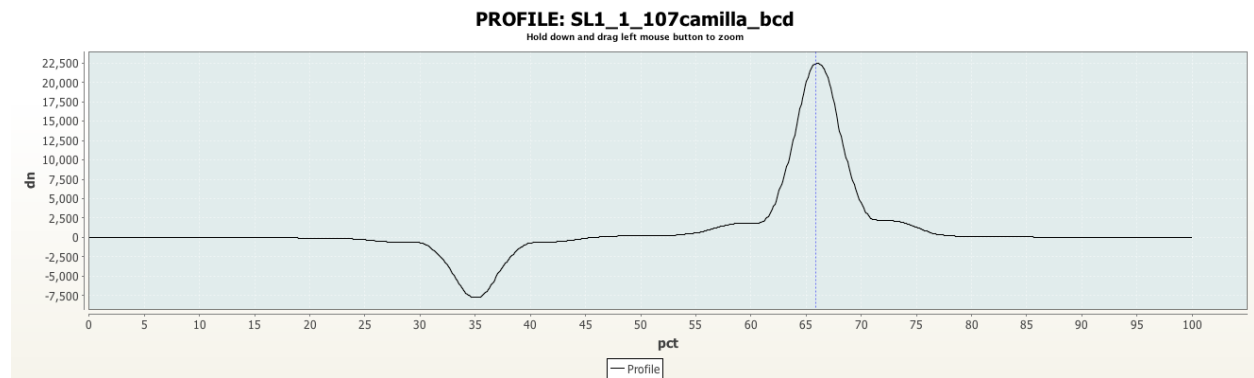


Figure 4.2: **(107) Camilla ridge**. This is an example of the maximum in the peak profile, or the ridge, that Spice determined was located at 66% along the length of the slit.

Ridge, the third module, uses the output from Profile to locate the peak in the spatial profile, and define the spectral trace of the point source SPICE is to extract. The location of the profile peak represents a percentage across the detector beginning from $x=0$. The user can chose the default

position determined by RIDGE or can manually enter a value. We always selected the default position, though after we visually inspected each RIDGE plot, for example in Figure 4.2.

The fourth module, EXTRACT, performs spectral extraction by summing the flux along the spectral trace determined by RIDGE within a window size specific to the IRS module as shown in Figure 4.3. For example, in the low resolution SL modes this window size is related to whether the object is a point or extended source, and for the high resolution SH, and LH modes EXTRACT uses the full slit width. We selected “point source - default” as this best represents the asteroids observed by SPITZER in this study. We also chose “regular extract” as the “optimal extract” option is best for point sources observed in IRS staring mode, not map mode. We left the default option for SPICE to set the fatal bit pattern, and to replace NaNs, in which case it interpolated over any NaN pixels in the data. The final result of the extraction process was a one-dimensional spectrum in units of electrons per second.

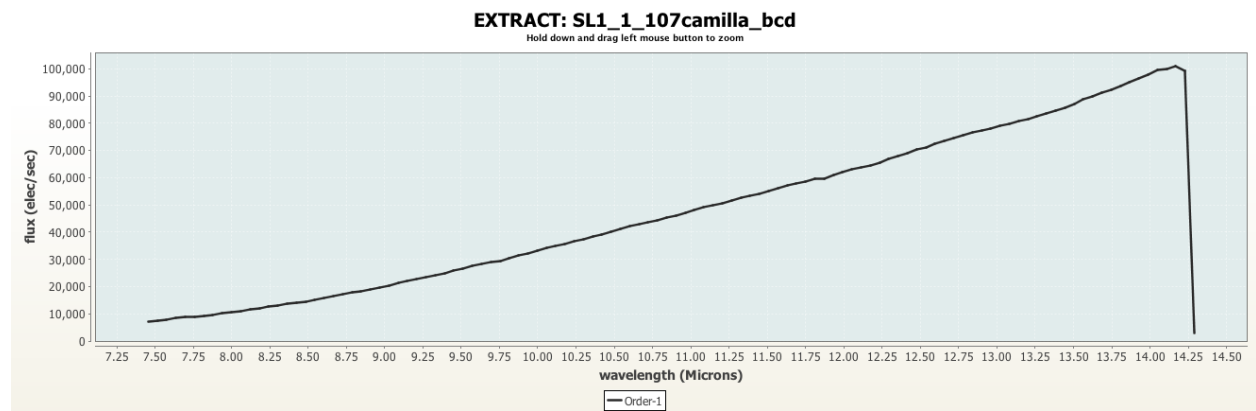


Figure 4.3: **Extracted Spectrum of (107) Camilla.** The extracted spectra is from the SL1 nod position 1, covering the $\sim 7\text{-}14\ \mu\text{m}$ range.

The last module, Point Source Tune, is specifically for point source objects, and, thus, applicable in this study of asteroids. Point Source Tune makes adjustments to the shape of each order (different for SL, LL, SH, and LH), and corrects by a scaling constant that is in units of electrons/s/Jy to convert the final spectrum into units of Jy shown in Figure 4.4.

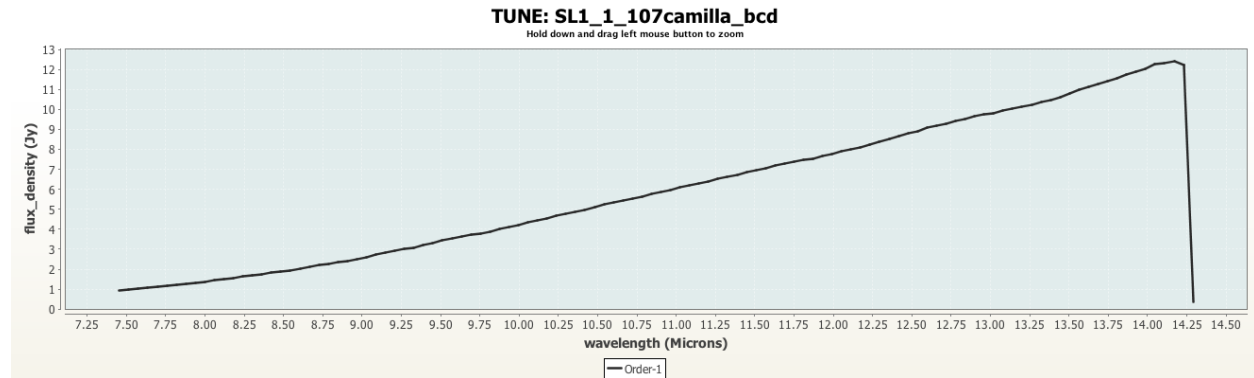


Figure 4.4: **(107) Camilla point source tune.** The point source procedure tuned the SL1 nod position 1 spectrum of (107) Camilla to the $\sim 7\text{-}14\ \mu\text{m}$ range. The spectrum has been corrected by a scaling constant to convert the final flux into unit of Jansky. Note the difference in the y-axis values compared to Figure 4.3.

4.3.3 Spitzer Align Modes Code

Of the several files output by the SPICE software, the *bcd.spect.tbl files contain the final reduced spectra of each asteroid for each mode (e.g SL, LL, SH, LH) observed by Spitzer. As previously mentioned, each observation consisted of two nod positions. For instance spectra taken in the

first order of the SL module consisted of spectra obtained by Spitzer at position 1 (33% along the axis of the slit) and position 2 (66% along the axis of the slit). Since both spectra are in the 7-14 μm region they can be combined, but only after we had used SPICE to extract these spectra independently. Also, the spectra of each mode was disjointed. To address these issues, we wrote a secondary routine in python, COMBMODES, to further process these data.

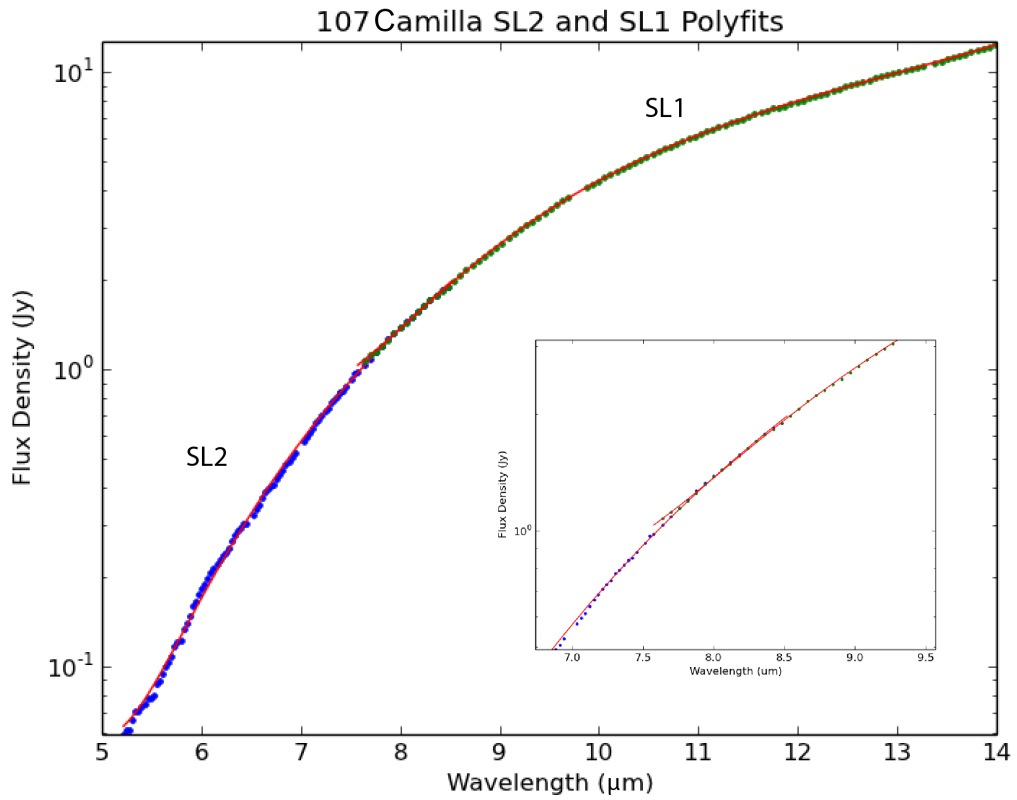


Figure 4.5: **(107) Camilla SL2 spectrum scaled to SL1.** Our routine, COMBMODES, determined the scale amount that best aligned the SL2 mode to the SL1 mode.

For each asteroid COMBMODES read the spectra extracted by SPICE into individual 2-D numpy arrays. Each array consisted of five columns: order, wavelength (μm), flux density (Jy), error, and bit flag. COMBMODES used the bit flag column to remove any fatal bit flags from each mode's order and nod position separately. Spitzer's post production process deemed certain bits fatal, and thus unusable for several reasons. COMBMODES compared the bit flag value from the asteroid data with bit flag values known to be fatal (e.g. 6,7,10,14) by computing the bitwise AND of the value from the bit flag column and $2^{(6,7,10,14)}$. If there was a value match then COMBMODES removed the entire row of the 5-column data array. Since COMBMODES later combines each nod position, if a value was deemed fatal in one of the nod positions (33% or 66%) it was removed from both. COMBMODES then computed a simple average of both nod positions for each mode, and calculated the errors on the flux as the standard deviation of the wavelength dependent flux points that went into the average.

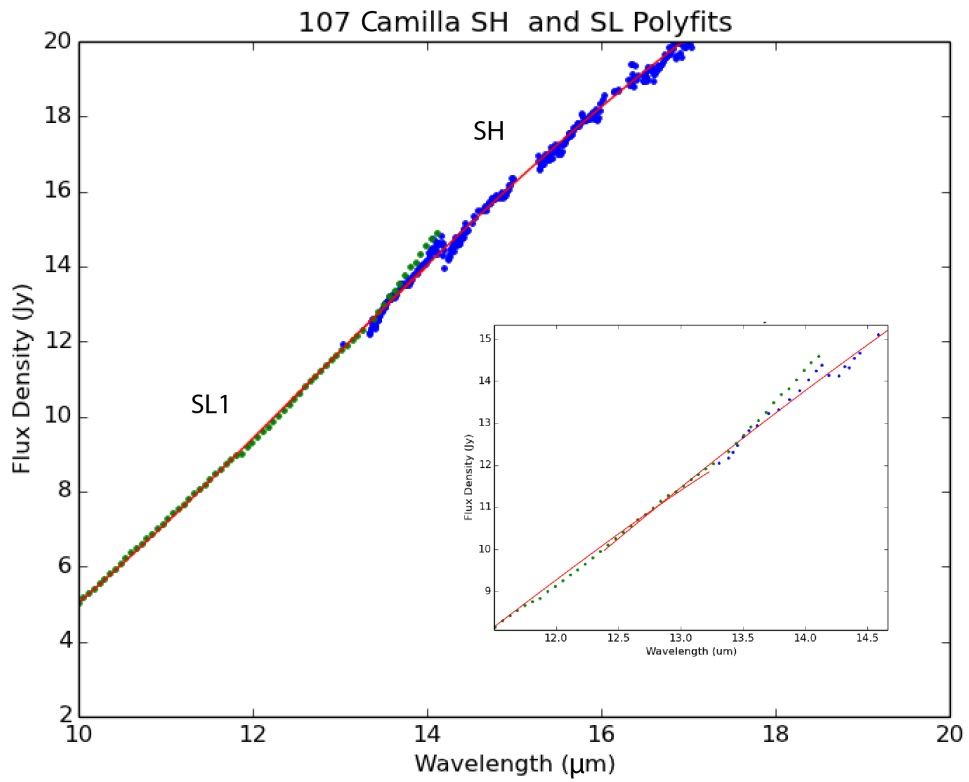


Figure 4.6: **(107) Camilla SH spectrum scaled to SL1.** Our routine, COMBMODES, determined the scale amount that best aligned the SH mode to the SL mode.

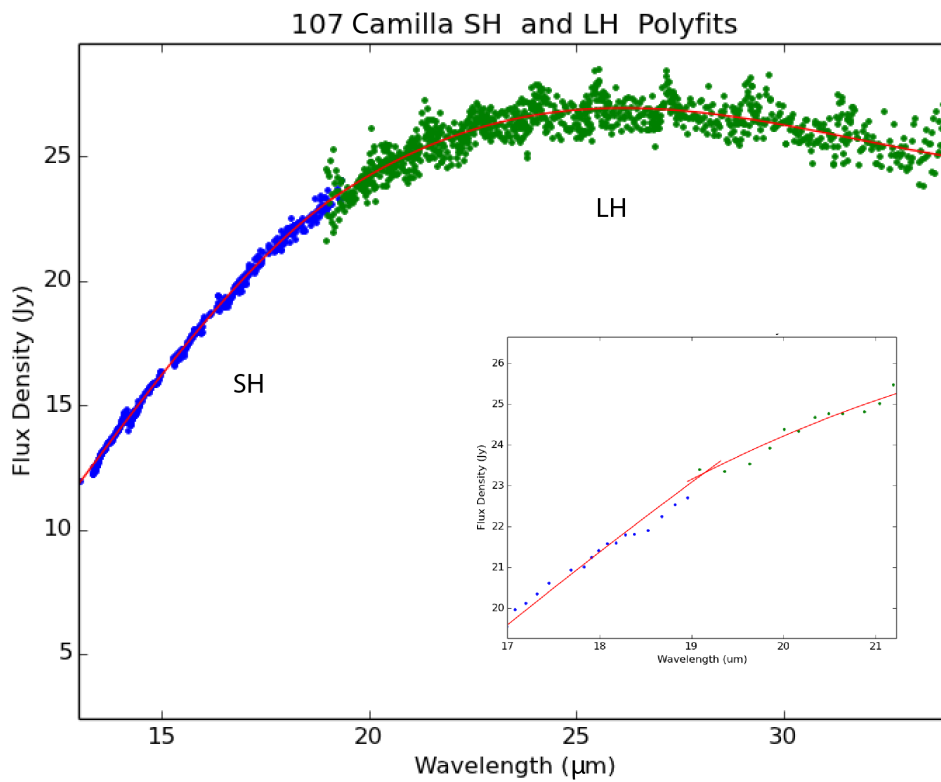


Figure 4.7: **(107) Camilla LH spectrum scaled to SH.** Our routine, COMBMODES, determined the scale amount that best aligned the LH mode to the SH mode.

Next COMBMODES addressed the misaligned spectral modes. The routine fit low-order polynomials to each mode that extended beyond the data as shown in Figures 4.5-4.7. The degree of the polynomial and the amount these polynomials extended is a user defined, adjustable parameter. COMBMODES would move one of the polynomials up or down in the y-axis (Flux Density) in increments of 0.01 to match the reference polynomial, checking how well the extended polynomials overlapped by assessing a chi-square value. The smallest chi-square value corresponded to the amount the polynomial, and thus data, needed to be scaled in order to align with another mode. COMBMODES essentially scaled all modes to SL1. For example, SL2 was scaled to match SL1. Then either LL or SH was scaled to match SL. And lastly LH was scaled to SH, which was itself scaled to SL1. All of the scale values determined by this routine were consistent with IRS pipeline's absolute calibration uncertainty of approximately 10%. For each asteroid COMBMODES output a text file with 3 columns: wavelength in microns, the aligned spectral modes in units of Jy, and the errors on the flux. These resulting spectral energy densities, an example of which is shown in Figure 4.8, we used for the final analysis involving a thermal model.

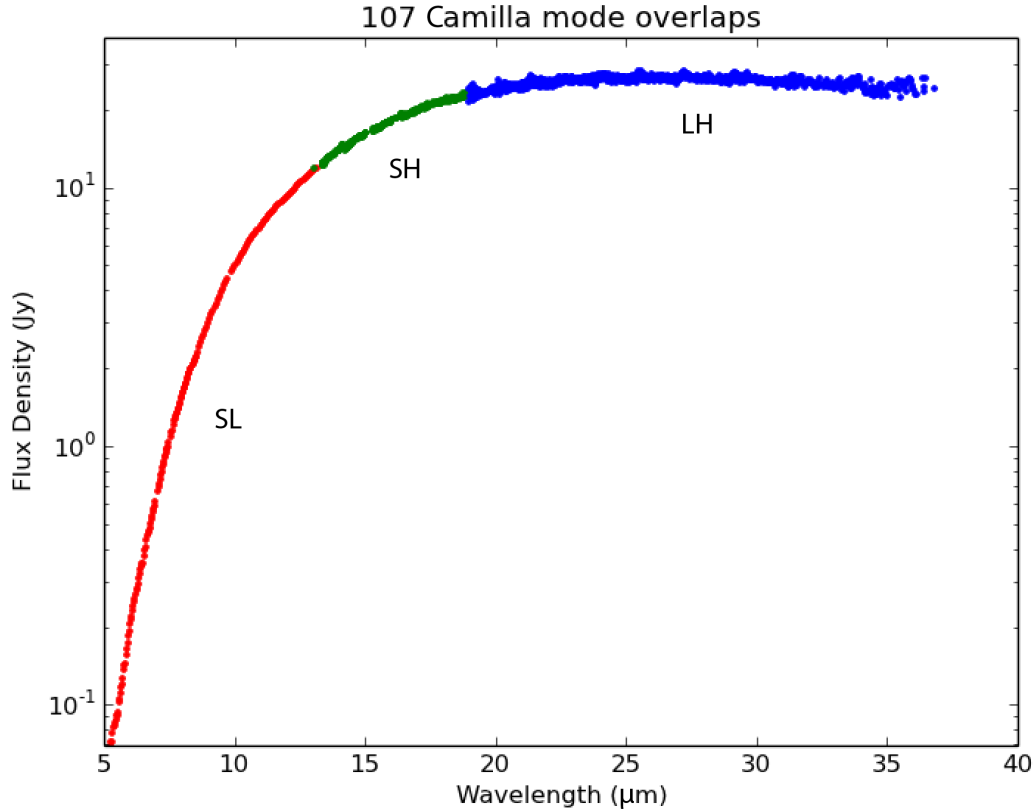


Figure 4.8: **Aligned 5-35- μm spectrum of (107) Camilla.** This aligned spectrum is the result of scaling the SL2, SH, and LH modes.

4.3.4 Thermal Modeling

We fit the NEATM to the mid-infrared 5-14 μm spectra of our asteroid sample. Inputs to the NEATM include the heliocentric distance (r), object-target distance (Δ), and the sun-target-observer angle (θ_{sto}) at the time of the Spitzer observations that we calculated by using the online ephemeris generator provided by NASA’s Jet Propulsion Laboratory. We obtained the slope parameter (G) [60] and the visible magnitude (H_v) from the WISE Main Belt Asteroid Pass 1 Table

if these were available. If WISE did not observe an asteroid we obtained G and H_v from IRAS measurements that are cataloged in the JPL Small-Body Database Browser.

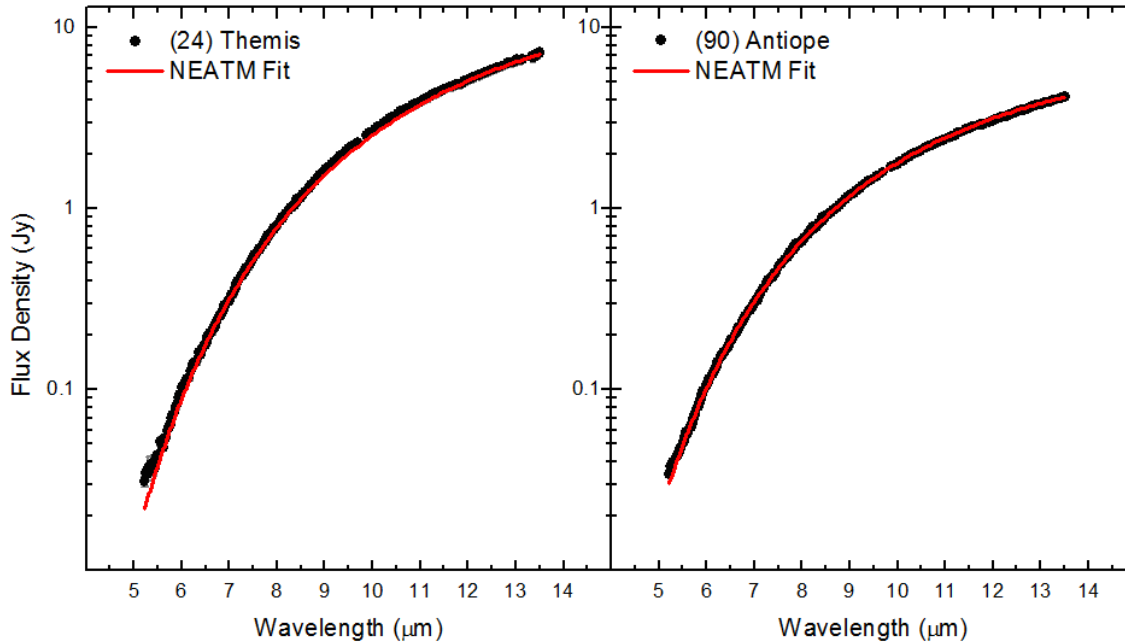


Figure 4.9: **(24) Themis and (90) Antiope NEATM fits.** The Near-Earth Asteroid Thermal Model (red line) fit to the 5-14 μm spectral energy density of asteroid (24) Themis and (90) Antiope.

In addition to the offsets between spectral modes there are contributions from reflected light and an artifact that affects our SL1 spectra. From approximately 5-7 μm there can be contribution from both reflected light and thermal emission. We did not characterize this reflected light component, instead we forced the NEATM to ignore this region. There is also an artifact known as the 14- μm teardrop that may produces excess flux in the 13.5 and 15.0 μm region. The teardrop is misleading as it can closely resemble an emission feature. Since there is no way to characterize the behavior

of the teardrop, there is no way to correct for it. Therefore, we have also forced the NEATM to ignore this region longward of $13.5 \mu\text{m}$ from the SL1 order.

In the mid-infrared, asteroid surface spectroscopy is dominated by thermal emission, which is affected by the composition and grain structure (size, porosity) of the surface. To reveal small scale absorption features or emission features in the thermal emission spectra of our asteroid sample, we divided the Spitzer mid-IR spectrum of each asteroid by their thermal continuum model computed by the NEATM. Any deviations from the theoretical model are potentially spectral features, useful for comparison with other asteroids as well as interpreting surface minerals and composition. The spectral contrast of the silicate emission features is also diagnostic of an asteroid's surface structure (under-dense or compact) as well as grain size. As mentioned, Trojan asteroids are relatively featureless in the visible and near-infrared, yet these objects have compositionally-detailed, high-contrast $10\text{-}\mu\text{m}$ and $20\text{-}\mu\text{m}$ emission features in the mid-infrared. This lack of information in reflectance spectra and presence in thermal emission spectra may be due to grain sizes less than $2 \mu\text{m}$, first suggested by Emery et al. (2006) and later refined by Vernazza et al. (2012) [38][39].

4.4 Results

4.4.1 Themis Family and Cybele Group Asteroids

Our thermal modeling of the mid-infrared spectra of the Cybele Group and Themis Family asteroids provided us with estimates of their diameters. These diameters are described in Table 4.2.

Table 4.2: Position of Aliphatic CH Stretch Features

<i>Asteroid</i>	<i>Diameter</i>	<i>Type</i>	<i>Density</i>	<i>Mass</i>	<i>Emission Contrast</i>
(624) Hektor	220±14	D	2.4	1.3x10 ¹⁹	10-15%
(65) Cybele	291±10	Xc	4.9	6.3x10 ¹⁹	5%
(24) Themis	214±12	B	2.4	1.2x10 ¹⁹	3-4%
(107) Camilla	257±12	X	1.8	1.6x10 ¹⁹	3-4%
(121) Hermione	165±10	Ch	1.4	3.3x10 ¹⁸	0%
(90) Antiope	111±10	Ch	1.4	1.0x10 ¹⁸	0%

Listed are the diameters, in km, for the Themis and Cybele asteroids were obtained from our thermal modeling of their mid-infrared spectra. The diameter for Trojan (624) Hektor was determined from Emery et al. (2006) [38], and listed for comparison. The density of (624) Hektor was obtained from lacerda et al. (2007) [73], and all others were adapted from Carry (2012) that determined the bulk densitites of asteroid types [74]. Density values are in units of g cm⁻³, and masses are in kg. Masses were roughly estimated using the diameters and densities, assuming a spherical shape.

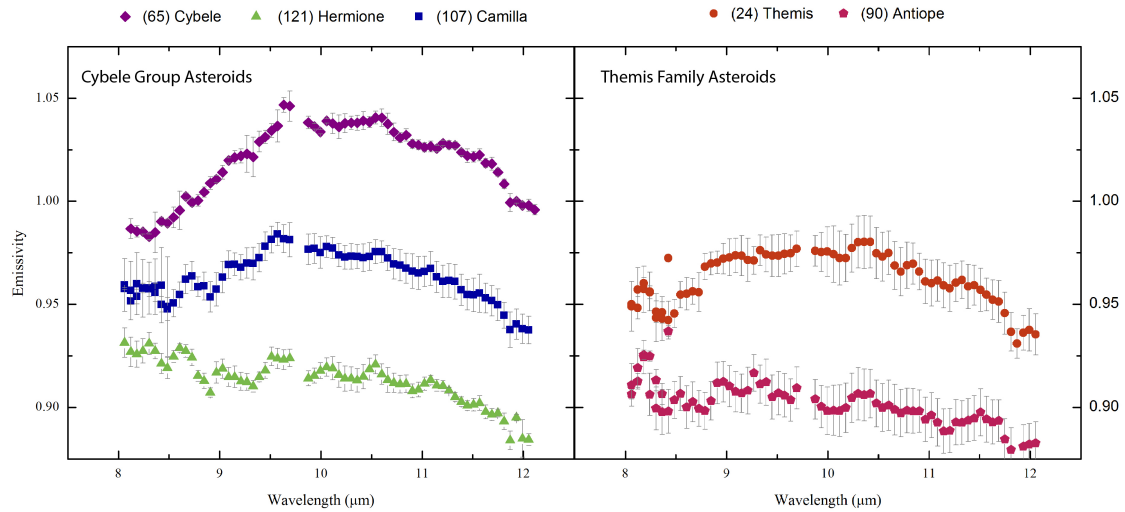


Figure 4.10: **8-10 μm emission spectra of hydrated asteroids from the Cybele group, and Themis family.** The Cybele group objects are shown in the left panel, and the Themis family objects are shown on the right. We obtained these emission spectra by dividing the Spectral Energy Density of each asteroid by their respective thermal models. Spectra are offset for clarity.

After modeling the mid-infrared spectra of our sample asteroids, we determined their emissivity spectra. The emission spectra of three Cybele group asteroids and two Themis family asteroids are shown in Figure 4.10. The emission of Themis has an overall broad bump between 8.3 and 12.0 μm that rises from 8.3 μm to 9.0 μm , flattens from this point until 10.3 μm , and then steadily declines to 12.0 μm . (90) Antiope's emission spectrum does not show a broad overall bump as in the case of Themis; rather, it peaks around 9.3 μm and steadily declines to approximately 11.8 μm . The emissivity spectrum of (65) Cybele exhibits an emission plateau starting from about 8.3 μm to approximately 12.1 μm , rising from 8.3 μm to 9.5 μm , flattens from this point to 10.5 μm , then

declining from 10.5 to 12.1 μm . (107) Camilla has a broad feature from about 9 μm to just shy of 12 μm , rising from 9 μm to about 9.5 μm , where it flattens to 10.5 μm , then steadily declines from this point to shortward of 12 μm . (121) Hermione's emission spectrum does not show a broad overall bump in the 8-12 μm region; rather, it peaks around 9.5 μm and steadily declines to approximately 11.8 μm . Asteroid (65) Cybele has the strongest emission at roughly 5%. (107) Camilla has an emission strength of roughly 3-4%, while (121) Hermione has no silicate emission in the 8-10 μm region. (24) Themis has an emission strength similar to that of (107) Camilla, while (90) Antiope has a 0% emission more akin to (121) Hermione. We attribute the low (0-5%) emission of these asteroids to a different surface structure than Trojan asteroids, which exhibit emissions in the 10-15% range. Unlike Trojans, these Cybele group and Themis family asteroids have near-infrared 3- μm features indicating water-ice or hydroxyl, which may contribute to their lower emissions. The spectral contrast of the asteroid emissions in the 8-12 μm region are detailed in Table 4.2.

4.4.2 Asteroid C-, D-, and S-types

Figure 4.11 show the results of the average emission of Bus C-, D-, and S-types. The D-type asteroids show the most pronounced emission with a contrast of approximately 10%. They have a broad, plateau-like emission feature similar to that seen in several comets (Emery et al. 2006). The

C-types show an emission similar to the D-types but with approximately 1/5 the contrast. They exhibit a more rounded, muted emission shape compared to the D-types, and comets. The S-type asteroids show an emission that peaks at approximately 8.5 μm and slopes downward to roughly 13 μm .

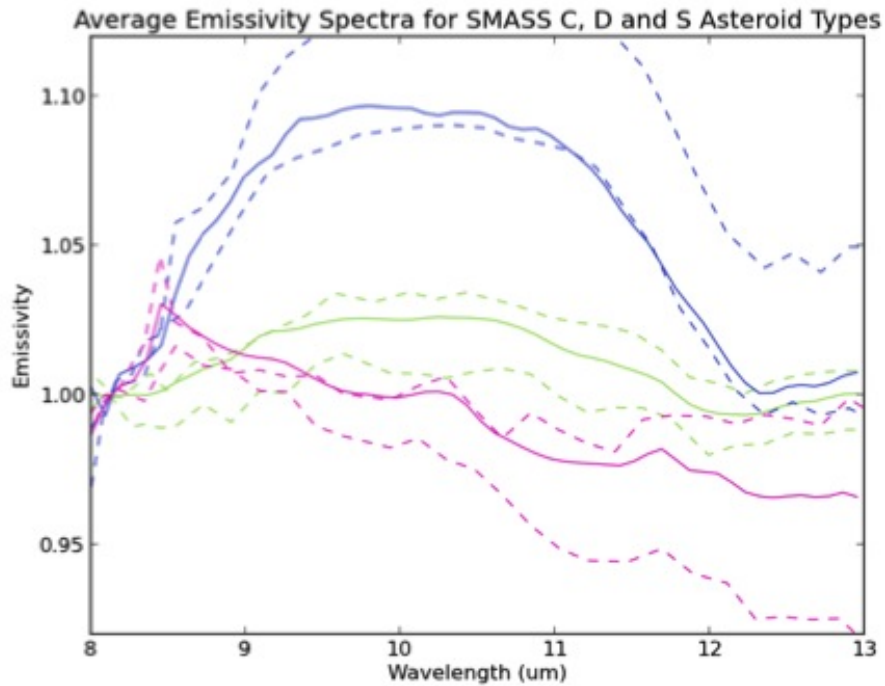


Figure 4.11: **8-13 μm spectra of C-, D-, and S-types.** The emission spectra of C-, D-, and S-type asteroids cluster into 3 statistically distinct groups based on their 8-13 μm spectra. The solid lines are the average of the 8-13 μm spectra. The dashed lines represent the highest and lowest emissivity spectra for each asteroid type at 10 μm . All spectra are normalized at 8.0 μm .

4.5 Discussion

4.5.1 Themis Family and Cybele Group Asteroids

The mid-infrared spectra of our sample of primitive asteroids, all of which exhibit a near-infrared feature indicating water-ice or hydroxyl, show low-strength 8-12 μm emission spectra in the 0-5% range. Work by Licandro et al. (2012) found a similar result when studying the emission of 8 Themis-family asteroids [75]. They attribute the lower amplitude of the 10 μm emission to larger dust particles, and/or a slightly denser surface structure. Our results are in agreement Licandro et al. (2012), but are add odds with the strong (10-15%) 10- μm silicate emission bump in the spectra of Trojan asteroids [38] that were found by Vernazza et al. (2012) to be the result of small grains on the first millimeter of the regolith that produces a high porosity surface structure [39]. It is possible that the Themis family and Cybele group asteroids in our study have larger surface grains, and thus lower surface porosity than the Trojans as a result of aqueous processes that produced their visible and near-infrared hydration features.

We notice differences and similarities in the emission spectra of these two populations (Figure 4.10). For example, asteroids (24) Themis and (107) Camilla have similar emission feature strengths of 3-4%. Asteroids (90) Antiope and (121) Hermione have no detectable emission in the 8-12 μm region. Interestingly both of these objects are part of a binary system. (121) Hermione is a bifurcated, elongated object [76] as is (90) Antiope.

All of the larger mass objects, (624) Hektor, (65) Cybele, (24) Themis (107) Camilla, exhibit an emission feature (Table 4.2). These more massive objects possess a higher gravity, making them able to retain smaller grains, which allows for a higher porosity, fluffier surface. By this notion (65) Cybele, the most massive object, should have the strongest emission. However we find that Trojan (624) Hektor has the highest contrast emission, double that of (65) Cybele. (624) Hektor has a mass more similar to (24) Themis and (107) Camilla, yet exhibits an enhanced $10\ \mu\text{m}$ emission strength. Therefore, we do not attribute the strength of the $10\ \mu\text{m}$ emission to mass alone. We believe that the presence of OH- and H₂O-dominated minerals has a more profound effect on the surface structure of asteroids. This is consistent with the more primitive, less aqueously and thermally altered surfaces of Trojans as indicated by an absence of a $3\ \mu\text{m}$ feature in the spectra of these asteroids [38].

This analysis of the $10\ \mu\text{m}$ silicate emission may be used as a method to indicate or confirm hydration at shorter wavelengths. Based on our analysis of this small sample, asteroids with a flat to somewhat rounded emission in the 8-12 μm region with a strength of 0-5% may show signs of hydration in the near-infrared.

4.5.2 Asteroid C-, D- and S-types

We have discovered that at least 3 of the main SMASS taxonomic groups (Cs, Ds, and Ss) defined by their visible spectra clearly cluster into 3 statistically distinct groups based on their mid-infrared 8-13 μm spectra. Our results are similar to Marchis et al. (2012) that found similarities in the mid-infrared emission spectra of several asteroid types, including X, C, Sq, S and V-types [72].

Our result validates the robustness of visible taxonomy, and the relationship between features at different wavelength regimes. In Table 4.3 we detail how taxonomy, mineralogy, and hydration inferred at shorter wavelengths relates to the shape, strength, and slope of the 8-13 μm emission. For this work we used a larger sample of asteroids than our study of Themis family and Cybele group asteroids. Though our results are identical. We find that the contrast of the 10 μm emission spectra may be an indicator of the amount of thermal and aqueous processing that an asteroid has experienced, especially when considering the C- and D-types. The C-types have several features indicating hydration in the visible and near-infrared, while the D-types have relatively featureless spectra at these wavelengths. The D-types, including some Trojans and main belt asteroids, likely harbor ice below the surface in their interiors. We attribute their strong emission in the mid-infrared to a lack of thermal processing, which would have melted their interior ice or brought it to the surface. It is possible that the aqueous events that produced hydration features detectable at shorter wavelengths in members of the C-complex have altered the surface textures and/or surface

porosities of these bodies, which has dampened the strength of their 10 μm emission spectra to 0-5%. This is consistent with Hargrove et al. (2012; 2015) that found a possible trend with hydration when comparing the 10 μm emission spectra of several primitive asteroids with 3- μm features, all of which exhibited a spectral contrast less than 5% [4] [17].

Of the three asteroid classes in this sample, the D-types likely have the highest surface porosity and/or smallest grain size due to their primitive nature. The S-types likely have the lowest surface porosity and/or largest grain size possibly related to the extreme thermal alterations they experienced. The surfaces of the C-types are intermediary between these two classes, as they have undergone the most aqueous processing.

Table 4.3: Relationship Between Asteroid Taxonomic Type with Spectral Features in the Near-, and Mid-infrared.

<i>SMASS Asteroid Type</i>	<i>Processing</i>	<i>Visible-Near-Infrared</i>	<i>Mid-Infrared</i>
D	Very Little?	Generally featureless	Have most pronounced emission with a strength $\sim 10\%$. Emission spectra have a broad, plateau-like shape similar to that in comets.
C-Complex	Thermal \rightarrow Aqueous	OH-minerals, H ₂ O-minerals, Oxidized Fe in phyllosilicates, Magnetite	Emission similar in shape to the D asteroid spectra, but $\sim 3-4\%$
S	Thermal \rightarrow Igneous	Olivine, Pyroxene, Fe-N metal	Unique emission shape that peaks at $\sim 8.5 \mu\text{m}$ then continues with a negative slope to $\sim 13 \mu\text{m}$

Columns indicate the asteroid SMASS classification, anticipated processing, Visible and Near-Infrared absorption features, and Mid-Infrared emission features.

CHAPTER 5

LABORATORY SIMULATION OF ASTEROID ORGANICS

Organic molecules such as aliphatic hydrocarbons and polycyclic aromatic hydrocarbons (PAHs) are abundant throughout our galaxy, the moons of giant planets, Earth, comets, Interstellar Dust Particles (IDPs), the Diffuse Interstellar Medium (DISM), primitive meteorites, and were recently detected on asteroids [1] [2] [3]. Although we still poorly understand the formation mechanisms and modification of these organics. Several theories for the synthesis mechanisms of organic solids have been proposed by researchers, including these in the hot inner protoplanetary nebula, the cold interstellar medium, the outer solar nebula, the circumstellar environment surrounding highly evolved stars, and in meteorite parent bodies by processes of aqueous alteration [77]. Regardless of the mechanism behind their formation, organic hydrocarbons were likely widely distributed in the solar nebula during the formation epoch of planetary and asteroidal bodies, and were incorporated into these objects.

The experiments we performed at NASA Ames are an effort to reproduce the organics we have detected on asteroids, thus providing us with a more detailed understanding of their molecular composition, formation mechanism, formation environment, evolution, and likelihood of contributing to life on Earth. We compared our laboratory spectra of organics with that we have detected in other

astronomical sources, in particular carbonaceous chondrites, comets and the interstellar medium, in our effort to understand the likely source of organics on primitive asteroids. Our analysis may also shed light on which chondrite type shares the most similarities with asteroids (24) Themis and (65) Cybele, and may place considerable constraints on the proposed formation region of organics and these asteroids. *Did (24) Themis and (65) Cybele accrete their organics in the outer solar system or in the outer main belt where they are located today?* Studies by Kebukawa and Cody (2014) suggest the Insoluble Organic Material (IOM) in carbonaceous chondrites, comets and IDPs (which are cometary and asteroidal in origin) were formed or best preserved in the outer solar system [77]. Therefore, linking the organics in chondrites with that in primitive asteroids could suggest these objects indeed formed in the outer reaches of the solar system. This would support hypotheses such as the the Grand Tack [78] in which asteroids from the outer solar system were scattered inward by the migration of Jupiter. An outer-solar-system origin for asteroid organics would also support the Nice model [79] that describes an influx of objects into the inner solar system from the outer due to gravitational perturbations from Jupiter and Saturn.

5.1 Introduction

Water ice, and aliphatic and aromatic hydrocarbons, have been detected on two asteroids thus far [1] [2] [3]. To simulate the organics on these asteroids we created several laboratory mixtures con-

taining similar components. Although to create astrophysically relevant organics, more complex in structure than our starting organics, we had to subject our ice-organic mixtures to UV irradiation, similar to the conditions like materials would experience in a space environment. This irradiation initiated many chemical reactions, producing new species, and changing the molecular structure of our starting products.

The aliphatic hydrocarbons we chose for this study are saturated hydrocarbons, or alkanes, the simplest of the hydrocarbon species. Alkanes consist of only hydrogen and carbon atoms, all singly bonded with the general formula C_nH_{2n+2} . The aromatic component is comprised of polycyclic aromatic hydrocarbons (PAHs) that similarly contain only carbon and hydrogen, though are bonded in benzene ring-like structures. Aliphatic and aromatic hydrocarbons produce pronounced features that we can easily compare with those detected in several other astronomical sources. For example, the C-H stretch molecular vibration of aliphatic hydrocarbons typically produces 4 features: the $-CH_3$ asymmetric stretch at $3.38 \mu m$, the $-CH_2-$ asymmetric stretch at $3.41 \mu m$, the $-CH_3$ symmetric stretch at $3.48 \mu m$, and the $-CH_2-$ symmetric stretch at $5.0 \mu m$. The identification of the band profiles and strengths of these features is crucial to understanding the nature of carbonaceous material in our laboratory and asteroid infrared spectra. The band centers of the aliphatic C-H stretch features are well documented for many astronomical objects, and interstellar sources. The positions of these bands can be very diagnostic of, for example, aliphatic hydrocarbons that

contain other perturbing chemical groups such as aromatic hydrocarbons that can shift the C-H stretch features from their nominal positions [80].

Widely reported and diagnostic tools in the fields of astrophysics and meteorite analysis are the optical depth ratio (τ_{CH_2}/τ_{CH_3}) and the column density ratio (N_{CH_2}/N_{CH_3}). The τ_{CH_2}/τ_{CH_3} ratio provides a rough estimate of the number of -CH₂- groups compared to -CH₃ groups, and provides a rough estimate of the average aliphatic chain length and/or branching nature of the aliphatic carrier. Branching occurs when -CH₃ groups bond to the -CH₂- groups in aliphatic chains, creating disordered organic structures. The N_{CH_2}/N_{CH_3} ratio is a more robust calculation, measuring the number of C atoms contributing to the aliphatic -CH₂- or -CH₃ groups. It is also indicative of the average aliphatic chain length and/or branching of the aliphatic carrier. For example, a higher N_{CH_2}/N_{CH_3} ratio suggests longer aliphatic chains and/or more cyclic aliphatic structures, and, conversely, a lower ratio would indicate shorter chain lengths and/or higher branching levels [81]. The τ_{CH_2}/τ_{CH_3} and N_{CH_2}/N_{CH_3} ratios for our laboratory ices and our two asteroids will help us to constrain the nature of organics on (24) Themis and (65) Cybele. Furthermore, there is plethora of astronomical objects and interstellar sources for which the organics have been studied in more detail. For example, this ratio has been extensively calculated for primitive meteorites [82], IDPs [83], the DISM [80] [84], and even the sample dust returns from comet Wild 2 [83].

5.2 Laboratory Samples

We created four mixtures containing only three components: water, an aromatic and an alkane. Alkanes are, in the simplest sense, aliphatic hydrocarbons consisting of chains of $\text{-CH}_2\text{-}$ groups terminated on each end of the chain by a -CH_3 group. We varied the alkanes, from propane to decane, to sample a wide range of chain lengths. For the aromatic component we chose naphthalene, the simplest polycyclic aromatic hydrocarbon. Examples of the hydrocarbons we chose for the mixtures are depicted in Figure 5.1. Our first mixture contained water, naphthalene, an aromatic, and propane, a short chain alkane consisting of only one $\text{-CH}_2\text{-}$ group. Our second mixture included water, naphthalene, and 3-methylpentane (3-MP), an alkane with three $\text{-CH}_2\text{-}$ groups, and an extra -CH_3 group bonded to the 3rd or central carbon in the aliphatic chain, making this our only branched organic. Our third mixture was comprised of water, naphthalene, and hexane, an alkane with four $\text{-CH}_2\text{-}$ groups. Lastly our fourth mixture consisting of water, naphthalene, and decane, a long-chain alkane with eight $\text{-CH}_2\text{-}$ groups. Our mixtures and ratios are listed in Table 5.1.

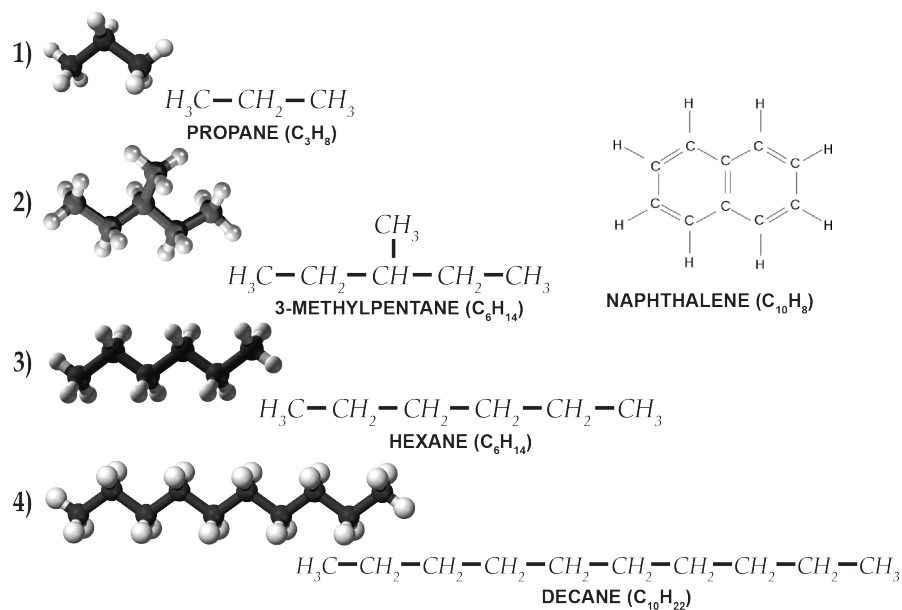


Figure 5.1: **Aliphatic and aromatic hydrocarbons.** We used these four types of alkanes in our simulations of asteroid organics. We chose these particular alkanes to vary the amount of initial $-CH_2-$ groups.

5.3 Laboratory Techniques

The following describes the techniques that we implemented in the laboratory to create astrophysically relevant ices containing various types of organics. We performed this work at the NASA Ames Astrophysics Laboratory in Moffett Field, California.

Table 5.1: Ratio of Water, Aromatics and Alkanes in our Laboratory Samples

<i>Mixture</i>	<i>Description</i>	<i>Ratio</i>	<i>-CH₂- Chain Length</i>
H ₂ O + C ₁₀ H ₈ + C ₃ H ₈	Water + Naphthalene + Propane	15:0.1:2	1
H ₂ O + C ₁₀ H ₈ + C ₆ H ₁₄	Water + Naphthalene + 3-methylpentane	15:0.1:2	3
H ₂ O + C ₁₀ H ₈ + C ₆ H ₁₄	Water + Naphthalene + Hexane	15:0.1:2	4
H ₂ O + C ₁₀ H ₈ + C ₁₀ H ₂₂	Water + Naphthalene + Decane	15:0.1:1	8

We chose an astrophysically relevant ratio of water to the other components, and used this same ratio for each of our mixtures except in the case of decane. Due to the vapor pressure of this material we added less, to avoid it remaining in liquid form.

5.3.1 Fabrication of Gas Bulbs

We prepared all of our gas mixtures in a glass line evacuated by a diffusion pump that allowed us to achieve a background pressure of $\sim 2 \times 10^{-5}$ mTorr. To eliminate contamination from atmospheric gases and cross contaminants, we evacuated the glass line with the diffusion pump, if the pressure was greater than $\sim 5 \times 10^{-3}$ mTorr, and then the diffusion pump when the pressure was below this value. We then turned on a heated tape element that wrapped around the longest dimension of the glass line. By heating the glass line, as the line is being evacuated, any unwanted volatiles with a low vapor pressure are liberated and removed from the system. We attached the glass bulb to the glass line, and opened it up to the vacuum. We also attached any relevant glass fingers containing the alkanes 3-methylpentane, hexane and decane, which are all in liquid form at room temperature. We only exposed the interconnect between the finger and the glass line to the vacuum, while the

finger remained closed. The combination of the heat tape and the diffusion pump typically led to pressures of $\sim 2 \times 10^{-5}$ mTorr in the glass line, interconnects, and bulb after 24 hours. Achieving such low pressures was crucial for exceeding the vapor pressures of the materials that we used in our experiments. For example we were able to incorporate the aromatic naphthalene, normally solid at room temperature, in its gaseous form in all 4 bulbs.

When preparing our first gas mixture, we added 15 mB water, (H₂O), to both the glass line and bulb. We then closed off the bulb. The glass bulb had a long stem that we submerged in liquid nitrogen to freeze out the 15 mB of water to the bottom of the bulb's stem. This procedure allowed us to add other components to the bulb without the water evacuating the bulb. We switched to the roughing pump to remove as much water as possible from the glass line. We allowed the pressure to reach 2×10^{-3} mTorr, and it was not crucial that we achieved pressures lower than this since small amounts of water contamination would not significantly affect our overall mixture as water was the main component of the mixture. The next material we added was propane. We calculated how much propane was needed in the glass line with

$$\textit{Amount needed in Line} = \frac{\textit{Volume of bulb} \times \textit{Amount of desired alkane}}{\textit{Volume of glass line}} \quad (5.1)$$

where the volume of the bulbs were either 2350 ml or 2100 ml, the amount of desired alkanes ranged from 1-2 mB, and the volume of the glass line was 555 ml. Since propane is not stored in a glass finger, we attached a propane tank to the glass line, and pumped out any atmosphere that we

introduced into the system. Once at a pressure of 5×10^{-4} mTorr, we added 7.5 mB of propane to the glass line then opened the bulb. The propane transferred from the glass line to the bulb since the bulb's stem, still submerged in liquid nitrogen, was acting as a cold trap. Once all the propane was frozen out we closed off the bulb, and once again cleared the glass line with the roughing pump to a pressure of $\sim 2 \times 10^{-3}$ mTorr. We then calculated the amount of naphthalene ($C_{10}H_8$) that was needed in the glass line using equation 5.1.

Since the vapor pressure of naphthalene is lower than the other components, we had to add 0.1 mB amount of this material into the glass line four separate times, using the freeze out method in between each addition. We did not clear the glass line with the roughing pump in between each addition of naphthalene since it is a difficult material to add to the bulb in general because 1) it has a relatively low vapor pressure and 2) it is an extremely sticky substance, adhering to any surfaces (e.g. walls of the glass line) along its path to the bulb. Therefore, any contamination of naphthalene from the previous addition was actually beneficial, likely allowing us to achieve an amount closer to our theoretical estimate. We performed an almost identical procedure when creating the other four bulbs, only changing the alkane (3-methylpentane, hexane, decane) that we used since all four bulbs contained similar components of water and naphthalene. The bulbs on average had a final pressure of ~ 17 mB.

We would like to note the problems we experienced with decane. We had to take special care with this aliphatic as its low vapor pressure allowed it to return to liquid form once in the

bulb. This could have caused problems when attaching the bulb to the system as the liquid could flow down into the system and remain there, possibly contaminating future experiments. Also when depositing our bulb contents into the chamber we may not have been depositing as much decane as we expected if some of it was in liquid form, and not uniformly mixed with the other components. Our solution was to add less decane, and apply heat to the bulb after preparation and before deposition to ensure that the decane was in gaseous form.

5.3.2 Experimental Techniques

In order to perform measurements on the contents of each completed bulb, we attached the bulbs to a cryovac system similar to the one depicted in Figure 5.2. This system was outfitted with an infrared spectrometer similar to the one shown in Figure 5.3. We attached our bulb to the system, though it would remain closed as we let the system bake out overnight by applying a heat tape that was wrapped around the longest dimension of the chamber. Similarly to the glass line, the heat tape would help to liberate any volatiles from previous experiments that were sticking to the walls of the chamber. Using this method, after approximately 24 hours we were able to achieve pressures of 2×10^{-7} mTorr at 300 K, room temperature. After cooling the spectrometer with liquid nitrogen, we would take a background spectrum in the 2-16 μm range at 300 K that was useful to ratio any spectra we obtained of our final organic residue at this temperature. We would

then cool the system with a closed-cycle liquid-hydrogen cryocooler in order to obtain backgrounds at other key temperatures, specifically 200 K, 150 K, 100 K, and 15 K. It was important that we acquired backgrounds at these temperatures because of the various structural states of water, each one uniquely contributing to the 3 μm feature. The 200 K background sampled mostly gaseous water and other volatiles. The background at 150 K and 100 K straddle the amorphous ice to crystalline ice transition of water ice. Lastly the background at 15 K, is the temperature at which we deposited our gas mixtures, and obtained a large majority of our spectra.

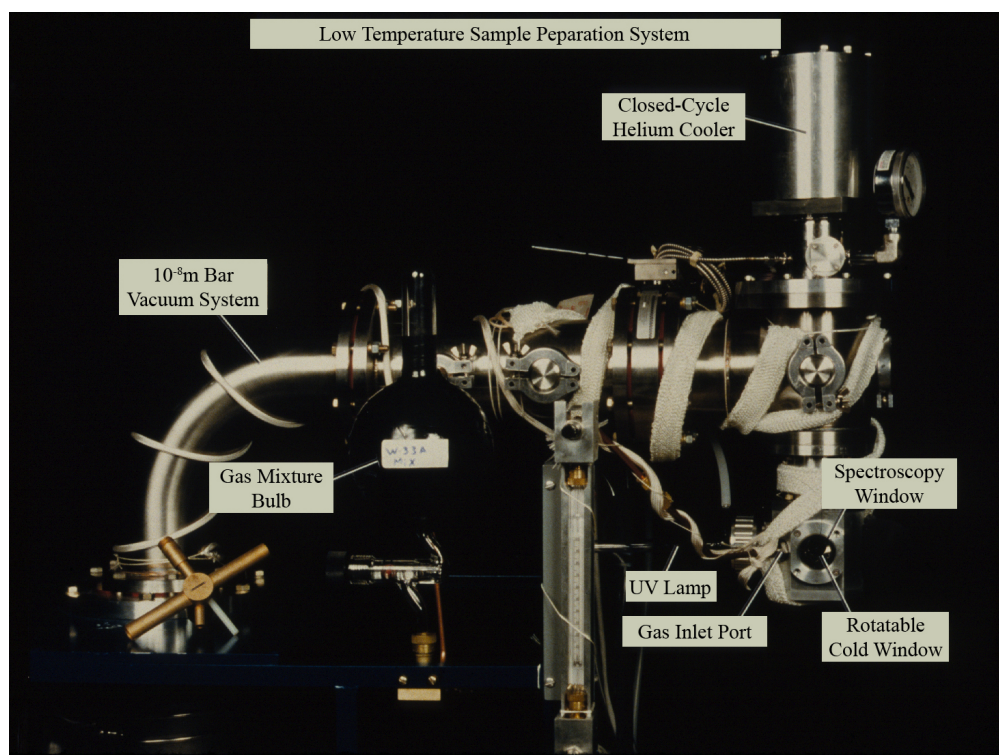


Figure 5.2: **Example cryovac system.** This cryovac system is similar to the one we used for our experiments. The closed-cycle helium cooler allowed us to reach temperatures close to 15K.

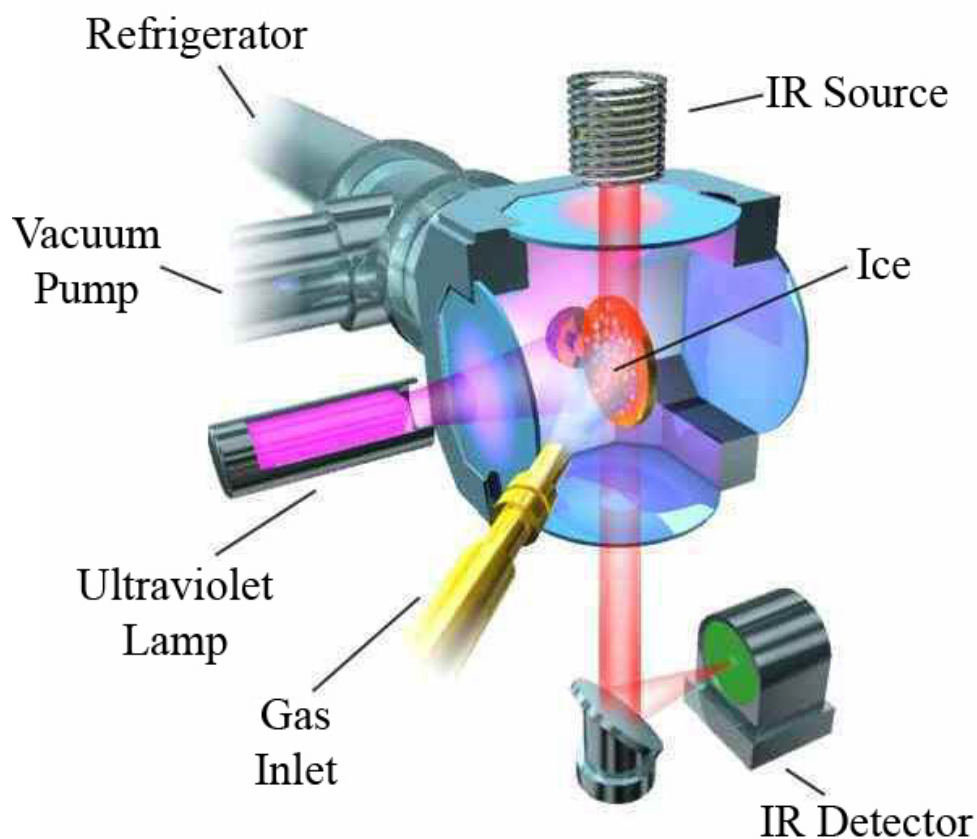


Figure 5.3: **Schematic of system sample head.** Our gas mixtures were deposited onto the system via the gas inlet valve, where it condensed into ice on the window. We situated the window at an angle such that we could perform UV photolysis and deposition simultaneously. Adapted from [8].

Once the system had cooled to roughly 15 K, we would initiate the UV lamp, which has an estimated rate of $\sim 2 \times 10^{15}$ photons $\text{cm}^{-2} \text{s}^{-1}$. We would immediately begin deposition of the bulb contents onto a zinc-solenoid window. The temperature and pressure differential between the bulb and the chamber allowed the gas to flow to the window, where it would condense into an ice as shown in Figure 5.4. We chose a slow flow rate, allowing very thin layers of ice to form slowly

over the length of the experiment. This maximized the number of UV photons that could interact with the ice molecules, producing more photoproducts and more evenly distributed photoproducts than, for example, irradiating just the surface of a thick ice.

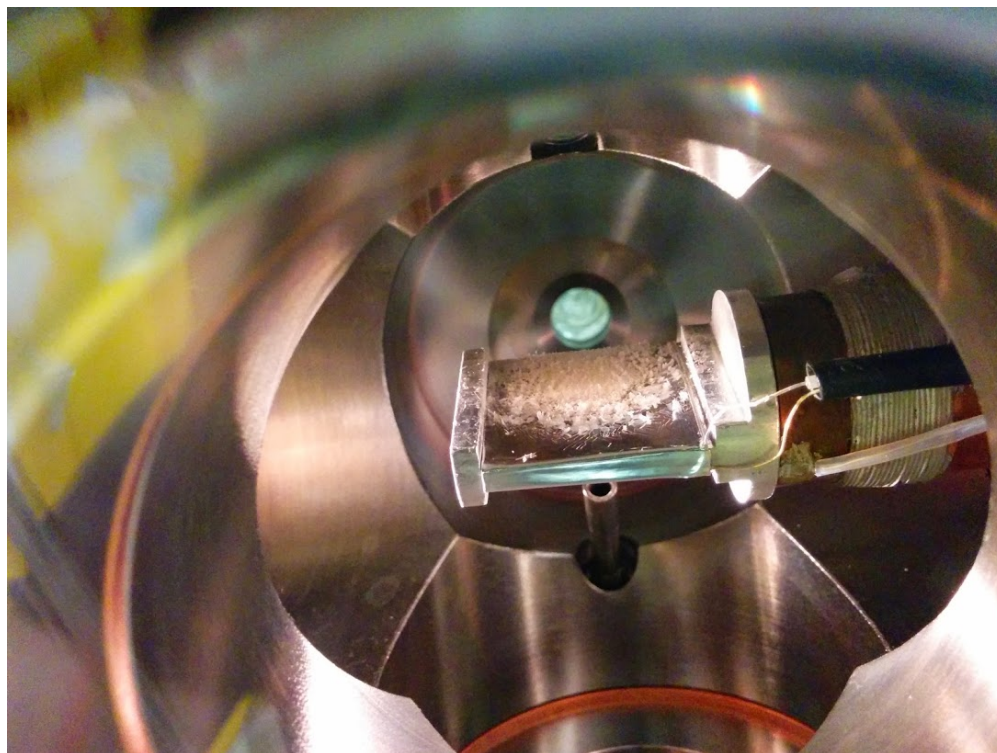


Figure 5.4: **Example of an astrophysical, organic-rich ice created in the laboratory.** These ices formed on a zinc-solenoid window after deposition of the bulb material at temperatures near 15K, and under UHV pressures.

After approximately 20 minutes with this deposition rate, the ice was thick enough that we could obtain a spectrum with good S/N. We would later use this first spectrum to serve as a control, estimating the initial ratios of the C-H stretch features in the organics present before much change was introduced by UV irradiation. We would allow the simultaneous photolysis and deposition to

continue for, on average, 72 hours, taking spectra of the ice throughout this duration. This long irradiation time roughly corresponded to about 216 million years of solar radiation, more than an order of magnitude longer than the lifetime of a typical dense molecular cloud $\sim 10^7$ years. We chose this irradiation time to ensure an excess of chemistry occurred.

After approximately 72 hours we closed off the bulb from the system so that ice was no longer depositing, and turned off the UV lamp. We initiated the warm up phase of the experiment that allowed us to observe how the ice changed with the influence of temperature alone, without any additional UV irradiation or deposition of more material. We warmed the temperature of the chamber and sample head very slowly, typically less than 1K/min to ensure that the ice did not sublime so quickly and violently that the material was liberated off the window. We typically warmed from deposition temperature of about 15 K to 110 K, 110 K to 150 K, and 150 K to 200 K, obtaining spectroscopy between each temperature set. Once at a temperature of 200 K we warmed in increments of 10 K, for example from 200 K - 210 K, 210 K - 220 K, and 220 K - 230 K. At 230 K we warmed in increments of 5 K from 230 K - 235 K, and 235 K - 240 K. We chose to acquire spectra at these smaller temperature ranges as we observed an interesting phenomenon in this 230 K - 240 K region during our experiment containing hexane. Once at 240 K, we warmed from this temperature to 250 K. From 250 K, we warmed directly to 300 K, or room temperature. This was the most critical temperature as the material left behind at this temperature was room-temperature, stable complex organic material.

5.4 Data Analysis

One of the most important tracers of carbonaceous material in the interstellar medium are the absorption bands in the 3.38-3.5 μ m region, arising from -CH₂- and -CH₃ groups in aliphatic hydrocarbons. We analyzed the spectra of our laboratory material and candidate asteroids in this diagnostic region using five spectral characteristics: (i) the band centers of the asymmetric and symmetric -CH₃ and -CH₂- features, (ii) the optical depths (τ) of the asymmetric -CH₃ and -CH₂- features, (iii) the FWHM of the asymmetric -CH₃ and -CH₂- features, (iv) the ratio of the optical depth (τ) of the -CH₂- asymmetric feature to that of the -CH₃ asymmetric feature, and (v) the ratio of the column density of the -CH₂- asymmetric feature to that of the -CH₃ asymmetric feature.

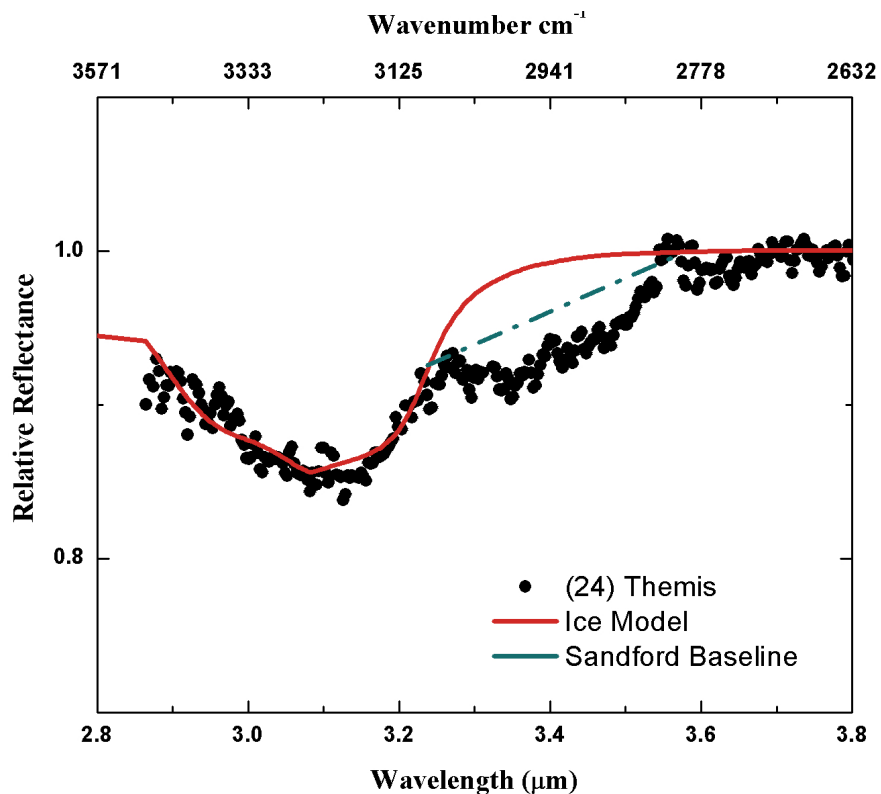


Figure 5.5: **Possible baselines for analysis of C-H stretch region.** Shown is the spectrum of asteroid (24) Themis with two possible baselines to isolate the C-H stretch organic features. We chose to use the blue dashed baseline for our asteroids, as well as our laboratory spectra.

5.4.1 Identification of organic band centers and strengths

The identification of the band minima and band strengths of the C-H stretch features is the first step to our understanding the nature of carbonaceous material in our laboratory and asteroid spectra.

The asymmetric and symmetric C-H stretch band positions for the $-\text{CH}_2-$ and $-\text{CH}_3$ groups are well documented for many astronomical objects. These band positions are extremely useful for com-

parison, and are diagnostic of, for example, aliphatic hydrocarbons that contain other perturbing chemical groups [85].

To characterize these band minima we first defined then removed the baseline, which converted our spectra into absorbance (optical depth) for analysis of the band profiles and strengths [80]. We defined our baselines in the 3.2 to 3.6 μm range (Figure 5.5), identical to that in Sandford et al. (1991) [80] as it yields conservative lower limits to the C-H stretch absorption strength compared to the ice model used in other studies [3] [86]. Once we removed the baselines, we fit Gaussians to all our laboratory spectra (e.g. Figure 5.6) and to our two asteroid spectra (Figures 5.7 and 5.8). We implemented the Levenburg-Marquardt gradient method for minimizing our Gaussian fits to the organic features. This method provided us with not only the position of the C-H stretch bands but the band strength τ (optical depth at band minimum), and $\Delta\nu$ (full-width-at-half-maximum) that is useful for our calculations of the column densities.

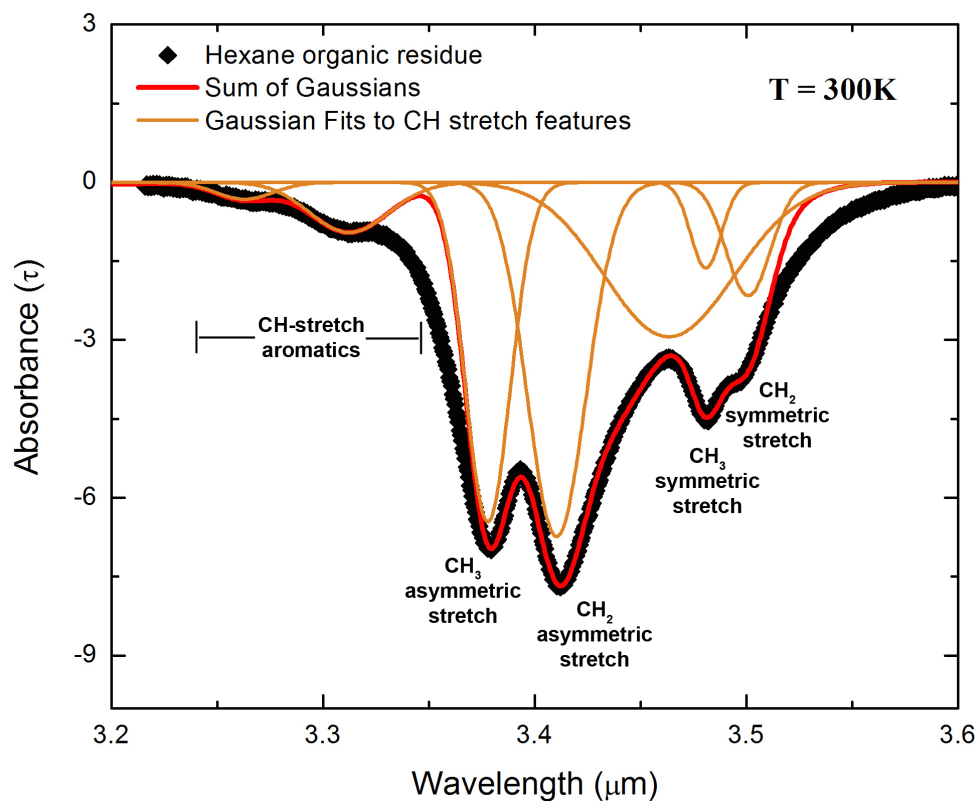


Figure 5.6: **Laboratory spectra organic gaussian deconvolution.** We used Gaussian deconvolution to determine the optical depth (τ), FWHM, and band centers of the organic features. We show the complex organic residue produced by the starting mixture that contained the alkane hexane. We fit several Gaussians (orange) to the features produced by aromatics, aliphatics and possibly tertiary carbon ($\sim 3.45 \mu\text{m}$). In the $3.3\text{-}3.35 \mu\text{m}$ region and the $3.5\text{-}3.55 \mu\text{m}$ region the data (black) are not well fit to the sum of the Gaussians (red). This may be due to band broadening or wings on the CH_3 asymmetric feature and the CH_2 symmetric stretch feature.

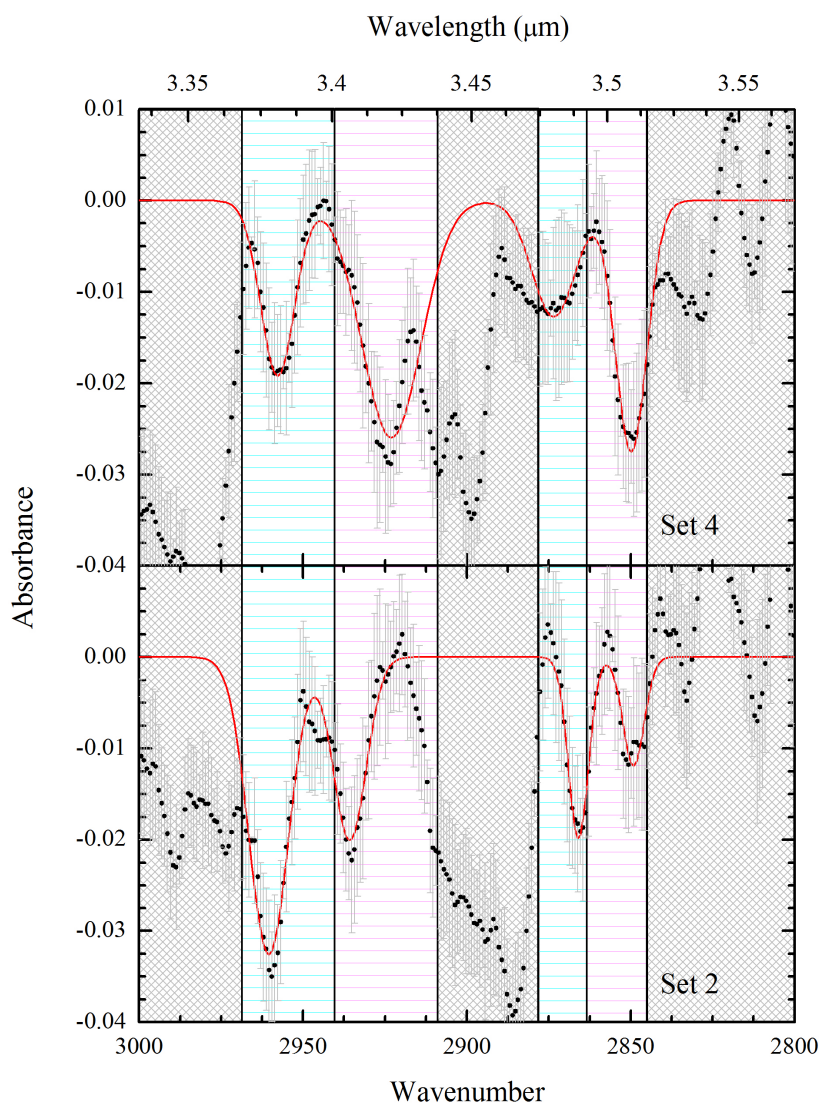


Figure 5.7: **Asteroid (24) Themis organic gaussian deconvolution.** We applied a Gaussian deconvolution method to the aliphatic features in two sets of our higher S/N spectra of (24) Themis. We focused only on the four aliphatic C-H stretch features, although there may be other features such as tertiary carbon around $3.45 \mu\text{m}$. Our two sets of spectra may indicate the organics are different as this asteroid rotates. These data have been smoothed using adjacent averaging techniques.

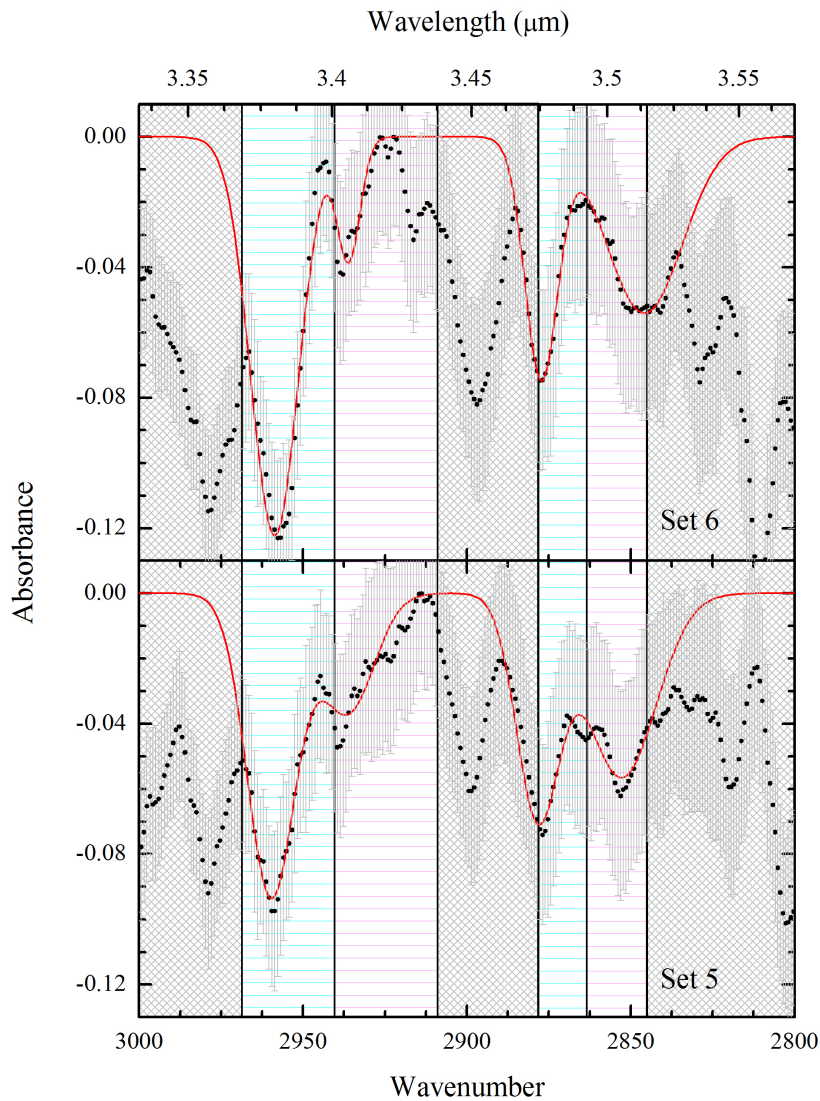


Figure 5.8: **Asteroid (65) Cybele organic gaussian deconvolution.** We applied a Gaussian deconvolution method to the aliphatic features in two sets of our higher S/N spectra of (65) Cybele. We have focused on only the four aliphatic C-H stretch features, although there may be other features such as tertiary carbon around $3.45 \mu\text{m}$, similar to Themis. These data have been smoothed using adjacent averaging techniques.

We determined that the minimum number of Gaussians we needed to describe our laboratory spectra was seven; two from naphthalene around 3.25 and 3.3 μm , four from aliphatics at \sim 3.38, 3.42, 3.48, and 3.5 μm , and one from tertiary carbon at 3.45 μm . For our asteroid spectra we found that only the four aliphatic features were necessary to describe our spectra. However we see several weaker features in the asteroid spectra, around 3.35, and 3.54 μm that can be attributed to methanol (CH_3OH) or formaldehyde (H_2CO) [87]. We also detect a stronger feature near 3.45 μm that we suggest is due to the presence of tertiary carbon [87].

5.4.2 Calculation of Optical Depths and Column Densities

Using τ , and $\Delta\nu$ from our determination of the band profiles and strengths we can calculate three interesting parameters. The first is the $\tau_{\text{CH}_2}/\tau_{\text{CH}_3}$ ratio. This is a simple calculation describing the optical depth of the CH_2 asymmetric stretch feature to that of the CH_3 asymmetric stretch feature. This value can provide us with a rough estimate of the chain length and/or branching nature of the aliphatic carrier. The second is the column density, N , which is a quantitative method to measure material producing an infrared absorption. This value can be determined for the asymmetric $-\text{CH}_2-$ and $-\text{CH}_3$ groups with

$$N = \frac{\tau\Delta\nu}{A}, \quad (5.2)$$

where A is the integrated absorbance in cm group^{-1} [88]. Using N_{CH_2} and N_{CH_3} from equation 5.2, we can determine the functional groups in the abundance ratio $N_{\text{CH}_2}/N_{\text{CH}_3}$. This ratio provides us insight into the abundance of C atoms contributing to the aliphatic $-\text{CH}_2-$ or $-\text{CH}_3$ groups [89], thus helping us to narrow down the properties of the aliphatic carrier responsible for the C-H stretch features in our laboratory and asteroid spectra. This ratio is also indicative of the average aliphatic chain length and branching nature of aliphatic material. For example, a higher $N_{\text{CH}_2}/N_{\text{CH}_3}$ ratio suggests longer aliphatic chains and/or more cyclic aliphatic structures, and, conversely, a lower ratio would indicate shorter chain lengths and/or higher branching levels [81]. This ratio has been extensively calculated for primitive meteorites [82] [90] [91], IDPs [83], the DISM [80] [84], and even the sample dust returns from comet Wild 2 [92] [93] [94] [95] [83].

5.5 Results

5.5.1 Laboratory Samples

Figure 5.9 shows our laboratory samples (a) during the warm-up phase of the experiment at a temperature of 235 K, and (b) at 300 K, or room temperature. The spectra have been normalized such that the $3\text{-}\mu\text{m}$ features are of constant depth. In the spectra presented in Figure 5.9 (a) we detect features due to H_2O ice, aromatic and aliphatic hydrocarbons, $\text{C}=\text{O}$ (carbon double bonded with oxygen), $\text{C}=\text{C}$ (carbon double bonded with carbon in aromatic rings), and others. The presence of

ice at 235 K is interesting, and we plan to continue our work in an effort to understand this phenomenon. The spectra in Figure 5.9 (b) no longer show evidence of ice or other volatiles, rather there are features due to OH, C=O, C=C, and other indications of complex organic material.

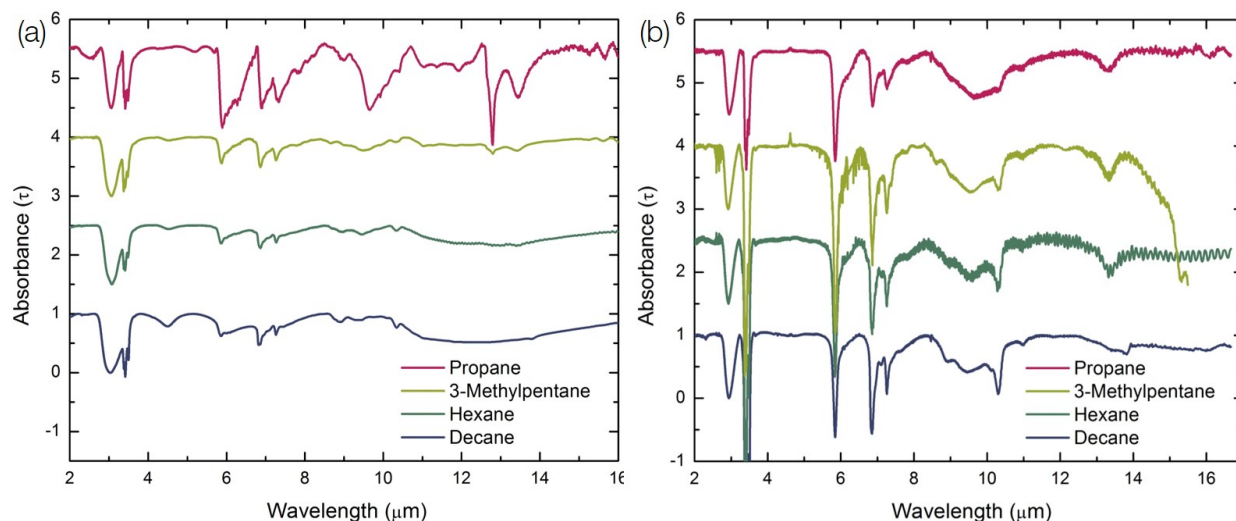


Figure 5.9: **Laboratory residues at 235 K and 300 K.** Shown are the laboratory samples at (a) 235 K and (b) 330 K. At 235 K we find several features due to H₂O ice, aromatic and aliphatic hydrocarbons, C=O, C=C. At 300 K, once all volatiles have sublimated, we find absorptions due to OH, C=O, C=C, and complex organic material.

Figure 5.10 shows our laboratory samples in the 3.2-3.5 μm range after the warm-up phase of the experiment at a temperature of 300 K, or roughly room temperature. The spectra have been normalized such that the -CH₂- asymmetric stretch features are of constant depth. The organics present in the 3.35-3.5 μm region are room-temperature stable, and did not sublime with the other volatiles during warm-up. The depth of the -CH₃ and -CH₂- asymmetric stretch features are

intrinsically stronger than the -CH_3 and $\text{-CH}_2\text{-}$ the symmetric stretch features. Depending on the chain length or the amount of branching in the organics, the -CH_3 or $\text{-CH}_2\text{-}$ asymmetric stretch features will be deeper relative to the other, or in some cases equivalent. This same ratio should also hold for the symmetric stretch features, though in several of our spectra it did not. We believe this may be the result of tertiary carbon that affects the appearance of the $\text{-CH}_2\text{-}$ and the -CH_3 symmetric stretch features.

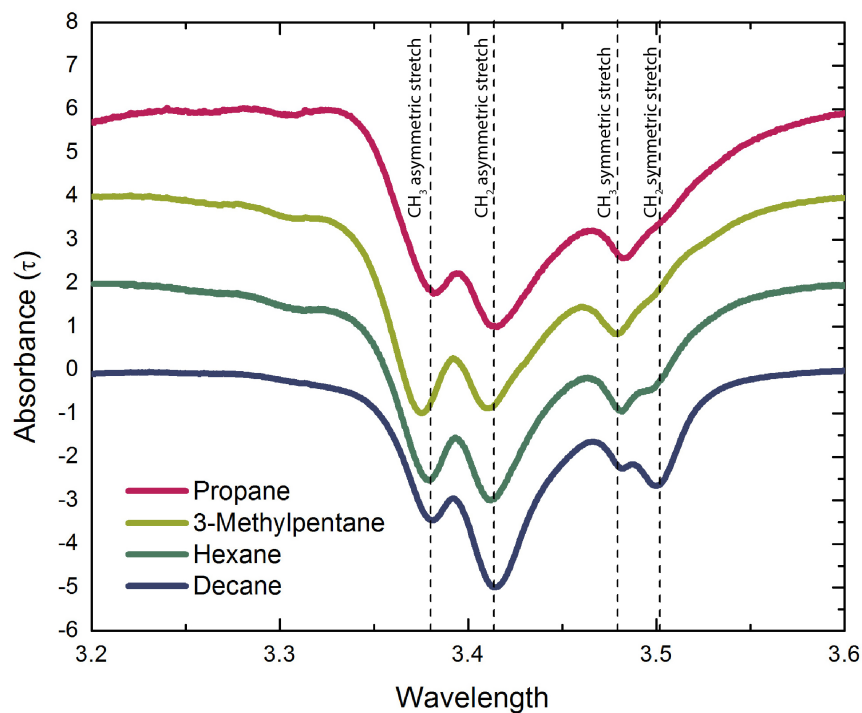


Figure 5.10: **Laboratory residues in the 3.2-3.6 μm region at 300 K.** Dashed lines locate the positions of the four aliphatic C-H stretch features.

In Figure 5.10, our propane organic residue shows a higher abundance of $\text{-CH}_2\text{-}$ groups as indicated by the deeper $\text{-CH}_2\text{-}$ asymmetric stretch feature at roughly $3.42 \mu\text{m}$ compared to the

-CH₃ asymmetric stretch feature at 3.38 μm . The -CH₂- symmetric stretch feature at 3.48 μm should also be deeper relative to the -CH₃ symmetric stretch feature at 3.50 μm but it does not appear this way. The 3-methylpentane organic residue shows a higher abundance of -CH₃ groups as indicated by a deeper -CH₃ asymmetric stretch feature at 3.38 and 3.42 μm . The spectrum of the hexane organic residue shows a deeper -CH₂- asymmetric stretch feature, with a more pronounced -CH₃ symmetric stretch feature. Lastly, our decane organic residue shows that this material is dominated by -CH₂- groups, with strong features at 3.42 and 3.5 μm due to the -CH₂- asymmetric and symmetric stretch features, respectively.

5.5.2 Band Centers of C-H stretch Aliphatic Features

We have determined the band centers of the C-H stretch aliphatic features in our laboratory organic residues and in our asteroid organics. We summarize all band centers in Table 5.2.

Table 5.2: Position of Aliphatic CH Stretch Features

<i>Organic Source</i>	<i>-CH₃ Asymmetric</i>	<i>-CH₂- Asymmetric</i>	<i>-CH₃ Symmetric</i>	<i>-CH₂- Symmetric</i>
(24) Themis (set 2)	3.38	3.41	3.49	3.51
(24) Themis (set 4)	3.38	3.42	3.48	3.51
(65) Cybele (set 5)	3.38	3.41	3.48	3.51
(65) Cybele (set 6)	3.38	3.41	3.48	3.51
Propane Experiment	3.38	3.41	3.48	3.51
3-MP Experiment	3.38	3.41	3.48	3.50
Hexane Experiment	3.38	3.41	3.48	3.50
Decane Experiment	3.38	3.42	3.48	3.50

Columns indicate the source of organic material, and the band centers in μm of the four aliphatic C-H stretch features in our asteroid and laboratory samples.

5.5.3 Optical Depths and Column Densities

We calculated N for the asymmetric $-\text{CH}_2-$ and $-\text{CH}_3$ groups in our laboratory and asteroid organics using the band depth, τ , and its full-width-at-half-maximum, $\delta\nu$ in cm^{-1} , that we determined from our Gaussian deconvolution methods. We list these values for our laboratory samples in Table 5.3, and for our asteroid spectral sets in Table 5.4. We did not calculate N for the symmetric $-\text{CH}_2-$ and $-\text{CH}_3$ groups as these features are intrinsically weaker, and may be blended or suppressed in some of our data sets.

Table 5.3: Optical Depth and Column Densities of the Methyl (-CH₃) and Methylene (-CH₂-) Components of our Laboratory Samples.

<i>Organic Material</i>	<i>Parameters</i>	<i>-CH₃ Asymmetric</i>	<i>-CH₂- Asymmetric</i>
H ₂ O + C ₁₀ H ₈ + C ₃ H ₈ (Propane)	τ	0.012	0.013
	$\Delta\nu$	22	34
	N	2.20×10^{16}	5.97×10^{16}
H ₂ O + C ₁₀ H ₈ + C ₆ H ₁₄ (3-MP)	τ	0.031	0.025
	$\Delta\nu$	26	25
	N	6.72×10^{16}	8.45×10^{16}
H ₂ O + C ₁₀ H ₈ + C ₆ H ₁₄ (Hexane)	τ	0.063	0.072
	$\Delta\nu$	22	32
	N	1.16×10^{17}	3.11×10^{17}
H ₂ O + C ₁₀ H ₈ + C ₁₀ H ₂₂ (Decane)	τ	0.071	0.11
	$\Delta\nu$	21	29
	N	1.24×10^{17}	4.31×10^{17}

τ (absorbance), $\Delta\nu$ (cm⁻¹), and N (group cm⁻²) are given. For the -CH₃ and -CH₂- asymmetric stretch features we used $A/CH_3 = 1.2 \times 10^{-17}$, and $A/CH_2 = 7.4 \times 10^{-18}$ with units of cm group⁻¹. We adapted these values from [80].

In Table 5.5 we list the initial and final τ_{CH_2}/τ_{CH_3} ratios for our laboratory organics. The initial material has had no UV irradiation, while our final organic residue has been subjected to approximately 72 hours.

Table 5.4: Optical Depth and Column Densities of the Methyl (-CH₃) and Methylene (-CH₂-)

Components of Select Asteroid Spectral Sets.

<i>Organic Material</i>	<i>Parameters</i>	<i>-CH₃ Asymmetric</i>	<i>-CH₂- Asymmetric</i>
(24) Themis (set 2)	τ	0.046	0.033
	$\Delta\nu$	18.3	16.5
	N	6.93×10^{16}	7.40×10^{16}
(24) Themis (set 4)	τ	0.021	0.029
	$\Delta\nu$	14.6	23.4
	N	2.59×10^{16}	9.10×10^{16}
(65) Cybele (set 5)	τ	0.093	0.037
	$\Delta\nu$	17.2	19.1
	N	1.33×10^{17}	9.45×10^{16}
(65) Cybele (set 6)	τ	0.122	0.038
	$\Delta\nu$	17.2	8.27
	N	1.33×10^{17}	4.20×10^{16}

τ (absorbance), $\Delta\nu$ (cm⁻¹), and N (group cm⁻²) are given. For the -CH₃ and -CH₂- asymmetric stretch features we used $A/CH_3 = 1.2 \times 10^{-17}$, and $A/CH_2 = 7.4 \times 10^{-18}$ with units of cm group⁻¹.

We adapted these values from [80].

Table 5.5: N_{CH_2}/N_{CH_3} Ratios for Our Laboratory Organics

<i>Organic Material</i>	<i>Initial</i>	<i>Final</i>	<i>Initial</i>	<i>Final</i>
	τ_{CH_2}/τ_{CH_3}	τ_{CH_2}/τ_{CH_3}	N_{CH_2}/N_{CH_3}	N_{CH_2}/N_{CH_3}
	(no UV)	(~ 72 hrs UV)	(no UV)	(~ 72 hrs UV)
H ₂ O + C ₁₀ H ₈ + C ₃ H ₈ (Propane)	0.3	1.1	0.6	2.7
H ₂ O + C ₁₀ H ₈ + C ₆ H ₁₄ (3-MP)	0.3	0.8	0.6	1.3
H ₂ O + C ₁₀ H ₈ + C ₆ H ₁₄ (Hexane)	0.8	1.1	1.6	2.7
H ₂ O + C ₁₀ H ₈ + C ₁₀ H ₂₂ (Decane)	1.4	1.5	2.7	3.5

N_{CH_2}/N_{CH_3} Ratios for our laboratory samples. Note how the initial τ_{CH_2}/τ_{CH_3} and N_{CH_2}/N_{CH_3} ratios of our organic spectra have increased in all cases, indicating that the complex organic residues have grown in chain-length (CH₂ groups).

In Table 5.6 we list the average τ_{CH_2}/τ_{CH_3} and N_{CH_2}/N_{CH_3} ratios for our asteroid organics. We first calculated the τ_{CH_2}/τ_{CH_3} and N_{CH_2}/N_{CH_3} ratios for each asteroid set, using the values listed in Table 5.4, then averaged the results.

Table 5.6: τ_{CH_2}/τ_{CH_3} and N_{CH_2}/N_{CH_3} Ratios for Our Asteroid Organics

<i>Organic Source</i>	<i>Average τ_{CH_2}/τ_{CH_3}</i>	<i>Average N_{CH_2}/N_{CH_3}</i>
(24) Themis	1.1	2.3
(65) Cybele	0.4	0.5

We calculated the τ_{CH_2}/τ_{CH_3} and N_{CH_2}/N_{CH_3} ratios independently for each set using the values listed in 5.4. We then took the average of these ratios.

5.6 Discussion

We find that both initial τ_{CH_2}/τ_{CH_3} and N_{CH_2}/N_{CH_3} ratios of our laboratory organics have increased after UV photolysis. Table 5.5 summarizes these results. When we consider the increased final τ_{CH_2}/τ_{CH_3} and N_{CH_2}/N_{CH_3} ratios this may indicate that the complex organic residues have likely grown in chain-length (-CH₂- groups) from that of our starting mixtures. We also found an interesting trend that suggests the amount of increase in these ratio is inversely proportional to the chain length of the original alkane. For instance propane, the shortest alkane (i.e fewest -CH₂- groups), had the largest percent increase from the initial τ_{CH_2}/τ_{CH_3} ratio to the final, and the initial

N_{CH_2}/N_{CH_3} ratio to the final. This trend held for all other alkanes. Although an explanation for this behavior is beyond the scope of this work.

Table 5.7: Optical Depth and Functional Group Ratios of Asteroids and Astronomical Sources

<i>Organic Material</i>	τ_{CH_2}/τ_{CH_3}	N_{CH_2}/N_{CH_3}	Possible Lab Residue	<i>Reference</i>
(65) Cybele	0.4	0.5	None	This study
(24) Themis	1.1	2.3	3-MP-Propane/Hexane	This study
DISM	0.92-1.3 [†]	2.0-2.5 [‡]	3-MP-Propane/Hexane	[95] [†] , [85] ^{†‡} , [80] [‡]
Wild 2 Sample Return	–	2.5-5.2	3-MP-Decane	[92], [94], [95]
Hydrous IDPs	1.0-5.3 [†]	2.8-5.5 [‡]	Propane/Hexane-Decane	[91] [‡] , [89] [‡]
Anhydrous IDPs	1.2-5.6 [†]	2.8-5.5 [‡]	Propane/Hexane-Decane	[91] [†] , [89] [‡]
Iapetus	–	3.0-4.0	Decane	[96]

Based on the available N_{CH_2}/N_{CH_3} ratios, we provide comparable laboratory residues for each source of organic material. When our laboratory residues do not provide a close match, we have determined a range of laboratory samples that the organic material is likely between. When both ratios are available crosses denote citations for the τ_{CH_2}/τ_{CH_3} ratios, and double crosses for the N_{CH_2}/N_{CH_3} ratios.

We compare the τ_{CH_2}/τ_{CH_3} and N_{CH_2}/N_{CH_3} ratios of asteroid (24) Themis and (65) Cybele with other astronomical sources. We also suggest possible lab analogs for each source of organic material based on available N_{CH_2}/N_{CH_3} ratios. Our results are listed in Table 5.7. We have analyzed several rotationally resolved data sets for each asteroid, and we have averaged the τ_{CH_2}/τ_{CH_3} and N_{CH_2}/N_{CH_3} ratios of these sets. We calculated a τ_{CH_2}/τ_{CH_3} ratio of 1.1 for Themis, and 0.4 for

Cybele. These values suggests that the asteroid organics may be relatively short in chain length with few $-CH_2-$ groups, and/or highly branched with additional $-CH_3$ bonded to the available $-CH_2-$ groups. Based on the lower τ_{CH_2}/τ_{CH_3} and N_{CH_2}/N_{CH_3} ratios, the organics on Cybele may be even more disordered than those on Themis. Although we note that the S/N of our Cybele data was lower than that for Themis, making our analysis of the individual organic features very challenging. When comparing Cybele to other astronomical objects we did not find a match with meteorites, comets, IDPs, or interstellar sources. This may be due to the lower S/N of our asteroid data, or possibly that we have no representative sample of the organics on Cybele. In contrast, the τ_{CH_2}/τ_{CH_3} ratio for Themis is comparable to what is observed for Interstellar Hydrocarbon, and the lower limit of the ratio for IDPs (Table 5.7). However the average τ_{CH_2}/τ_{CH_3} ratio of the DISM is identical to that of Themis, whereas the average for IDPs is significantly higher. Moreover the average N_{CH_2}/N_{CH_3} ratio of the DISM is more consistent with Themis than this average for IDPs, which is also significantly higher. A relationship with interstellar organics is interesting when considering the $3.45 \mu\text{m}$ feature in the spectra of Themis (and Cybele). This absorption has been detected in several dense molecular clouds, and has been attributed to tertiary carbon arranged in a diamond-like structure [87]. These “interstellar diamonds” may further suggest an interstellar source for the organics on Themis (and possibly Cybele).

Interestingly, the C-H stretch aliphatic features in the spectra of several primitive chondrites share striking similarities to the features observed in the spectra of interstellar sources, such as the

DISM [97] [90] [98] [99], and Table 5.8 shows that some of these chondrites may also be comparable to the organics present on Themis. The aliphatic organic material in the DISM likely originated from the outflow region of evolved carbon-rich stars [100], which was then incorporated into the solar nebula, and eventually solar system bodies. These hydrocarbons survived relatively unaltered in the most primitive of these bodies, fragments of which are likely CI/CM/CR carbonaceous chondrites. Our analysis of the Themis organics τ_{CH_2}/τ_{CH_3} and N_{CH_2}/N_{CH_3} ratio are similar to several CI/CM/CR chondrites, suggesting this asteroid may be representative of a source for such primitive meteorites. For example, carbonaceous Chondrites Murchison (CM2), Orgueil (CI1), Tagish Lake (CI2), and Bells (CM2) have minimum τ_{CH_2}/τ_{CH_3} ratios close to that of Themis. When considering the N_{CH_2}/N_{CH_3} ratio for Themis several other meteorites are comparable, having average N_{CH_2}/N_{CH_3} ratios close to that of Themis. These meteorites include Renazzo (CR2), Nogoya (CM2), and Paris (CM). The average of the τ_{CH_2}/τ_{CH_3} and N_{CH_2}/N_{CH_3} ratios for all CM2 chondrites is most consistent with that for (24) Themis. This result is consistent with work by DeLeon (2012) that suggests the visible spectra of (24) Themis is most similar to CM2 chondrites [101].

Similarities between primitive CI and CM meteorites and the Themis family are not surprising. Most CIs are petrologic type 1 and CMs type 2, indicating they experienced extreme and significant aqueous alteration, respectively. Several members of the Themis family show evidence of hydrated minerals such as OH-dominated minerals (phyllosilicates), and/or oxidized iron in phyllosilicates,

indicating they too have experienced some degrees of aqueous alterations. There is also evidence that the chemical heterogeneity of type 1 and 2 chondrites may be related to short-duration thermal processing on the asteroid parent body [102] rather than aqueous alteration, however there are models that suggest that the parent body of the Themis family underwent significant thermal evolution early in its history [103]. Heating of aliphatic hydrocarbons increases the amount of aromatic hydrocarbons, while shortening the aliphatic chains [99]. These variations in thermal processing, and/or formation environment could explain why, for example, Themis organics are only slightly different from that of IDPs and extremely different from Saturn's moon Iapetus and meteorite Sutter's Mill (SM2).

There are other factors that can contribute to the low τ_{CH_2}/τ_{CH_3} and N_{CH_2}/N_{CH_3} ratios we calculated for Themis and Cybele, such as irradiation by high-energy particles, which tends to destroy $-CH_2$ groups, shortening aliphatic chains [99]. The Themis family is one of the oldest known asteroid families, subjected to billions of years of irradiation. Should a meteorite exist in our current collection that originated from Themis, it may not have experienced the same amount of irradiation as the bulk surface of Themis. This could hamper our attempts to make solid parent body-meteorite connections based on the spectral signatures of aliphatic hydrocarbons alone. Ideally we would like to measure the amount of aromatic material in the spectra of Themis and Cybele for comparison with other astronomical sources, and meteorites. However quantifying the amount of this particular material is difficult. The C-H stretch absorption feature of aromatic hydrocarbons

($\sim 3.28 \mu\text{m}$), is weak compared to the aliphatic features. Aromatics are bonded to fewer hydrogen atoms per carbon atom ($\text{H/C} < 1$) than aliphatics ($\text{H/C} < 2$). This causes the intrinsic strength of the aromatic C-H stretch absorptions to be 2-3 times lower than that for aliphatics [100]. Also when using remote spectroscopy we can only detect the outer "shell" of a more complex aromatic structure, so our attempts to estimate the abundance of carbon contributing to aromatic molecules may be significantly underestimated. Even without quantifying the amount of aromatic material we can, however, place constraints on the aliphatic hydrocarbons, and we have done so by comparing the laboratory spectra of organic residues with the spectra of Themis and Cybele.

We have determined which laboratory organic residue is most similar to our asteroid organics. The $\tau_{\text{CH}_2}/\tau_{\text{CH}_3}$ ratio for our samples containing 3-methylpentane and propane were 0.3 before UV irradiation. These un-irradiated samples are most consistent with (65) Cybele's $\tau_{\text{CH}_2}/\tau_{\text{CH}_3}$ of 0.4, and may be representative of the organics on Cybele. The $N_{\text{CH}_2}/N_{\text{CH}_3}$ ratio of 0.5 for Cybele is not consistent with any of our laboratory samples. This lower $N_{\text{CH}_2}/N_{\text{CH}_3}$ ratio may in part be due to the smaller FWHM we measured for Cybele's -CH₂- asymmetric stretch feature ($\delta\nu=8.3 \text{ cm}^{-1}$) in set 6, whereas the canonical value is normally between 17-22 cm^{-1} .

Table 5.8: Optical Depth and Functional Group Ratios of Asteroids and Meteorites

<i>Organic Material</i>	τ_{CH_2}/τ_{CH_3}	N_{CH_2}/N_{CH_3}	Possible Lab Residue	<i>Reference</i>
(65) Cybele	0.4	0.5	None	This study
(24) Themis	1.1	2.3	3-MP-Propane/Hexane	This study
Alais (CI1)	–	1.5-1.8	3-MP-Propane/Hexane	[102]
Murchison (CM2)	1.1-1.5†	1.5-2.0‡	3-MP-Propane/Hexane	[91]†, [104]†, [102]‡
PCA91008 (CM2)	–	1.6-2.2	3-MP-Propane/Hexane	[102]
Ivuna (CI1)	–	1.7-2.1	3-MP-Propane/Hexane	[102]
EET92042 (CR2)	–	1.7-3.2	3-MP-Propane/Hexane	[102]
Orgueil (CI1)	1.0-1.5†	1.8-2.0‡	3-MP-Propane/Hexane	[90]†, [104]†, [102]‡
Tagish Lake (C2)	1.2-4.4†	1.9-2.6‡	3-MP-Propane/Hexane	[82]‡, [105]†, [102]‡
QUE99177 (CR2)	–	1.9-2.1	3-MP-Propane/Hexane	[102]
Renazzo (CR2)	–	1.9-2.2	3-MP-Propane/Hexane	[102]
Nogoya (CM2)	–	2.0-2.6	3-MP-Propane/Hexane	[102]
Paris (CM)	–	2.2	3-MP-Propane/Hexane	[99]
Cold Bokkeveld (CM2)	–	2.4-2.8	3-MP-Decane	[102]
Semarkona (LL3)	–	2.4-2.9	3-MP-Decane	[102]
QUE93005 (CM2)	–	2.4-3.4	3-MP-Decane	[102]
Bells (CM2)	1.4	–	–	[104]
QUE93005 (CM2)	–	3.0-4.0	Propane/Hexane-Decane	[102]
Sutter’s Mill (SM2)	2.4-4.0	–	–	[106]
NWA852 (CR2)	2.5	–	–	[107]

Based on the available N_{CH_2}/N_{CH_3} ratios, we provide comparable laboratory residues for each source of organic material. When our laboratory residues do not provide a close match, we have determined a range of laboratory samples that the organic material is likely between. When both ratios are available crosses denote citations for the τ_{CH_2}/τ_{CH_3} ratios, and double crosses for the N_{CH_2}/N_{CH_3} ratios.

The τ_{CH_2}/τ_{CH_3} ratio for Themis is equal to 1.1, identical to that of our propane and hexane residues. These hydrocarbons before irradiation had chain lengths ranging from 1-4. After irradiation the chain length of the residues increased to an undetermined amount, but may still be consistent with analysis of the DISM organics that were found to have individual chains lengths no longer than 4-5 [97]. The N_{CH_2}/N_{CH_3} ratio for Themis (2.3) is a value between the N_{CH_2}/N_{CH_3} ratios of 3-methylpentane and propane/hexane, also consistent with a rather short-chained and/or branched material implied by the τ_{CH_2}/τ_{CH_3} ratios. However, it is likely that the organics on Themis and Cybele can not be described by one type of aliphatic carrier, but may consist of a structurally complex combination. Similar to the IOM of Chondrites, the organics may be composed of aromatic hydrocarbons cross-linked by short chains of $-CH_2-$ groups, ranging in chain length, with $-CH_3$ groups bonded to these available $-CH_2-$ groups in a highly disordered manner [108].

We find that overall the laboratory residue that is least consistent with our asteroids is that which originally contained decane. Its τ_{CH_2}/τ_{CH_3} ratio of 1.5 and N_{CH_2}/N_{CH_3} of 3.5 implies that this organic residue has long chains of $-CH_2-$ groups. This is not surprising as decane has eight $-CH_2-$ groups intrinsically, and UV irradiation seems to have further lengthened this chain. These excess $-CH_2-$ groups in our decane residue is the least consistent with our asteroid organics as it has excess $-CH_2-$ groups not apparent in the asteroid spectra. Our decane residue is most similar to the organics of the distant, out solar system moon Iapetus. It is possible that the differences

between Themis and Cybele organics with the organics on Iapetus are related to variations in thermal processing.

Table 5.9: Position of Aliphatic C-H stretch Features

<i>Organic Source</i>	<i>-CH₃ Asymmetric</i>	<i>-CH₂- Asymmetric</i>	<i>-CH₃ Symmetric</i>	<i>-CH₂- Symmetric</i>
Avg. DISM, IDP	3.39	3.42	3.48	3.51
Cold Bokkeveld	3.38	3.42	3.48	3.51
Wild 2 Stardust Track	3.38	3.42	3.50	3.50
(24) Themis (set 2)	3.38	3.41	3.49	3.51
(24) Themis (set 4)	3.38	3.42	3.48	3.51
(65) Cybele (set 5)	3.38	3.41	3.48	3.51
(65) Cybele (set 6)	3.38	3.41	3.48	3.51
Propane Experiment	3.38	3.41	3.48	3.51
3-MP Experiment	3.38	3.41	3.48	3.50
Hexane Experiment	3.38	3.41	3.48	3.50
Decane Experiment	3.38	3.42	3.48	3.50
Methanol	3.35	–	3.54	–
Methylcyanide	3.33	–	3.40	–

Columns indicate the source of organic material, and the band centers in μm of the four aliphatic C-H stretch features in our asteroid organics, laboratory samples, and other astronomical sources [80] [92] [109] [86].

Lastly, we have compared the band positions of the C-H stretch aliphatic features present in our organic residues to those in our asteroid spectra and other astronomical sources (Table 5.9). We find that the -CH_3 and $\text{-CH}_2\text{-}$ asymmetric and symmetric stretch features of our asteroid organics are most consistent with the DISM, IDPs, and our laboratory samples. The band centers of Themis (set 4) organics are identical to meteorite Cold Bokkeveld. The Themis and Cybele organics are least consistent with methanol and methylcyanide, aliphatics with electronegative groups such as aromatic rings, hydroxy (-O-H) or cyano ($\text{-C}\equiv\text{N}$) chemically bonded adjacent to the C-H bonds [80]. However Themis and Cybele have weaker features around $3.35\ \mu\text{m}$ and $3.54\ \mu\text{m}$ (see Figures 5.7 and 5.8), and these features could be due to the presence of aliphatics bonded to electronegative groups. Both asteroids have absorptions around $3.3\ \mu\text{m}$ from the presence of aromatic hydrocarbons. It is possible that both types of aliphatics are represented on these asteroids, aliphatics chemically bonded to electronegative groups (i.e. aromatics), and those that are not.

CHAPTER 6

CONCLUSIONS AND FUTURE WORK

This work combines four projects related to furthering our understanding of the mineralogy and composition of asteroids. Asteroids represent a promising frontier for exploring some of the big picture questions that still remain in planetary science, such as *what are the characteristics of the solar system that lead to the origins of life?*. By studying primitive solar system bodies we can begin to answer this intriguing question. We know now that some of these dark, primitive asteroids harbor water ice and organics, essential ingredients for life to arise and flourish. These materials were likely incorporated into their composition during the formation of these objects in the outer reaches of the solar system [77]. Hypotheses such as the Nice model [79] and Grand Tack [78] suggest these distant asteroids were transported into the inner solar system, where many were delivered to Earth by impacts about 4 billion years ago. The remaining objects now reside mainly in the middle and outer main belt, where we can fairly easily study them today with ground-based and space-based telescopes. By understanding these primitive asteroids, we can reveal their connection to our planet's oceans, water, and, ultimately, life.

6.1 Conclusions

Our first project in this work investigated the surface composition of several outer main belt asteroids. This project was motivated by our detection of a rounded 3- μm absorption due to water-ice and 3.2-3.6 μm absorptions indicative of complex organics [1] [2] [3] on the largest members of the Themis family, (24) Themis, and the Cybele group, (65) Cybele. We predicted that other members of these populations may also exhibit similar features, thus we investigated a small sample of primitive asteroids belonging to the Themis family and Cybele group using near-infrared 2-4 μm spectroscopy. We found that (90) Antiope, a member of the Themis family, likely has a rounded 3- μm feature similar to (24) Themis. In the Cybele group we found that (107) Camilla, and (790) Pretoria have rounded 3- μm features similar to (65) Cybele. Asteroid (121) Hermione is the only member of this population to exhibit a sharp 3- μm feature due to hydroxyl. Understanding the diversity of aqueous and thermal processing within populations of primitive asteroids is important for geophysical evolution models of volatile-rich asteroid families [103], dynamical models of the solar system [110], and the water and organic inventory of earth.

In our second study, we focused on the mid-infrared 8-13 μm region. Of the asteroids for which we obtained near-infrared 2-4 μm spectra we analyzed their available mid-infrared 8-13 μm spectra that we obtained from a public database of Spitzer Space Telescope observations. In the 8-13 μm region is the strongest vibrational mode of Si-O, the Si-O stretch fundamental. This

emission from silicates creates an emission plateau centered at 10 μm , and the strength of this emission is due to fine-grained silicates in a transparent matrix or an under-dense "fairy castle" structure [38] on the surface of asteroids. Asteroids (24) Themis, (65) Cybele, and (107) Camilla have well-defined, rounded 10 μm emissions with a contrast of roughly 4-5%; while asteroid (90) Antiope and (121) Hermione show no emission in the 8-13 μm region. The emission spectra of these primitive, hydrated asteroids is in stark contrast to the stronger 10-15% emission of Jupiter Trojan asteroids [38]. It is likely that our sample asteroids have a different surface structure than the Trojans, with Trojans having the most "fluffy" surface structure and (121) Hermione and (90) Antiope having the least [4] [17]. Asteroids (24) Themis, other Themis family members, (107) Camilla, and (65) Cybele have surface textures intermediate between the Trojans and, for example, (90) Antiope [3] [75] [4] [17]. We conclude that these asteroids with emission strengths ranging between (0-5%) have larger surface grains, and thus lower surface porosities than the Trojans as a result of aqueous processes that produced their visible and near-infrared hydration features.

For our third study, also in the mid-infrared 8-13 μm region, we turned our focus to understanding the relationship between any mineralogy and hydration inferred in the visible and near-infrared with the shape, strength, and slope of the 10 μm emission. We averaged Bus C-complex, D-types, and S-types, finding that these classes defined so by their visible spectra clearly cluster into 3 statistically distinct groups based on their 8-13 μm spectra. Our results suggest that asteroids grouped by their visible spectra (taxonomy) similarly group in mid-infrared, validating the robustness of

visible taxonomy and the relationship between features present at disparate wavelength regimes. We also find that the contrast and rounded shape of the 10 μm emission spectra may be an indicator of the amount of hydration processing that an asteroid has experienced. For example, that D-type asteroids have not been heated enough for aqueous alterations and conversely, that the C-types have. This larger sample of asteroid spectra confirms the results of our previous study of hydrated Themis and Cybele asteroids.

In our last study we simulated organics in a laboratory to provide us with a more detailed understanding of the organics we have observed on asteroids. We created several ice mixtures containing water and simple hydrocarbons (alkanes), starting materials that we believe may have been present in the solar system during the formation of asteroids. We have compared our laboratory organics both quantitatively and qualitatively to the organics detected on asteroids and other astronomical sources. We find that the aliphatic features in the spectra of (24) Themis and (65) Cybele are consistent with our laboratory organics, and/or other astronomical sources.

We calculated τ_{CH_2}/τ_{CH_3} and N_{CH_2}/N_{CH_3} for our laboratory and asteroid organics. We found that the organics on (24) Themis have a τ_{CH_2}/τ_{CH_3} ratio of 1.1 identical to propane residue and hexane residue, and a N_{CH_2}/N_{CH_3} ratio of 2.3. This value suggests the organics on (24) Themis may be represented by an unknown material with a N_{CH_2}/N_{CH_3} ratio between that of 3-MP residue and the propane/hexane residues. For (65) Cybele we found a τ_{CH_2}/τ_{CH_3} ratio of 0.4 and a N_{CH_2}/N_{CH_3} of 0.5. The τ_{CH_2}/τ_{CH_3} ratio for (65) Cybele is most similar to our un-irradiated 3-methylpentane

sample, while the N_{CH_2}/N_{CH_3} does not match any of our laboratory organics. The asteroid organics are likely not represented by a single aliphatic carrier but rather a complex combination of them. For both asteroids the lower τ_{CH_2}/τ_{CH_3} and N_{CH_2}/N_{CH_3} ratios suggest that the organics may be relatively short in chain length with few -CH₂- groups, and/or highly branched. The even lower values for Cybele imply that the organics may be different from Themis, more branched and shorter in chain length. These highly disordered organics may be the result of formation region of the solar nebula, or possibly induced by thermal evolution and/or billions of years of solar and cosmic irradiation.

Compared to other astronomical sources we did not find any similarities to the organics on (65) Cybele. This may be due to the lower S/N of these asteroid data, or that we do not yet have a representable sample of Cybele's organics. The Themis organics had spectral similarities to several interesting sources, and may be genetically related to the interstellar medium, IDPs, and some carbonaceous chondrites. More specifically, Themis had τ_{CH_2}/τ_{CH_3} and N_{CH_2}/N_{CH_3} ratios that closely matched the DISM, and had a N_{CH_2}/N_{CH_3} ratio similar to several primitive chondrites such as Renazzo (CR2), Nogoya (CM2), and Paris (CM). We suggest that Themis is an excellent candidate for the parent body of primitive CI/CM/CR meteorites, especially CM2 chondrites since the τ_{CH_2}/τ_{CH_3} and N_{CH_2}/N_{CH_3} ratios of Themis are most similar to the average of these ratios for CM2 chondrites.

We also compared the C-H stretch band centers of our asteroid organics with that of several astronomical sources. We find both (24) Themis and (65) Cybele have C-H stretch features most consistent with the DISM, IDPs, meteorite Cold Bokkeveld, and our laboratory samples. We also attribute weaker features at $3.35\ \mu\text{m}$ and $3.54\ \mu\text{m}$ in the spectra of these asteroid to possibly aliphatic hydrocarbons chemically bonded to electronegative groups such as aromatic hydrocarbons. A feature at $3.3\ \mu\text{m}$ has been confirmed in both asteroid spectra. We propose that the asteroid organics may be represented by aliphatics chemically bonded to aromatics, and those that are not.

Our laboratory simulations of asteroid organics are the first step in finding the relationship between asteroids and other sources of organics throughout the solar system. We look forward to sample return missions such as OSIRIS-Rex that will bring back physical samples from 1999 RQ36, an asteroid rich in organic material. This will be the first mission of its kind, and will help us to study in better detail the organics on an asteroid. Using ground-based spectroscopy on asteroids (24) Themis and (65) Cybele we are limited to simple analysis such as the τ_{CH_2}/τ_{CH_3} and N_{CH_2}/N_{CH_3} ratios. With a sample return we can perform more complex analysis, such as characterizing the elemental and isotopic composition of the organics on RQ36, which has been done for much of our meteorite collection. The OSIRIS-Rex sample return may help us to better connect carbonaceous chondrite meteorites with their likely parent body, and possibly shed new light on the origin of life on Earth.

6.1.1 Future Work

We would like to continue our study of primitive asteroids in the Themis family and Cybele group. Our ideal data set would consist of 2-4 μm spectroscopy of a large fraction of these populations with high enough S/N to resolve the CH-stretch region of organic material. This data set would test if our small sample presented in this work was representative of the other members of these populations. It would also allow us to perform a more comprehensive analysis of asteroid organics. For example we could test the relationship between ice and organics. Do both of these materials have to be present? We could also test if there is a relationship with asteroid size and the presence of organics, and if the bulk organics on Themis members differs from that in the bulk on Cybele group members.

In the 8-14 μm region, we would like to expand our study by observing more asteroids belonging to C, D, and S taxonomic types, and possibly asteroids belonging to other classes such as Bus X-types. Additionally we would like to test the robustness of other taxonomy systems such as Bus-DeMeo and Tholen using our current data set [34] [26].

In future work, we also propose to explore several aspects of our laboratory experiments. First the warm-up phase of our experiment was particularly interesting as it yielded unexpected results. During our warm-up from 15 K to 300 K the water-ice component of our mixture was supposed to sublime at approximately 150 K. Instead, the ice did not sublime until between 235 K and 240

K for our mixtures incorporating hexane and decane. We repeated the hexane experiment twice with identical results. We propose to further investigate these particular experiments, focusing on its relevance to the stability of water ice on asteroids that have surface temperatures near 230-240 K where ice should not exist but has been detected (e.g. (24) Themis and (65) Cybele). We predict that complex aliphatic organics, including longer-chain saturated aliphatic hydrocarbons (such as hexane), combined with aromatic hydrocarbons are partially responsible for the stability of ice at higher temperatures.

Secondly, we would like to understand how the chain length and/or branching nature of the laboratory organics changes as a result of UV irradiation, and warm up. We propose to track the N_{CH_2}/N_{CH_3} of the organic features from 15 K to 300 K to understand, on a first order level, how the -CH₂- and -CH₃- groups are changing (i.e. sublimating, bonding) throughout the experiments. Additionally we would like to quantize the abundance of tertiary carbon through our experiments from 15 K to 300 K.

LIST OF REFERENCES

- [1] H. Campins, K. Hargrove, N. Pinilla-Alonso, E. S. Howell, M. S. Kelley, J. Licandro, T. Mothé-Diniz, Y. Fernández, and J. Ziffer, “Water ice and organics on the surface of the asteroid 24 themis,” *Nature*, vol. 464, no. 7293, pp. 1320–1321, 2010.
- [2] A. S. Rivkin and J. P. Emery, “Detection of ice and organics on an asteroidal surface,” *Nature*, vol. 464, no. 7293, pp. 1322–1323, 2010.
- [3] Licandro, J., Campins, H., Kelley, M., Hargrove, K., Pinilla-Alonso, N., Cruikshank, D., Rivkin, A. S., and Emery, J., “(65) cybele: detection of small silicate grains, water-ice, and organics,” *A&A*, vol. 525, p. A34, 2011. [Online]. Available: <http://dx.doi.org/10.1051/0004-6361/201015339>
- [4] K. D. Hargrove, M. S. Kelley, H. Campins, J. Licandro, and J. Emery, “Asteroids (65) cybele,(107) camilla and (121) hermione: Infrared spectral diversity among the cybeles,” *Icarus*, 2012.
- [5] D. Takir and J. P. Emery, “Outer main belt asteroids: Identification and distribution of four 3- μ m spectral groups,” *Icarus*, 2012.
- [6] E. L. Volquardsen, A. S. Rivkin, and S. J. Bus, “Composition of hydrated near-earth object (100085) 1992 uy4,” *Icarus*, vol. 187, no. 2, pp. 464–468, 2007.
- [7] S. J. Bus and R. P. Binzel, “Phase ii of the small main-belt asteroid spectroscopic survey: A feature-based taxonomy,” *Icarus*, vol. 158, no. 1, pp. 146–177, 2002.
- [8] M. P. Bernstein, S. A. Sandford, and L. J. Allamandola, “Lite’s far-flung raw materials,” *Scientific American*, vol. 281, no. 1, pp. 42–49, 1999.
- [9] M. Lazzarin, S. Marchi, L. Moroz, R. Brunetto, S. Magrin, P. Paolicchi, and G. Strazzulla, “Space weathering in the main asteroid belt: The big picture,” *The Astrophysical Journal Letters*, vol. 647, no. 2, p. L179, 2006.
- [10] M. Barucci, M. Fulchignoni, and M. Lazzarin, “Water ice in primitive asteroids?” *Planetary and space science*, vol. 44, no. 9, pp. 1047–1049, 1996.
- [11] D. Jewitt and A. Guilbert-Lepoutre, “Limits to ice on asteroids (24) themis and (65) cybele,” *The Astronomical Journal*, vol. 143, no. 1, p. 21, 2012.

- [12] J. Sunshine, M. A’Hearn, O. Groussin, J.-Y. Li, M. Belton, W. Delamere, J. Kissel, K. Klaasen, L. McFadden, K. Meech *et al.*, “Exposed water ice deposits on the surface of comet 9p/tempel 1,” *Science*, vol. 311, no. 5766, pp. 1453–1455, 2006.
- [13] H. H. Hsieh and D. Jewitt, “A population of comets in the main asteroid belt,” *Science*, vol. 312, no. 5773, pp. 561–563, 2006.
- [14] N. Schorghofer, “The lifetime of ice on main belt asteroids,” *The Astrophysical Journal*, vol. 682, no. 1, p. 697, 2008.
- [15] D. Prialnik and E. D. Rosenberg, “Can ice survive in main-belt comets? long-term evolution models of comet 133p/elst-pizarro,” *Monthly Notices of the Royal Astronomical Society: Letters*, vol. 399, no. 1, pp. L79–L83, 2009.
- [16] A. Rivkin, E. Howell, F. Vilas, and L. Lebofsky, “Hydrated minerals on asteroids: The astronomical record,” *Asteroids III*, vol. 1, pp. 235–253, 2002.
- [17] K. D. Hargrove, J. Emery, H. Campins, and M. S. Kelley, “Asteroid (90) antiope: Another icy member of the themis family?” *Icarus*, 2015 in press.
- [18] V. Zappala, P. Bendjoya, A. Cellino, P. Farinella, and C. Froeschlé, “Asteroid families: Search of a 12,487-asteroid sample using two different clustering techniques,” *Icarus*, vol. 116, no. 2, pp. 291–314, 1995.
- [19] J. Rayner, D. Toomey, P. Onaka, A. Denault, W. Stahlberger, W. Vacca, M. Cushing, and S. Wang, “Spex: A medium-resolution 0.8–5.5 micron spectrograph and imager for the nasa infrared telescope facility,” *Publications of the Astronomical Society of the Pacific*, vol. 115, no. 805, pp. 362–382, 2003.
- [20] M. Werner, T. Roellig, F. Low, G. Rieke, M. Rieke, W. Hoffmann, E. Young, J. Houck, B. Brandl, G. Fazio *et al.*, “The spitzer space telescope mission,” *The Astrophysical Journal Supplement Series*, vol. 154, no. 1, p. 1, 2004.
- [21] E. C. Pickering, “The draper catalogue of stellar spectra photographed with the 8-inch bache telescope as a part of the henry draper memorial,” *Annals of Harvard College Observatory*, vol. 27, pp. 1–388, 1890.
- [22] A. J. Cannon and E. C. Pickering, *The Henry Draper Catalog*. The Observatory, 1918, vol. 92.
- [23] E. P. Hubble, “Extragalactic nebulae.” *The Astrophysical Journal*, vol. 64, pp. 321–369, 1926.
- [24] G. De Vaucouleurs, “Classification and morphology of external galaxies,” in *Astrophysik IV: Sternsysteme/Astrophysics IV: Stellar Systems*. Springer, 1959, pp. 275–310.

- [25] G. Piazzì, *Risultati delle osservazioni della nuova stella scoperta il dì 1. gennajo all'Osservatorio reale di Palermo*, 1801.
- [26] D. J. Tholen, "Asteroid taxonomy from cluster analysis of photometry." 1984.
- [27] S. J. Bus, F. Vilas, and M. A. Barucci, "Visible-wavelength spectroscopy of asteroids," *Asteroids III*, vol. 1, pp. 169–182, 2002.
- [28] B. Zellner, D. Tholen, and E. Tedesco, "The eight-color asteroid survey: Results for 589 minor planets," *Icarus*, vol. 61, no. 3, pp. 355–416, 1985.
- [29] R. P. Binzel and S. Xu, "Chips off of asteroid 4 vesta: Evidence for the parent body of basaltic achondrite meteorites," *Science*, vol. 260, no. 5105, pp. 186–191, 1993.
- [30] S. Xu, R. P. Binzel, T. H. Burbine, and S. J. Bus, "Small main-belt asteroid spectroscopic survey: Initial results," *Icarus*, vol. 115, no. 1, pp. 1–35, 1995.
- [31] S. J. Bus and R. P. Binzel, "Phase ii of the small main-belt asteroid spectroscopic survey: The observations," *Icarus*, vol. 158, no. 1, pp. 106–145, 2002.
- [32] T. H. Burbine and R. P. Binzel, "Small main-belt asteroid spectroscopic survey in the near-infrared," *Icarus*, vol. 159, no. 2, pp. 468–499, 2002.
- [33] S. J. Bus, "Compositional structure in the asteroid belt: Results of a spectroscopic survey," 1999.
- [34] F. E. DeMeo, R. P. Binzel, S. M. Slivan, and S. J. Bus, "An extension of the bus asteroid taxonomy into the near-infrared," *Icarus*, vol. 202, no. 1, pp. 160–180, 2009.
- [35] M. J. Gaffey, J. F. Bell, and D. P. Cruikshank, "Reflectance spectroscopy and asteroid surface mineralogy," in *Asteroids II*, vol. 1, 1989, pp. 98–127.
- [36] T. D. Jones, "An infrared reflectance study of water in outer belt asteroids: Clues to composition and origin." 1988.
- [37] W. M. Irvine and J. B. Pollack, "Infrared optical properties of water and ice spheres," *Icarus*, vol. 8, no. 1, pp. 324–360, 1968.
- [38] J. Emery, D. Cruikshank, and J. Van Cleve, "Thermal emission spectroscopy (5.2–38 μm) of three trojan asteroids with the spitzer space telescope: Detection of fine-grained silicates," *Icarus*, vol. 182, no. 2, pp. 496–512, 2006.
- [39] P. Vernazza, M. Delbo, P. King, M. Izawa, J. Olofsson, P. Lamy, F. Cipriani, R. Binzel, F. Marchis, B. Merín *et al.*, "High surface porosity as the origin of emissivity features in asteroid spectra," *Icarus*, 2012.

- [40] W. Duley and D. Williams, “The infrared spectrum of interstellar dust-surface functional groups on carbon,” *Monthly Notices of the Royal Astronomical Society*, vol. 196, pp. 269–274, 1981.
- [41] M. P. Bernstein, S. A. Sandford, L. J. Allamandola, J. S. Gillette, S. J. Clemett, and R. N. Zare, “Uv irradiation of polycyclic aromatic hydrocarbons in ices: Production of alcohols, quinones, and ethers,” *Science*, vol. 283, no. 5405, pp. 1135–1138, 1999.
- [42] R. P. Binzel, D. F. Lupishko, M. Di Martino, R. J. Whiteley, and G. J. Hahn, “Physical properties of near-earth objects,” *Asteroids III*, vol. 255, 2002.
- [43] F. DeMeo and B. Carry, “The taxonomic distribution of asteroids from multi-filter all-sky photometric surveys,” *Icarus*, vol. 226, no. 1, pp. 723–741, 2013.
- [44] T. D. Jones, L. A. Lebofsky, J. S. Lewis, and M. S. Marley, “The composition and origin of the c, p, and d asteroids: Water as a tracer of thermal evolution in the outer belt,” *Icarus*, vol. 88, no. 1, pp. 172–192, 1990.
- [45] J. De León, J. Licandro, M. Serra-Ricart, N. Pinilla-Alonso, and H. Campins, “Finding the compositional diversity of the solar system,” in *Highlights of Spanish Astrophysics VI, Proceedings of the IX Scientific Meeting of the Spanish Astronomical Society (SEA)*, Zapatero Osorio MR et al.(eds.), 2011, pp. 555–569.
- [46] M. J. Gaffey, T. H. Burbine, and R. P. Binzel, “Asteroid spectroscopy: Progress and perspectives,” *Meteoritics*, vol. 28, no. 2, pp. 161–187, 1993.
- [47] D. T. Britt, D. J. Tholen, J. F. Bell, and C. M. Pieters, “Comparison of asteroid and meteorite spectra: Classification by principal component analysis,” *Icarus*, vol. 99, no. 1, pp. 153–166, 1992.
- [48] J. Hardorp, “The sun among the stars. i-a search for solar spectral analogs,” *Astronomy and Astrophysics*, vol. 63, pp. 383–390, 1978.
- [49] G. C. de Strobel, “Stars resembling the sun,” *The Astronomy and Astrophysics Review*, vol. 7, no. 3, pp. 243–288, 1996.
- [50] A. U. Landolt, “Ubvri photometric standard stars in the magnitude range 11.5-16.0 around the celestial equator,” *The Astronomical Journal*, vol. 104, pp. 340–371, 1992.
- [51] M. C. Cushing, W. D. Vacca, and J. T. Rayner, “Spextool: A spectral extraction package for spex, a 0.8–5.5 micron cross-dispersed spectrograph,” *Publications of the Astronomical Society of the Pacific*, vol. 116, no. 818, pp. 362–376, 2004.
- [52] W. D. Vacca, M. C. Cushing, and J. T. Rayner, “Nonlinearity corrections and statistical uncertainties associated with near-infrared arrays,” *Nonlinearity*, vol. 116, no. 818, pp. 352–361, 2004.

- [53] S. D. Lord, “A new software tool for computing earth’s atmospheric transmission of near- and far-infrared radiation,” *NASA Technical Memorandum 103957*, vol. 1, 1992.
- [54] A. Rivkin, R. Binzel, and S. Bus, “Constraining near-earth object albedos using near-infrared spectroscopy,” *Icarus*, vol. 175, no. 1, pp. 175–180, 2005.
- [55] L. A. Lebofsky, M. V. Sykes, E. F. Tedesco, G. J. Veeder, D. L. Matson, R. H. Brown, J. C. Gradie, M. A. Feierberg, and R. J. Rudy, “A refined standard thermal model for asteroids based on observations of 1 ceres and 2 pallas,” *Icarus*, vol. 68, no. 2, pp. 239–251, 1986.
- [56] J. R. Spencer, L. A. Lebofsky, and M. V. Sykes, “Systematic biases in radiometric diameter determinations,” *Icarus*, vol. 78, no. 2, pp. 337–354, 1989.
- [57] E. Tedesco, “The iras minor planet survey. tech. rpt,” PL-TR-92-2049. Phillips Laboratory, Hanscom Air Force Base, Massachusetts (online version available at [pdssbn.astro.umd.edu/sbhtml/asteroids/physical param. html](http://pdssbn.astro.umd.edu/sbhtml/asteroids/physical_param.html)), Tech. Rep., 1992.
- [58] M. Delbó and A. W. Harris, “Physical properties of near-earth asteroids from thermal infrared observations and thermal modeling,” *Meteoritics & Planetary Science*, vol. 37, no. 12, pp. 1929–1936, 2002.
- [59] A. W. Harris, “A thermal model for near-earth asteroids,” *Icarus*, vol. 131, no. 2, pp. 291–301, 1998.
- [60] E. Bowell, B. Hapke, D. Domingue, K. Lumme, J. Peltoniemi, and A. W. Harris, “Application of photometric models to asteroids,” in *Asteroids II*, vol. 1, 1989, pp. 524–556.
- [61] M. Florczak, D. Lazzaro, T. Mothé-Diniz, C. Angeli, and A. Betzler, “A spectroscopic study of the themis family,” *Astronomy and Astrophysics Supplement Series*, vol. 134, pp. 463–471, 1999.
- [62] J. Licandro, H. Campins, G. Tozzi, J. De León, N. Pinilla-Alonso, H. Boehnhardt, and O. Hainaut, “Testing the comet nature of main belt comets. the spectra of 133p/elst-pizarro and 176p/linear,” *arXiv preprint arXiv:1104.0879*, 2011.
- [63] R. P. Binzel, A. S. Rivkin, S. J. Bus, J. M. Sunshine, and T. H. Burbine, “Muses-c target asteroid (25143) 1998 sf36: A reddened ordinary chondrite,” *Meteoritics & Planetary Science*, vol. 36, no. 8, pp. 1167–1172, 2001.
- [64] R. P. Binzel, A. S. Rivkin, C. A. Thomas, P. Vernazza, T. H. Burbine, F. E. DeMeo, S. J. Bus, A. T. Tokunaga, and M. Birlan, “Spectral properties and composition of potentially hazardous asteroid (99942) apophis,” *Icarus*, vol. 200, no. 2, pp. 480–485, 2009.
- [65] R. P. Binzel, A. Morbidelli, S. Merouane, F. E. DeMeo, M. Birlan, P. Vernazza, C. A. Thomas, A. S. Rivkin, S. J. Bus, and A. T. Tokunaga, “Earth encounters as the origin of fresh surfaces on near-earth asteroids,” *Nature*, vol. 463, no. 7279, pp. 331–334, 2010.

- [66] P. Vernazza, T. Mothé-Diniz, M. A. Barucci, M. Birlan, J. Carvano, G. Strazzulla, M. Fulchignoni, A. Migliorini *et al.*, “Analysis of near-ir spectra of 1 ceres and 4 vesta, targets of the dawn mission,” *Astronomy and Astrophysics*, vol. 436, no. 3, 2005.
- [67] P. Vernazza, R. Binzel, C. Thomas, F. DeMeo, S. Bus, A. Rivkin, and A. Tokunaga, “Compositional differences between meteorites and near-earth asteroids,” *Nature*, vol. 454, no. 7206, pp. 858–860, 2008.
- [68] P. Vernazza, R. Binzel, A. Rossi, M. Fulchignoni, and M. Birlan, “Solar wind as the origin of rapid reddening of asteroid surfaces,” *Nature*, vol. 458, no. 7241, pp. 993–995, 2009.
- [69] J. Ziffer, H. Campins, J. Licandro, M. E. Walker, Y. Fernandez, B. E. Clark, T. Mothe-Diniz, E. Howell, and R. Deshpande, “Near-infrared spectroscopy of primitive asteroid families,” *Icarus*, vol. 213, no. 2, pp. 538–546, 2011.
- [70] T. Hiroi, M. E. Zolensky, and C. M. Pieters, “The tagish lake meteorite: A possible sample from a d-type asteroid,” *Science*, vol. 293, no. 5538, pp. 2234–2236, 2001.
- [71] B. E. Clark, J. Ziffer, D. Nesvorny, H. Campins, A. S. Rivkin, T. Hiroi, M. A. Barucci, M. Fulchignoni, R. P. Binzel, S. Fornasier *et al.*, “Spectroscopy of b-type asteroids: Subgroups and meteorite analogs,” *Journal of Geophysical Research: Planets (1991–2012)*, vol. 115, no. E6, 2010.
- [72] F. Marchis, J. Enriquez, J. Emery, M. Mueller, M. Baek, J. Pollock, M. Assafin, R. Vieira Martins, J. Berthier, F. Vachier *et al.*, “Multiple asteroid systems: Dimensions and thermal properties from spitzer space telescope and ground-based observations,” *Icarus*, vol. 221, no. 2, pp. 1130–1161, 2012.
- [73] P. Lacerda and D. C. Jewitt, “Densities of solar system objects from their rotational light curves,” *The Astronomical Journal*, vol. 133, no. 4, p. 1393, 2007.
- [74] B. Carry, “Density of asteroids,” *Planetary and Space Science*, vol. 73, no. 1, pp. 98–118, 2012.
- [75] J. Licandro, K. Hargrove, M. Kelley, H. Campins, J. Ziffer, V. Alí-Lagoa, Y. Fernández, and A. Rivkin, “5–14 μ m spitzer spectra of themis family asteroids,” *Astronomy & Astrophysics*, vol. 537, 2012.
- [76] P. Descamps, F. Marchis, J. Durech, J. Emery, A. Harris, M. Kaasalainen, J. Berthier, J.-P. Teng-Chuen-Yu, A. Peyrot, L. Hutton *et al.*, “New insights on the binary asteroid 121 hermione,” *Icarus*, vol. 203, no. 1, pp. 88–101, 2009.
- [77] Y. Kebukawa and G. D. Cody, “A kinetic study of the formation of organic solids from formaldehyde: Implications for the origin of extraterrestrial organic solids in primitive solar system objects,” *Icarus*, vol. 248, pp. 412–423, 2015.

- [78] K. J. Walsh, A. Morbidelli, S. N. Raymond, D. OBRIEN, and A. Mandell, “Populating the asteroid belt from two parent source regions due to the migration of giant planets—the grand tack,” *Meteoritics & Planetary Science*, vol. 47, no. 12, pp. 1941–1947, 2012.
- [79] K. Tsiganis, R. Gomes, A. Morbidelli, and H. Levison, “Origin of the orbital architecture of the giant planets of the solar system,” *Nature*, vol. 435, no. 7041, pp. 459–461, 2005.
- [80] S. Sandford, L. Allamandola, A. Tielens, K. Sellgren, M. Tapia, and Y. Pendleton, “The interstellar ch stretching band near 3.4 microns—constraints on the composition of organic material in the diffuse interstellar medium,” *The Astrophysical Journal*, vol. 371, pp. 607–620, 1991.
- [81] Y. Kebukawa, C. M. Alexander, and G. D. Cody, “Compositional diversity in insoluble organic matter in type 1, 2 and 3 chondrites as detected by infrared spectroscopy,” *Geochimica et Cosmochimica Acta*, vol. 75, no. 12, pp. 3530–3541, 2011.
- [82] G. Matrajt, J. Borg, P. Raynal, Z. Djouadi, L. d’Hendecourt, G. Flynn, and D. Deboffle, “Ftir and raman analyses of the tagish lake meteorite: Relationship with the aliphatic hydrocarbons observed in the diffuse interstellar medium,” *Astronomy and Astrophysics*, vol. 416, no. 3, pp. 983–990, 2004.
- [83] G. Matrajt, S. Messenger, D. Brownlee, and D. Joswiak, “Diverse forms of primordial organic matter identified in interplanetary dust particles,” *Meteoritics & Planetary Science*, vol. 47, no. 4, pp. 525–549, 2012.
- [84] E. Dartois, G. M. Caro, D. Deboffle, L. d’Hendecourt, K. Chan, X. Liao, K. Zhang, C. Jones, G. Bihain, G. Israelian *et al.*, “Diffuse interstellar medium organic polymers—photoproduction of the 3.4, 6.85 and 7.25 μm features p. 133,” *Astronomy & Astrophysics*, vol. 423, no. 3, 2004.
- [85] Y. Pendleton, S. Sandford, L. Allamandola, A. Tielens, and K. Sellgren, “Near-infrared absorption spectroscopy of interstellar hydrocarbon grains,” *The Astrophysical Journal*, vol. 437, pp. 683–696, 1994.
- [86] G. Matrajt, G. Flynn, D. Brownlee, D. Joswiak, and S. Bajt, “The origin of the 3.4 μm feature in wild 2 cometary particles and in ultracarbonaceous interplanetary dust particles,” *The Astrophysical Journal*, vol. 765, no. 2, p. 145, 2013.
- [87] L. Allamandola, S. Sandford, A. Tielens, and T. Herbst, “Methanol in the sky with diamonds,” *Meteoritics*, vol. 26, p. 313, 1991.
- [88] L. d’Hendecourt, L. Allamandola, and J. Greenberg, “Time dependent chemistry in dense molecular clouds. i-grain surface reactions, gas/grain interactions and infrared spectroscopy,” *Astronomy and Astrophysics*, vol. 152, pp. 130–150, 1985.

- [89] G. Matrajt, G. M. Caro, E. Dartois, L. d’Hendecourt, D. Deboffle, and J. Borg, “Ftir analysis of the organics in idps: Comparison with the ir spectra of the diffuse interstellar medium,” *Astronomy & Astrophysics*, vol. 433, no. 3, pp. 979–995, 2005.
- [90] P. Ehrenfreund, F. Robert, L. d’Hendecourt, and F. Behar, “Comparison of interstellar and meteoritic organic matter at 3.4 microns,” *Astronomy and Astrophysics*, vol. 252, pp. 712–717, 1991.
- [91] G. Flynn, L. Keller, M. Feser, S. Wirick, and C. Jacobsen, “The origin of organic matter in the solar system: Evidence from the interplanetary dust particles,” *Geochimica et Cosmochimica Acta*, vol. 67, no. 24, pp. 4791–4806, 2003.
- [92] L. P. Keller, S. Bajt, G. A. Baratta, J. Borg, J. P. Bradley, D. E. Brownlee, H. Busemann, J. R. Brucato, M. Burchell, L. Colangeli *et al.*, “Infrared spectroscopy of comet 81p/wild 2 samples returned by stardust,” *Science*, vol. 314, no. 5806, pp. 1728–1731, 2006.
- [93] S. Bajt, S. Sandford, G. Flynn, G. Matrajt, C. Snead, A. Westphal, and J. Bradley, “Infrared spectroscopy of wild 2 particle hypervelocity tracks in stardust aerogel: Evidence for the presence of volatile organics in cometary dust,” *Meteoritics & Planetary Science*, vol. 44, no. 4, pp. 471–484, 2009.
- [94] G. Muñoz Caro, E. Dartois, and K. Nakamura-Messenger, “Characterization of the carbon component in cometary stardust samples by means of infrared and raman spectroscopy,” *Astronomy and astrophysics*, vol. 485, no. 3, pp. 743–751, 2008.
- [95] S. A. Sandford, J. Aléon, C. M. Alexander, T. Araki, S. Bajt, G. A. Baratta, J. Borg, J. P. Bradley, D. E. Brownlee, J. R. Brucato *et al.*, “Organics captured from comet 81p/wild 2 by the stardust spacecraft,” *Science*, vol. 314, no. 5806, pp. 1720–1724, 2006.
- [96] D. P. Cruikshank, C. M. Dalle Ore, R. N. Clark, and Y. J. Pendleton, “Aromatic and aliphatic organic materials on iapetus: Analysis of cassini vims data,” *Icarus*, vol. 233, pp. 306–315, 2014.
- [97] Y. J. Pendleton and L. J. Allamandola, “The organic refractory material in the diffuse interstellar medium: mid-infrared spectroscopic constraints,” *The Astrophysical Journal Supplement Series*, vol. 138, no. 1, p. 75, 2002.
- [98] S. A. Sandford, Y. J. Pendleton, and L. J. Allamandola, “The galactic distribution of aliphatic hydrocarbons in the diffuse interstellar medium,” *The Astrophysical Journal*, vol. 440, p. 697, 1995.
- [99] S. Merouane, Z. Djouadi, L. L. S. d’Hendecourt, B. Zanda, and J. Borg, “Hydrocarbon materials of likely interstellar origin from the paris meteorite,” *The Astrophysical Journal*, vol. 756, no. 2, p. 154, 2012.

- [100] Y. Pendleton, “Hydrocarbons in meteorites, the milky way, and other galaxies,” in *Astrophysics of Dust*, vol. 309, 2004, p. 573.
- [101] J. De Leon, N. Pinilla-Alonso, H. Campins, J. Licandro, and G. Marzo, “Near-infrared spectroscopic survey of b-type asteroids: Compositional analysis,” *Icarus*, vol. 218, no. 1, pp. 196–206, 2012.
- [102] F.-R. Orthous-Daunay, E. Quirico, P. Beck, O. Brissaud, E. Dartois, T. Pino, and B. Schmitt, “Mid-infrared study of the molecular structure variability of insoluble organic matter from primitive chondrites,” *Icarus*, vol. 223, no. 1, pp. 534–543, 2013.
- [103] J. C. Castillo-Rogez and B. Schmidt, “Geophysical evolution of the themis family parent body,” *Geophysical Research Letters*, vol. 37, no. 10, 2010.
- [104] Y. Kebukawa, S. Nakashima, M. Ishikawa, K. Aizawa, T. Inoue, K. NAKAMURA-MESSENGER, and M. E. Zolensky, “Spatial distribution of organic matter in the bells cm2 chondrite using near-field infrared microspectroscopy,” *Meteoritics & Planetary Science*, vol. 45, no. 3, pp. 394–405, 2010.
- [105] C. Alexander, G. Cody, Y. Kebukawa, R. Bowden, M. Fogel, A. Kilcoyne, L. Nittler, and C. Herd, “Elemental, isotopic, and structural changes in tagish lake insoluble organic matter produced by parent body processes,” *Meteoritics & Planetary Science*, vol. 49, no. 4, pp. 503–525, 2014.
- [106] M. Yesiltas, Y. Kebukawa, R. E. Peale, E. Mattson, C. J. Hirschmugl, and P. Jenniskens, “Infrared imaging spectroscopy with micron resolution of sutter’s mill meteorite grains,” *Meteoritics & Planetary Science*, vol. 49, no. 11, pp. 2027–2037, 2014.
- [107] M. Yesiltas, C. Hirschmugl, and R. Peale, “In situ investigation of meteoritic organic-mineral relationships by high spatial resolution infrared spectroscopy,” *Meteoritics and Planetary Science Supplement*, vol. 76, p. 5068, 2013.
- [108] C. M. Alexander, “A common origin for organics in meteorites and comets: Was it interstellar?” *Proceedings of the International Astronomical Union*, vol. 7, no. S280, pp. 288–301, 2011.
- [109] S. Pizzarello, G. Cooper, and G. Flynn, “The nature and distribution of the organic material in carbonaceous chondrites and interplanetary dust particles,” *Meteorites and the early solar system II*, vol. 1, pp. 625–651, 2006.
- [110] K. J. Walsh, A. Morbidelli, S. N. Raymond, D. P. O’Brien, and A. M. Mandell, “A low mass for mars from jupiter’s early gas-driven migration,” *Nature*, vol. 475, no. 7355, pp. 206–209, 2011.